LEXNET
Low EMF Exposure Future Networks

D3.2 Wideband dosimeter design study & performances characterization
Release 2

Contractual delivery date:	M16
Actual delivery date:	M24

Document Information

Version	V2.0	Dissemination level	PU

Editor	S. BORIES (CEA-LETI)
Other authors	S.M. ANWAR (SAT), M. LE HENAFF (SAT), Y. TOUTAIN (SAT), Y. FERNANDEZ (TTI), A. SANCHEZ (TTI), D. DASSONVILLE (CEA), S. BORIES (CEA), T. SARREBOURSE (ORANGE) M. KOPRIVICA (TKS), A. NEŠKOVIĆ (TKS), M. POPOVIĆ (TKS), J. MILINKOVIĆ (TKS), S. NIKŠIĆ (TKS), M. MACKOWIAK, L. CORREIA (INOV), C. ROBLIN (TPT), A. SIBILLE (TPT), R. HASHMAT (TPT)
Abstract	*The design studies of the LEXNET wearable wideband dosimeter components are reported with architecture choices and final simulation results. A validation campaign of these different parts is addressed with measured performances characterization. The impact of external parameters as the body shadowing, the polarization distribution, and the traffic load are also addressed in this deliverable second release.*
Key words	Dosimeter, wideband, wearable, correction factor, uncertainty.

Project Information

Grant Agreement n°	318273
Dates	1st November 2012 – 31th October 2015

Document approval

Name	Position in project	Organisation	Date	Visa
Joe Wiart	Coordinator	Orange	13/01/2015	OK

Document history

Version	Date	Modifications	Authors
V1.0	10/04/2014	revised version from review	S. Bories
V2.0	17/07/2014	Release 2, Appendices are separated from the main D3.2 document	S. Bories

Table of contents

List of Acronyms

Abbreviations	Meanings
ADC	Analogue to Digital Convertor
AF	Antenna Factor
AOA	Angle of Arrival
AP	Access Point
ASA	Azimuth Spread of Arrival
ATF	Antenna Transfer Function
BPF	Band Pass Filter
BS	Base Station
BST	Barium-Strontium-Titanate
CMOS	Complementary Metal Oxide Silicon
CDF	Cumulative Distribution Function
DCR	Direct Conversion Receiver
DC	Direct Continuous
DET	Detector
DL	Down Link
DCS	Digital Cellular System
DOA	Direction of Arrival
DTC	Digitally Tunable Capacitor
EC	European Community
EEPROM	Electrically Erasable Programmable ROM
EI	Exposure Index
EM	Electro-Magnetic
EMC	Electro-Magnetic Compatibility
EMF	Electro-Magnetic Field
ESA	Elevation Spread of Arrival
FET	Field Effect Transistor
FF	Far Field
FOM	Figure of Merit

FTBR	Front to Back Ratio
GSM	Global System for Mobile
IF	Intermediate Frequency
I/O	Inputs/Outputs
IL	Insertion Loss
LEXNET	Low EMF EXposure future Networks
LED	Light Emitting Diode
LTE	Long Term Evolution
LNA	Low Noise Amplifier
LO	Local Oscillator
LOS	Line of Sight
LPF	Low Pass Filter
LTCC	Low Temperature Co-fired Ceramics
MAA	Mono-Axial Antenna
MEMS	Micro ElectroMechanical Systems
MRG	Mean Realized Gain
MIM	Metal Insulator Metal
MPC	Multi Path Component
NF	Noise Figure
NLOS	Non Line of Sight
O2I	Outdoor to Indoor
OIP3	Output Third-Order Intercept Point
P1dB	Compression Point at 1 dB
PC	Personal Computer
PCB	Printed Board Circuit
PL	Path Loss
PLL	Phase Locked Loop
RAT	Radio Access Technology
RF	Radio Frequency
Rx	Received
RMS	Root Mean Square
SAR	Specific Absorption Rate
SAW	Surface Acoustic Wave

SRF	Self-Resonant Frequency
SOI	Silicon On Insulator
SOS	Silicon On Sapphire
SPI	Serial Peripheral Interconnect
USB	Universal Serial Bus
Tx	Transmitted
TTL	Transistor Transistor Logic
VGA	Variable Gain Amplifier
UMTS	Universal Mobile Telecommunication System
UL	Up Link
UART	Universal Asynchrobous
UMa	Urban Macrocell
VCO	Voltage Controlled Oscillator
WLAN	Wireless Local Area Network
XPR	Cross Polarization Ratio

List of figures

List of Tables

Executive Summary

The wearable dosimeter represents a key tool for the LEXNET project since this network-independent measurement device will be used by the other work packages. It is able to feedback measurements on the wireless network and to assess the Exposure Index from electrical field values directly measured at the position of the user who wears it. This information could be used by the service providers to manage the network configuration in order to reduce global exposure. Compared to the LEXNET simplified dosimeter, the wearable one allows to differentiate any telecom services within the 0.7-6 GHz and also to identify the service provider both in Up-Link and in Down-Link.

The design of the LEXNET wearable dosimeter has been initiated from a review of existing dosimeters and other available solutions. Regarding this state of the art, two major innovations on the RF front-end are implemented. The first one concerns the high selectivity of the selected frequency band which enables to isolate and measure a given network provider contribution to the overall experience EMF exposure. The second innovation brings the advantage of a large flexibility to assess existing and future telecom standards without changing the hardware thanks to a frequency reconfigurable RF architecture on the 0.7-6 GHz frequency band. Part of the design innovation consists to distribute the complexity and selectivity constraints on both the pre-filter and the Direct Conversion Receiver.

Another main achievement in LEXNET is the study of the parameters impacting the accuracy of the measured results and to propose solutions that decrease uncertainties. First, the shadowing due to the close proximity of obstacles as well as the human body results in an important bias that could be compensated for the down link exposure measurement. Moreover, the roles of long-term variability, averaging time window, and polarization distribution of the electrical field are analyzed. The objective is to embrace the trade-off between simplifying and fastening measurements on one side and improving the accuracy and reducing the uncertainties on the other side.

During the two first years of the LEXNET project, the wearable dosimeter has been specified, designed, and it will be prototyped at the end of the second year. During the third year, functional prototypes will be deployed during the validation demonstrations. This tight schedule is made possible by the collaboration and the coordination of the different involved partners, who have developed the dosimeter components by considering all together the sensitivity/selectivity trade-off (5 mV/m minimum level for 3 MHz bandwidth), the battery autonomy (more than a day), and the dimensions performances (smartphone form factor).

1 INTRODUCTION

The main objective of the Low EMF EXposure future Networks (LEXNET) project is twofold. First LEXNET has defined a global metric to assess human exposure to electromagnetic fields (EMF) radiated by radio frequency communications devices. This aims to quantify, compare, and predict the current and future trends (usage and technologies) in term of global EMF exposure. The second objective is to provide means of reducing exposure thanks to low EMF radio and networks technologies. The LEXNET metric assessment approach requires evaluating the exposure induced by different devices and standards with a representative spatial sampling. This can be done through modeling with assumptions, but also via real-life measurements. The wearable and fixed dosimeters developed in LEXNET fill up this last requirement. This D3.2 deliverable focuses on the wearable version which has high-performances thanks to a more complex design compared to the fixed one.

The user exposure is obtained from the assessment of the whole body SAR induced by EM sources. Although SAR evaluation is not practically easy, SAR is mainly related to the field strength and location of the source regarding the user body. This field level can be estimated in different ways: first, through the Network to which the user is connected, second, thanks to information collected by disseminated field sensors or personal dosimeters directly worn by user. Individual user device transmitted (Tx) and received (Rx) powers, Base Stations (BS) or Access Point (AP) Tx power and traffic load are assessed information from network providers, but usually not fully available from the user equipment. Moreover this solution ignores emissions from other networks and is hence partial. Note that dosimeters can be deployed by the operators themselves or by independent external stakeholders such as regulatory agencies or local authorities (provinces, regions, cities, etc.).

The dissymmetry between Up-Link (UL) and Down-Link (DL) radio transmissions is retrieved in UL and DL user exposure evaluation challenges. On the one hand for the DL, the isotropy of the dosimeter is strongly affected by the user body. Fortunately the DL fields from far sources are at the end of the day statistically uniformly distributed over the azimuth directions and statistical model can compensate the bias. The DL challenge is addressed in this deliverable. On the other hand for the UL, sources are close to the body but dosimeter cannot estimate their location as regards the body neither the exact transmit power. Thus it is not possible to estimate UL user exposure (in term of SAR) from the field measured at the body-worn dosimeter location. The UL problem is addressed in LEXNET with other approaches (simulation, trace mobile…) nevertheless the selected architecture will remain possible the use of multi probes for future studies.

This deliverable is organized as follow. The chapter 2 presents the state of the art of the existing wearable dosimeters or other solutions to estimate exposure and their limitations. The chapter 3 details the design and the performances of the isolated parts of the wearable dosimeter such as the antenna, the tunable band pass filter, the variable gain Low Noise Amplifier, and the Direct Conversion Receiver. A global evaluation is proposed by considering all together the sensitivity/selectivity trade-off, the battery autonomy, and the dimensions performances. The consolidated results on the dosimeter characterization are addressed in chapter 4. First part deals with the body shadowing effect in the Down-Link exposure of body-worn scenario. Body-worn dosimeter characterization results are presented in controlled or real environments. A statistical approach proposes to model and compensate the bias resulting from body shadowing. The second part evaluates the bias and uncertainty level when mono-axial probe is used instead of the isotropic one. At last the variability of band selective measurements with regards to network environment is considered in different cities during the full day.

At last the conclusion of this second release of deliverable D3.2 synthesizes the reached performances for the wearable dosimeter sub-components, proposes strategies for sensor correction, and suggests the way forward.

2 WEARABLE DOSIMETER: STATE OF THE ART

The dosimeter is a device used to measure EMF value with good precision. They provide a low-end solution with reliable measurement certainty as compared to high-end professional solutions such as wide band probes with spectrum analyzers.

In this section, two existing wearable and "frequency selective" dosimeters are presented. These are the only ones to the author's best knowledge available in the market with reliable EMF measurement capabilities. Other solutions called "broadband" (EME Guard from SATIMO [1] or Radman from Narda [2]) exist. But these are not relevant in the context of this study, because they give an indication of the total E-field over the whole frequency band without any frequency selectivity characteristics.

2.1 Satimo solution: EME SPY 140

EME Spy 140 [3] (Figure 1) is a light and portable RF safety dosimeter which performs continuous measurements of the human exposure level to electromagnetic fields (EMF) on 14 pre-defined frequency bands. This unique solution enables accurate selective measurements without incurring the costs of an integrated spectrum analyzer.

Technical characteristics

FREQUENCY RANGES	AXIAL ISOTROPY Min - Max	AXIAL ISOTROPY Standard deviation
FM (88 – 108 MHz)	± 2.6 dB	± 1.7 dB
TV3 (174 – 223 MHz)	± 2.2 dB	± 1.3 dB
TETRA (380 - 390 MHz)	± 2.5 dB	± 1.2 dB
TV4&5 (470 – 830 MHz)	± 0.8 dB	± 0.4 dB
GSM Tx (880 – 915 MHz)	± 2.6 dB	± 1.6 dB
GSM Rx (925 – 960 MHz)	± 2.4 dB	± 1.5 dB
DCS Tx (1710 – 1785 MHz)	± 2.3 dB	± 1.3 dB
DCS Rx (1805 – 1880 MHz)	± 2.2 dB	± 1.4 dB
DECT (1880 – 1900 MHz)	± 1.2 dB	± 0.8 dB
UMTS Tx (1920 – 1980 MHz)	± 0.9 dB	± 0.5 dB
UMTS Rx (2110 – 2170 MHz)	± 1.3 dB	± 0.6 dB
WiFi 2G (2400 – 2500 MHz)	± 1.5 dB	± 0.8 dB
WiMAX (3400 – 3800 MHz)	± 2.9 dB	± 1.5 dB
WiFI 5G (5150 – 5850 MHz)	± 3.9 dB	± 2.0 dB

Figure 1 : EME Spy 140

This dosimeter is able to discriminate upload and download link. This original specification is not only useful to assess the contribution of each transmitter, but also to avoid corruption of the results by phones emitting close to the dosimeter.

Measurements are done from a sensitivity of 5 mV/m up to 5 V/m (with a dynamic of 60 dB). The dimensions of this dosimeter are 168,5*79*49,7 mm (H*L*W) for a weight of 410 g. It is able to store around 80 000 measurements with 4 to 255 seconds between measurements.

There are two modes of operation:

1. The apparatus is operable in real time. In this case, the visualization can be done on a PC, tablet or smartphone. The data transfer can be done via an USB cable or directly via Bluetooth.
2. It is also possible to program a measurement cycle. The measurements are then stored in the device, and at the end of the cycle can be downloaded via an USB link to a PC.

2.2 MASCHEK solution: ESM140

The German Company MASCHEK has also developed a frequency selective dosimeter [4]. The main characteristics of this dosimeter are summarized below:

Measurement range:	0.010V/m - 70V/m (mean value, CW)	
Range selection:	automatic (auto-range)	
Frequency range:	GSM900	(mid-range frequency, 900MHz uplink 935MHz downlink)
	GSM1800	(mid-range frequency, 1750MHz uplink 1850MHz downlink)
	DECT	(mid-range frequency, 1895MHz up and downlink)
	UMTS	(mid-range frequency, 1950MHz uplink 2140MHz downlink)
	WLAN	(mid-range frequency 2440MHz up and downlink)
Accuracy:	±2dB in free field (mid-range frequency of respective band) (3.5V/m)	
	±4 dB with dosimeter worn on upper arm (3.5V/m)	
Measuring rate:	20kHz, internal	
Measuring method:	HF sensor, detector,	
Memory:	260 000 records for each of the 8 channels, both mean and peak value	
Recording rate:	0.5 to 10 secs	
Recording mode:	mean and peak value	
Functions:	marking function by means of push-button, acoustic signal when pressed	
Status display:	LED indicates measuring, battery state, standby, data transfer	
Operating time:	approx. 37 hours with one battery charge	
Standby:	6 months	
Charging time:	90 minutes (if battery completely discharged)	
PC interface:	USB	
Operating temperature:	-10 to 45ºC	
Storage temperature:	-20 to 50ºC	
Dimensions:	45mm X 115mm X 29mm	
Weight:	87 g with battery (not including strap)	

Figure 2 : Main characteristics of ESM 140 dosimeter

2.3 Comparison between EME-SPY and ESM 140

For 10 years, a lot of validations and comparisons of these dosimeters were performed. Among the most comprehensive studies, we can mention:

- Seawind project "Sound Exposure & Risk Assessment of Wireless Network Devices – Deliverable 1.1 - Literature review of exposure assessment and dosimetry of wireless networks" [5]
- Dominique PICARD, Luce FOUQUET, Sébastien CHAUVIN - "Characterization of four different Radio Frequency dosimeters [6]
- Georg Neubauer, Stefan Cecil, Wolfram Giczi, Benjamin Petric, Patrick Preiner, Jürg Fröhlich, Martin Röösli – Final Report on the project C2006-07: "Evaluation of the correlation between RF dosimeter reading and real human exposure" – 2008 [7]

Lots of these studies were realized with an old version of the SATIMO dosimeter (EME Spy 90/120/121), but they have the advantage to propose comparisons between both devices.

	Satimo EME Spy 121	Maschek ESM 140
Frequency bands		
FM	88–108 MHz	Not included
TV3	174–223 MHz	Not included
TETRA	380–400 MHz	Not included
TV 4&5	470–830 MHz	Not included
GSM900 Uplink	880–915 MHz	900 MHz[a]
GSM900 Downlink	925–960 MHz	935 MHz[a]
GSM1800 Uplink	1710–1785 MHz	1750 MHz[a]
GSM1800 Downlink	1805–1880 MHz	1850 MHz[a]
DECT	1880–1900 MHz	1895 MHz[a]
UMTS Uplink	1920–1980 MHz	1950 MHz[a]
UMTS Downlink	2110–2170 MHz	2140 MHz[a]
WLAN	2400–2500 MHz	2440 MHz[a]
Antennas	Isotropic three axis	Folded
Spectral analysis	Passive filters	Narrow band antennas
Measurement range	0.05–10 V/m	0.01–70 V/m
Logging interval	4-255 s	0.5–10 s
No of samples stored	12,540	260,000
Size	193 x 95.6 x 69.4 mm^3	100 x 45 x 20 mm^3
Weight	450 g	70 g

[a]Center frequency mentioned in the technical specifications

Figure 3 : Comparison between EMESPY 121 and ESM 140 [5][8]

The term “folded” for the antenna type used for the Maschek ESM 140 dosimeter signifies the folded dipole antennas.

The principal interest of Maschek ESM 140 is its small dimension and its low weight. That is why it was sometimes preferred to the first one in studies involving children. Anyway, the others technical specifications (selectivity and isotropy) are lower than the specifications of the EME Spy.

2.4 Limitations of existing dosimeters

The current dosimeters allow to carry out frequency selective exposure measurements. However, there are two major limitations:

i. Current dosimeters do not have the ability to distinguish between different service providers. This property would be useful in the case where one wishes to determine the exposure from a specific service provider in a given area. This capability will also be helpful in comparing / calibrating the exposure simulations, which provide the exposure maps for a single operator (single source).

ii. Actual dosimeters do not take into account the error induced due to the immediate dosimeter environment (i.e. presence of the human body, or other obstacles). This error is quite considerable especially when measuring the Up-Link (UL) exposure, due to the shadowing effect of the human body between the mobile device (emitting source) and the dosimeter position [5], [8], and [9]. However the compensation of the DL bias is addressed in chapter 4.

3 LEXNET WEARABLE DOSIMETER DESIGN

In this section, the global design of the wearable dosimeter designed under the LEXNET project, is detailed. First the proposed architecture is defined as a whole. The choice of each component of the architecture was finalized after detailed calculations and discussions. Then each of the sub-components of the dosimeter is presented with details regarding their design and experimental characterization. Finally, a preliminary mechanical design is presented for the integrated solution. The principal characteristics are presented in the Table 1 below.

Characteristics	Description
Measurement capabilities	• **Able to contribute to the determination of the** EMF exposure index (defined by LEXNET-WP2) • Measurement differentiation by application (GSM, DCS, UMTS, LTE, WiFi etc.) and also by service provider • Up-Link and Down-Link differentiation • Log of measurements
User profile	• Service providers / operators • Research organizations • Regulatory bodies
Frequency bands	0.7 GHz – 6 GHz
Interface	• Bluetooth (tablet / smartphone) • USB
Product compliance	• Fully compliant with ICNIRP recommendations / guidelines (Or other references, IARC, WHO,etc.) • EC marking compatibility (EMC, electrical safety) • Mechanical and climatical certification
Probe sensitivity	• 5 mV/m
Dynamic range	• 60 dB (5 mV/m to 5 V/m)
Dimensions	• Smartphone form factor
Weight	• < 400 g

Table 1 : Main features of the LEXNET dosimeter

The dosimeter has to cover the frequency bands as described in Table 2.

	Start	Center	Stop	BW
LTE 20 - Uplink	791	806	821	30
LTE 20 - Downlink	832	847	862	30
GSM 900 - Uplink	880	897.5	915	35
GSM 900 - Downlink	925	942.5	960	35
DCS1800 - Uplink	1710	1747.5	1785	75
DCS 1800 - Downlink	1805	1842.5	1880	75
DECT	1880	1890	1900	20
UMTS - Uplink	1920	1950	1980	60
UMTS Downlink	2110	2140	2170	60
Wifi	2400	2441.75	2483.5	83.5
LTE band VII - Uplink	2500	2535	2570	70
LTE band VII - Downlink	2620	2655	2690	70
Wimax 3.6GHz	3300	3600	3900	600
Wifi 5 GHz	5150	5487.5	5825	675

Table 2 – Frequency bands requirements

3.1 General architecture and design

At first, two architectures were chosen and studied in parallel. One of them was a low level, simplistic solution with all the complexity focused on one component. The other was a high level, more complex solution with increased flexibility. After initial evaluation, it was decided to merge the two solutions and focus on a single architecture which would be suitable in terms of performance, design flexibility, power consumption, and cost.

The block diagram of the finalized architecture is presented in Figure 4. The main block, marked as “wearable dosimeter”, is the actual dosimeter. The external RF block, marked as “optional external front end”, is designed for more precise measurements with an external probe.

The first part of the dosimeter is the probe. A three axis probe has been selected for best isotropy. Next there is the band pass filter (BPF) which is a tunable filter for initial frequency selectivity. After that we have the variable gain low noise amplifier (LNA) block to amplify the received signal. This signal is then down-converted to base-band frequencies using the Direct Conversion Receiver (DCR) block. The base-band signal is then detected using a RMS power detector (part of the DCR block) and then sampled by the Analog to Digital Converter (ADC) present in the microcontroller. The measurements are stored in an internal memory block and can be transferred to a PC or a mobile device using the USB or Bluetooth connectivity modules. The battery provides the power to the RF and digital blocks. The external RF block for increased precision and sensitivity can be connected directly to the internal DCR block via an RF switch connector.

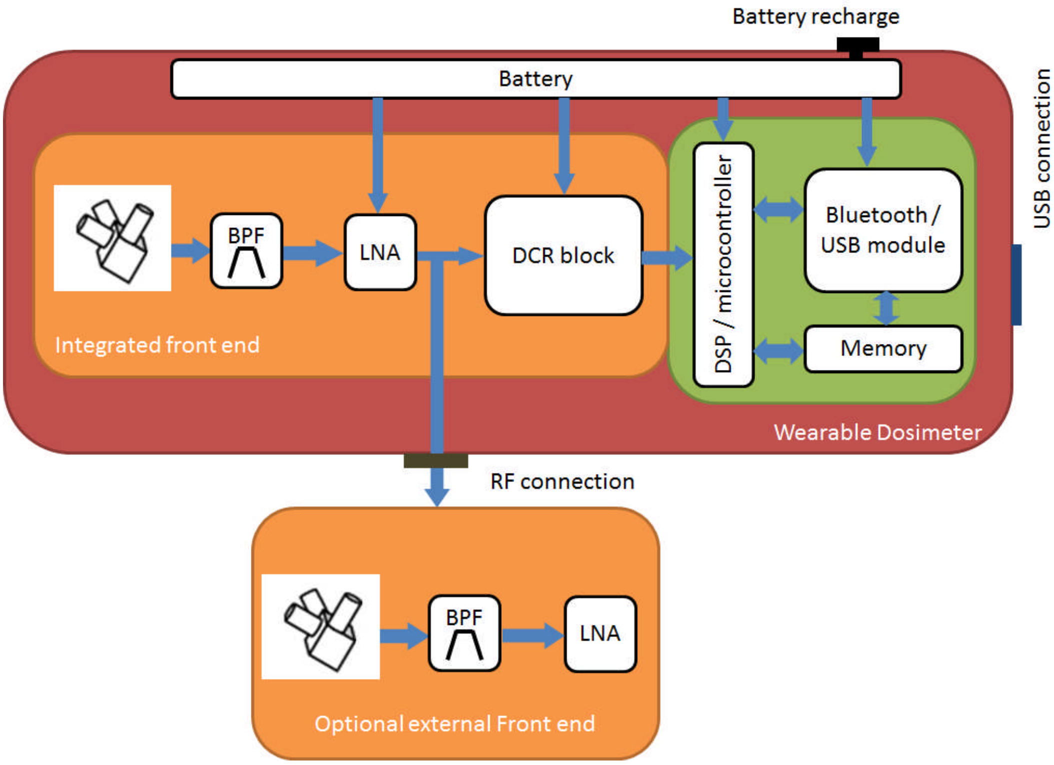

Figure 4 : Block diagram of the LEXNET wearable dosimeter

Each of the dosimeter sub-components (blocks) identified in Figure 4 is presented in detail in the following.

3.2 Tri-axial probe

The antenna probe selected for the LEXNET wearable dosimeter is presented in Figure 5. It consists of three monopole ball shaped antennas.

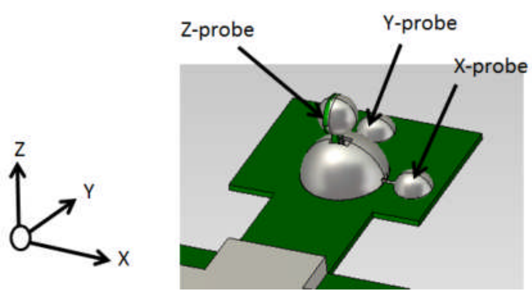

(a)

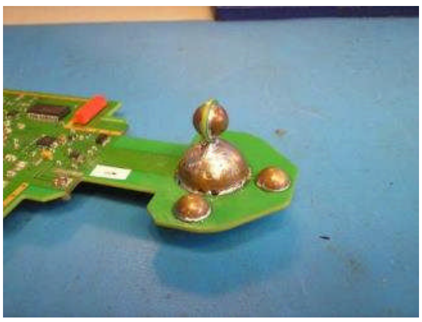

(b)

Figure 5 : Tri-axial probe selected for the LEXNET dosimeter (a) simulation model, (b) prototype used in actual EME-SPY dosimeters.

This probe is currently used in the EME-SPY dosimeters [3] for operation between 80 MHz up to 6 GHz. It represents excellent isotropy over the LEXNET frequency band as shown in Table 3 below.

FREQUENCY RANGES	AXIAL ISOTROPY	
	Min - Max	Standard Deviation
GSM Tx (880 – 915 MHz)	± 2.6 dB	± 1.6 dB
GSM Rx (925 – 960 MHz)	± 2.4 dB	± 1.5 dB
DCS Tx (1710 – 1785 MHz)	± 2.3 dB	± 1.3 dB
DCS Rx (1805 – 1880 MHz)	± 2.2 dB	± 1.4 dB
UMTS Tx (1920 – 1980 MHz)	± 0.9 dB	± 0.5 dB
UMTS Rx (2110 – 2170 MHz)	± 1.3 dB	± 0.6 dB
WiFi 2G (2400 – 2500 MHz)	± 1.5 dB	± 0.8 dB
WiMAX (3400 – 3800 MHz)	± 2.9 dB	± 1.5 dB
WiFI 5G (5150 – 5850 MHz)	± 3.9 dB	± 2.0 dB

Table 3 : Isotropy of the tri-axial probe over the LEXNET frequency band

The simulation and measured reflection coefficient for the probe are presented in Figure 6 for the three axes. The measurements and simulations were carried out at Satimo industries, Brest, France.

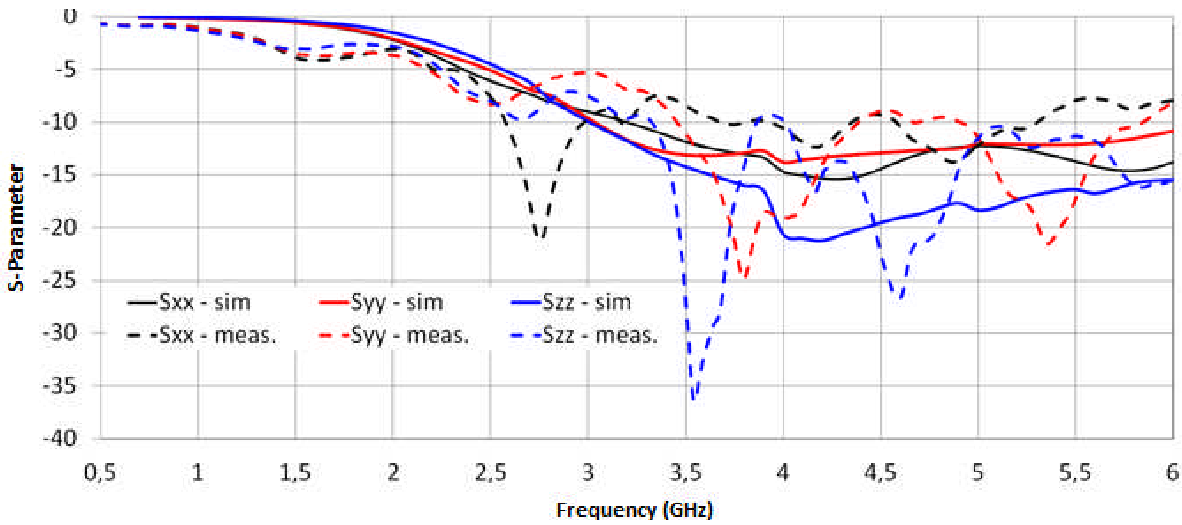

Figure 6 : Comparison between measured and simulation results for the probe reflection coefficient (in dB)

A good agreement in general is observed between the simulation and measurement results. The differences are principally due to the line losses and presence of connecting cables, which were not taken into account in the simulations.

The measured antenna factors for the dosimeter are presented in Table 4 for the different Telecommunication frequency standards present in the LEXNET frequency bandwidth. This measured data will be used in the calculations and determination of the whole system dynamic, sensitivity level, and the required gain ranges required for the low noise amplifier block. The external probe will be a similar one with better antenna factors (larger monopole size, and lower impact of immediate RF components, PCB, and battery) for increased sensitivity levels.

Standard	Centre freq. (MHz)	Antenna factor Probe X (dB)	Antenna factor Probe Y (dB)	Antenna factor Probe Z (dB)
LTE- XX DL	806	49	51	47
LTE -XX UL	847	49	49	46
GSM UL	895	48	49	46
GSM DL	947	47	48	46
DCS UL	1747	41	41	42
DCS DL	1842	41	42	42
UMTS UL	1950	41	43	41
UMTS DL	2140	39	43	41
Wifi	2450	41	43	41
LTE - VII UL	2535	42	42	40
LTE - VII DL	2650	43	43	43
WiMAX	3600	45	44	43
Wifi 5G	5500	48	47	47

Table 4 : Measured results for the probe antenna factor over the LEXNET frequency band

3.3 Tunable filter

The tunable filter is the RF Band Pass Filter (BPF) placed just after the antenna and followed by the LNA.This filter provides the first RF selectivity for the whole dosimeter architecture.The design goals for this BPF are:

- RF selectivity
- Low loss
- Distorsion-less response
- Flexibility (ability to be used for different frequency band configurations)
- Small physical size

3.3.1 RF Filter technology overview

Several technologies are available for RF BPF. From a dosimeter designer perspective, the most interesting technologies are:

- Discrete inductor (L) and capacitor (C): discrete components soldered to a PCB.

- Distributed parameters: some components are implemented with sections of transmission lines or coupled transmission lines on a PCB, in a planar structure.

- LTCC (low temperature co-fired ceramics): this is a technology that allows the very compact realization of RF filters in the form of monolithic components, by integrating capacitors, inductors, and transformers.

- SAW (surface acoustic wave): the electrical waves are transformed into mechanical (pressure) waves and back, through the use of transducers that are designed to pass only certain frequencies.

Each option has its pros and cons, summarized in Table 5.

To reach the specification for the tunable filter, a mix of these technologies is used.

RF Filter Technologies for PCB implementation			
Technology :	**Discrete L and C**	**Planar distributed**	**LTCC and SAW**
Selectivity	low	low	high
Insertion Loss	high	medium	low
Distortion	low	low	low
Flexibility	high	high	low
Size	medium	large, worse at lower frequencies	small

Table 5 - Different RF Filter Technologies

3.3.2 Tunable Filter Technology

To be able to monitor different frequency bands, the dosimeter has to switch between different frequency bands. RF switches are used to select one among n filter (Figure 7). This approach has been used in previous designs. It is a simple way to split the specified band into several sub-bands, selecting one different RF filter for each sub-band.

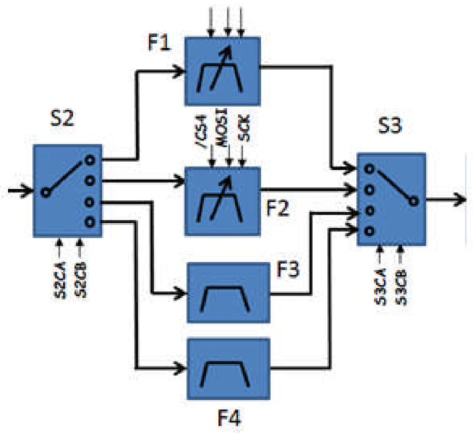

Figure 7 - RF filter selection with 4 way switches

Note that the RF switch brings insertion loss and non-linear distortion. Also this approach is limited by the space available for n way switches. It is desirable to have RF filters with inherent tunability, in order to cover future frequency bands. Such tunability can be obtained by several means:

- Varactor Diodes: these diodes exhibit a variable capacitance as a function of DC reverse bias.
- Integrated tunable capacitor: these are integrated RF switches and MIM (Metal Insulator Metal) capacitors. The capacitance is a function of the digital control word applied to the device.
- Ferroelectric device: these have a variable capacitance depending on the DC bias applied to a ferroelectric substrate, such as Barium-Strontium-Titanate (BST).
- Micro Electromechanical Systems (MEMS): in these devices, variable capacitances are realized with either mechanical switches, or with mechanically actuated membranes.

All these technologies have pros and cons, summarized in the following Table 6 - Different tunable RF Filter Technologies.

Tunable parts for RF Filter				
Technology :	**Varactor Diodes**	**Integrated Switched Capacitors**	**BST capacitors**	**MEMS capacitors**
Q factor	Moderate	low	moderate	high
Intercept Point	Low	low	moderate	high
Tuning Ratio	Moderate	moderate	low	high
Tuning Speed	Fast	fast	moderate	slow
Commercial Availability	high	moderate	low	low
Cost	low	moderate	moderate	moderate

Table 6 - Different tunable RF Filter Technologies

3.3.3 Peregrine Digitally Tunable Capacitor choice and validation.

After a search for commercially available parts, it was decided to use Integrated switched capacitors made by Peregrine (Digitally Tunable Capacitor). These cover a large range of capacitance values and are readily available from part distributors.

In the Peregrine DTC, a serial interface is used to control Field Effect Transistor (FET) switches that connect or disconnect High-Q MIM (Metal Insulator Metal) capacitors. The technology employed for these DTC is Silicon on Insulator (SOI) and is characterized by a Figure of Merit (FOM) equal to the product of On state resistance (Ron) times Off state capacitance (Coff). A block diagram of the DTC is shown in Figure 8, and a graph of Capacitance vs. Tuning State is shown in Figure 9.

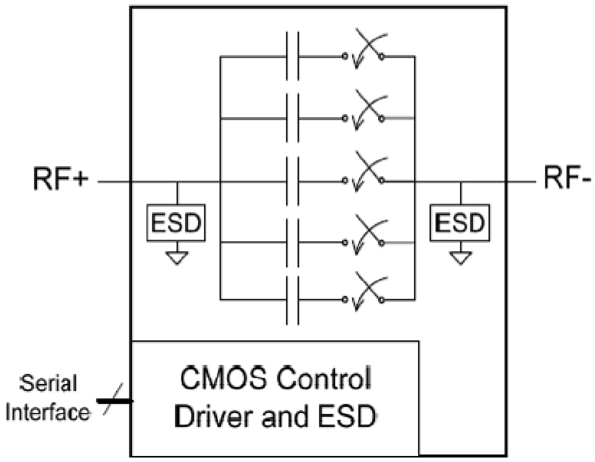

Figure 8 - Block diagram of Peregrine DTC – taken from Peregrine Application Note 29 (DTC Theory of Operation)

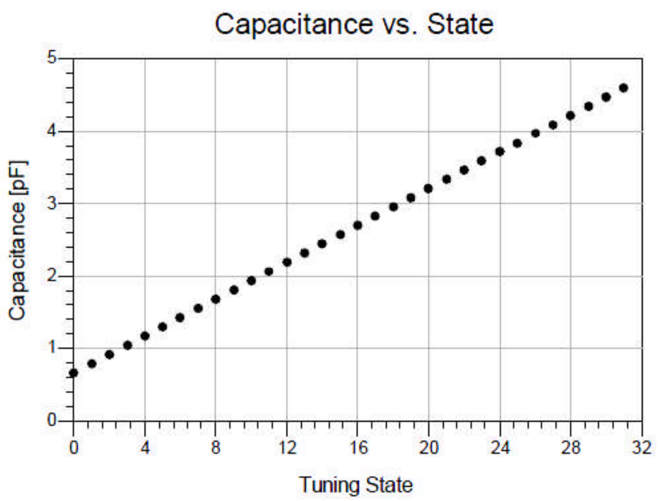

Figure 9 - Capacitance vs Tuning State of DTC – taken from Peregrine Application Note 29 (DTC Theory of Operation)

The Peregrine DTC comes in several part numbers, with different capacitance range and capacitance steps. A linear electrical model is supplied by Peregrine, that integrates the unwanted resistive, capacitive and inductive parasitics (Figure 10). Simulation of this model in Ansys Designer® and comparison with measurements have been performed in order to validate the accuracy of the model.

Figure 11 shows a comparison between measurement and simulation for an LC shunt resonator composed of an inductor and a DTC type PE64102, in two different tuning states.

A good fit can be seen between simulation and measurement.

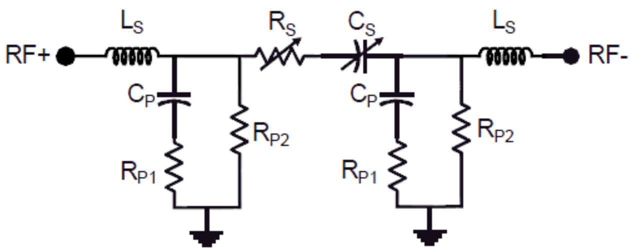

Figure 10 - DTC linear equivalent model - taken from Peregrine Application Note 29 (DTC Theory of Operation)

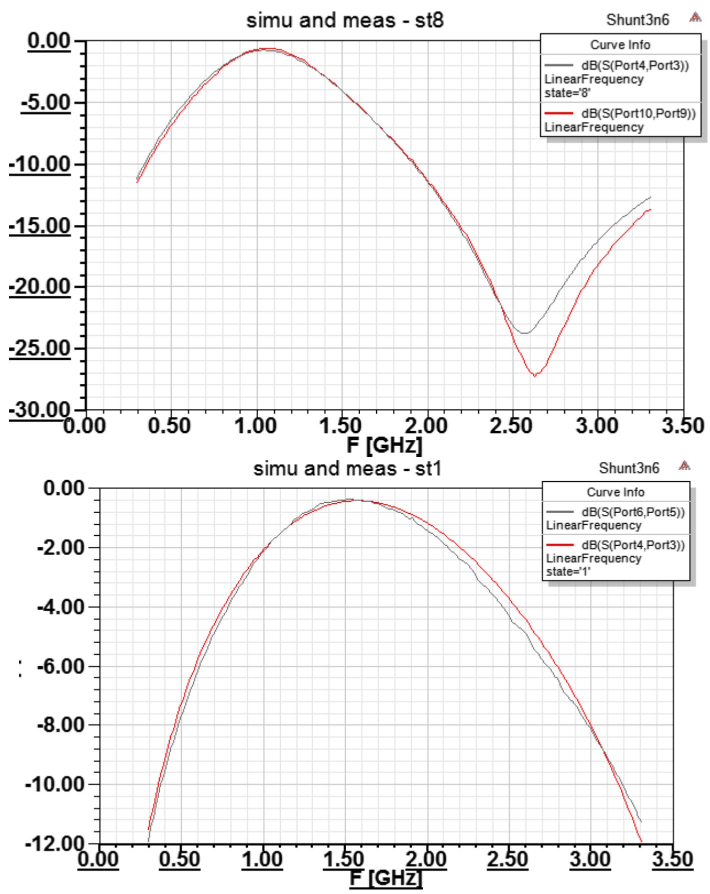

Figure 11 - Simulation (red) vs Measurement (black) of an LC resonator transmission (dB) for state 8 (top) and state 1 (bottom)

3.3.4 Tunable Filter requirements

Regarding the frequency bands to cover Table 2, the following scheme was decided, as a compromise between number of filters, tuning range and flexibility. The RF filter can be switched between 4 different RF filters F1 F2 F3 F4 :

- F1 : tuning filter for 791 to 960 MHz. (Fmax/Fmin = 1.21)
- F2 : tuning filter for 1710 to 2690 MHz. (Fmax/Fmin = 1.57)
- F3 : fixed filter for Wimax 3.5GHz.
- F4 : fixed filter for Wifi 5.5GHz.

Refer to Figure 7 for RF filter block diagram.

3.3.5 Tunable Filter simulation (791-960 MHz)

The 791-960 MHz BPF has been simulated. The topology (See Figure 12 - Tuning filter 790-960 MHz) is an L coupled shunt resonator with an order 2. Each resonator is composed of:

- a fixed inductor (discrete type),
- a fixed capacitor
- and a DTC in parallel.

The simulation result for filter F1 is in Figure 13, showing response for several tuning states.

By testing in simulation, it has been seen that most of the insertion loss is caused by the parasitics of the DTC. Also these parasitics cause a degradation of the rejection at higher frequencies (>3GHz). These can be mitigated by the adjunction of a notch filter (order 2, tuned at 1.9GHz), with still acceptable loss (between 1 and 4 dB IL). Also the filter bandwidth is not constant with tuning frequency: it is larger at higher frequencies, because only the resonators' frequencies are actuated, not the coupling coefficient (top coupling fixed inductor).

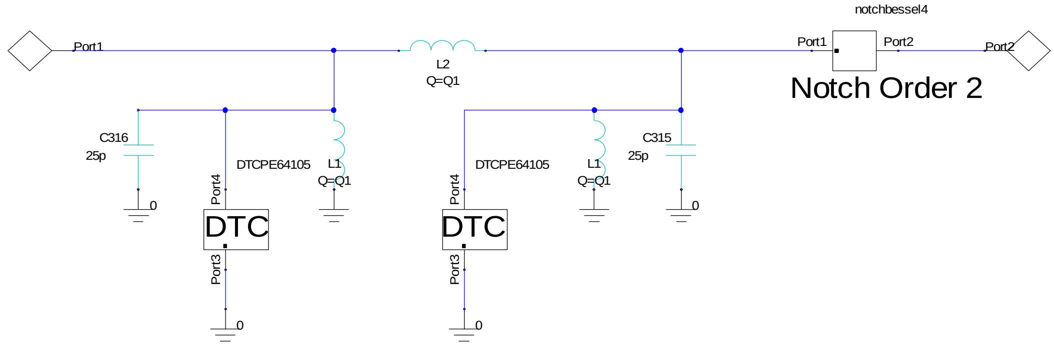

Figure 12 - Tuning filter 790-960 MHz

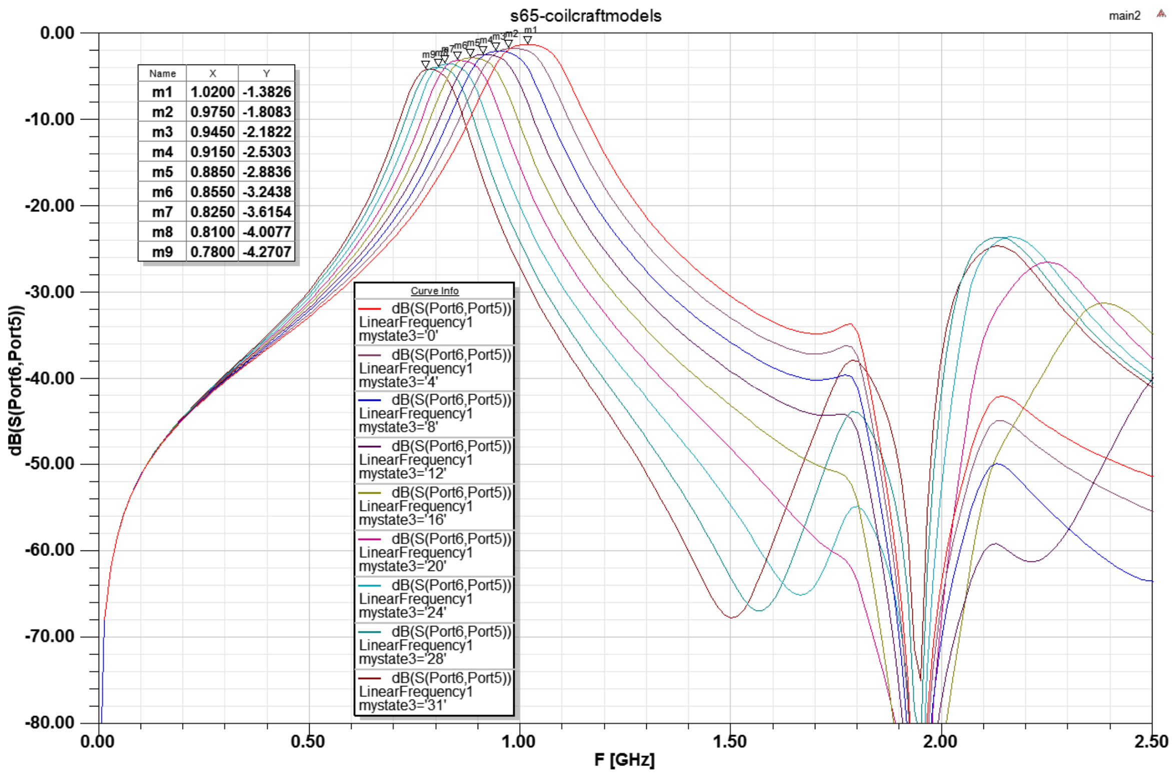

Name	X	Y
m1	1.0200	-1.3826
m2	0.9750	-1.8083
m3	0.9450	-2.1822
m4	0.9150	-2.5303
m5	0.8850	-2.8836
m6	0.8550	-3.2438
m7	0.8250	-3.6154
m8	0.8100	-4.0077
m9	0.7800	-4.2707

Figure 13 - Simulation Result for F1 Tuning filter (790-960 MHz) for different values of the DTC

3.3.6 Tunable Filter Characterization (1710-2690 MHz)

The 1710–2690 MHz filter F2 has been simulated. The topology is an L coupled shunt resonator, order 2, followed by a fixed low pass filter. Each resonator is composed of a fixed inductor (discrete type) and one DTC in parallel

Simulation results for this configuration can be seen in Figure 14. Each filter (F1 and F2) fits within a 16*16mm space.

A prototype filter F2 has been realized. The measurement can be seen in Figure 15.

The power consumption is limited to a maximum of 0.14 mA per DTC (typical). The total consumption for the filter bank is well within the DC power budget for the dosimeter.

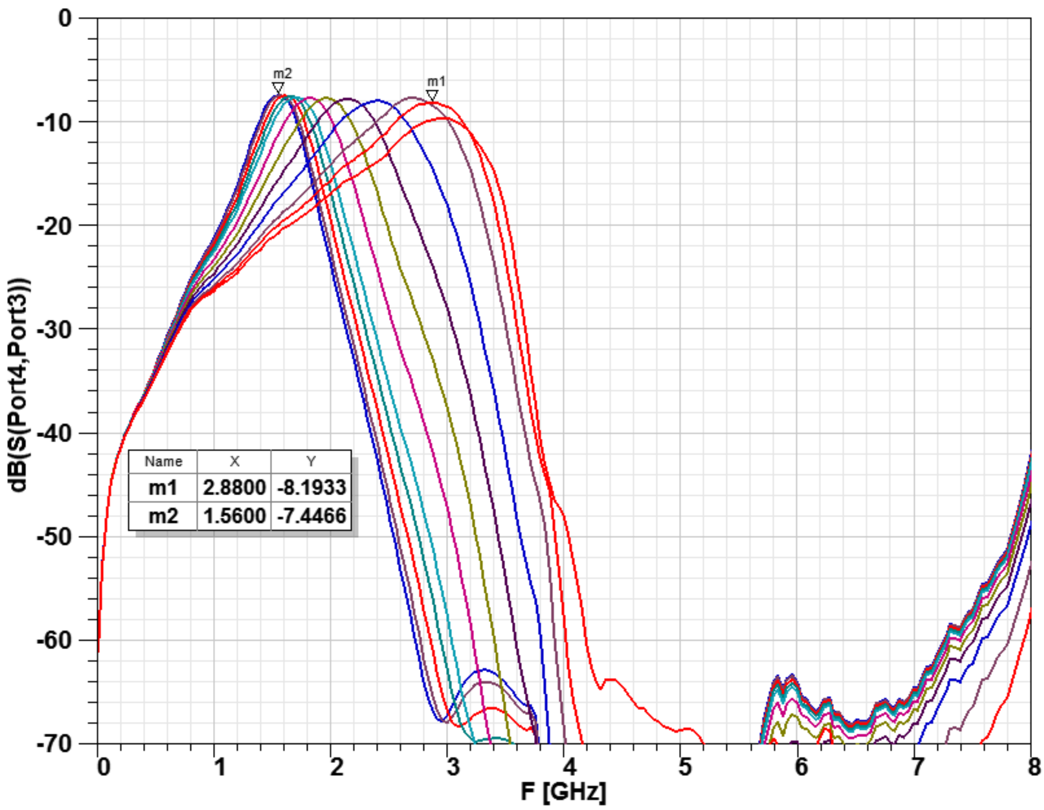

Figure 14 - Simulation Result for F2 Tuning filter (1710-2690MHz) for different values of the DTC

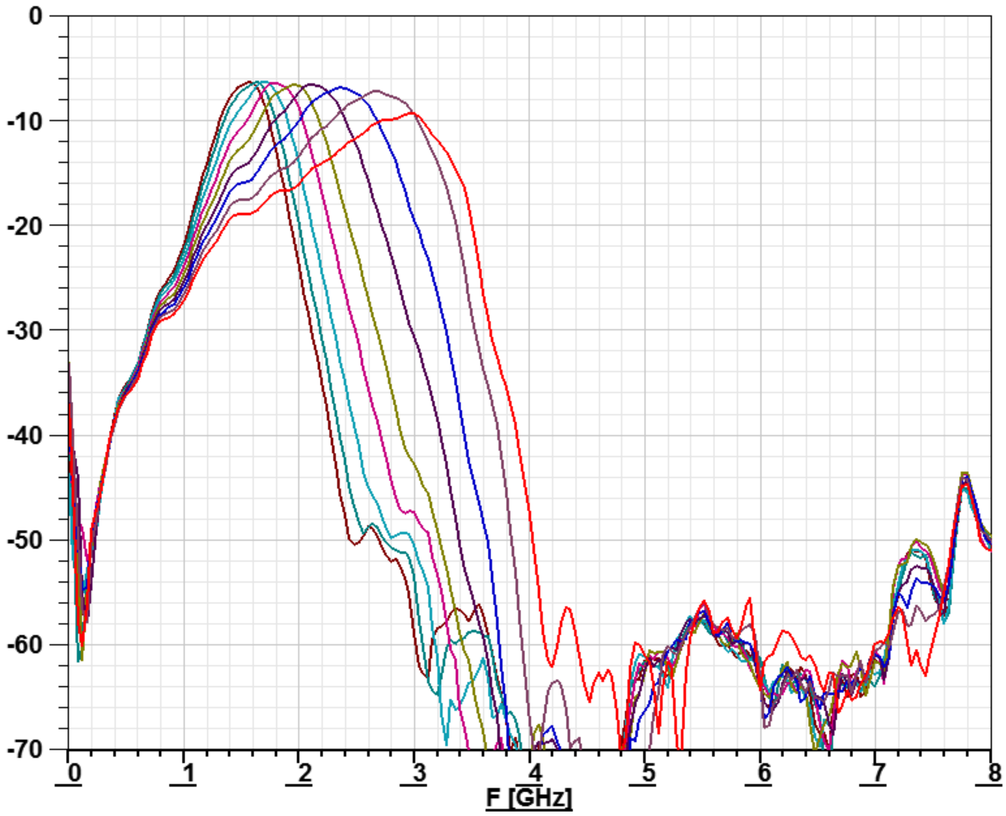

Figure 15 - Measurement for Prototype Filter F2 (S21 (dB) regarding frequency)

3.4 Variable gain LNA

The variable gain LNA is placed just after the tunable filters and followed by the down conversion receiver block. The aims of this stage are:

- to improve the dosimeter sensibility providing a good noise figure,
- to add gain to the RF chain and a dynamic gain control in order to accommodate the input signals to be properly detected,
- to offer enough P1dB and OIP3 to avoid intermodulation products when high interfering signals are wrapping the signal to be measured.

In this section, we will study the design of this variable gain LNA as well as carry out experimental characterization of the different parts.

3.4.1 Design study

The design of the variable gain LNA started with the definition of specifications based on the information from the previous and following blocks. After defining the requirements, we will discuss about the possible configurations to fulfil those specifications.

Some initial calculations were carried out analyzing the antenna factors and expected E-field values. Additionally, the expected losses in the reconfigurable filters were evaluated to estimate the maximum and minimum input power at variable gain LNA, Table 7.

Values obtained from the antenna factors and expected E-field: min. 5mV/m (74dBµV/m) // max. 5V/m (134dBµV/m)							
Freq. (MHz)	**Antenna Factor MAX (dB)**	**Antenna Factor MIN (dB)**	**Pant MAX (max. E-field) (dBm)**	**Pant MIN (min. E-field) (dBm)**	**Losses up to LNA (dB)**	**LNA max. Input Power (dBm)**	**LNA min. Input Power (dBm)**
800	47	50	-20	-83	8.8	-28.8	-91.8
900	47	50	-20	-83	8.8	-28.8	-91.8
1900	39	41	-12	-74	9.8	-21.8	-83.8
2400	38	39	-11	-72	9.8	-20.8	-81.8
3600	36	39	-9	-72	8.8	-17.8	-80.8
5500	39	41	-12	-75	8.8	-20.8	-82.8

Table 7 : Estimated maximum and minimum input power at LNA

Furthermore, other requirements come from the down conversion receiver block analysis; in this case in terms of P1dB and OIP3, Table 8. The LNA should ensure a free-of-intermodulation spectrum just before the down conversion mixer so we would be able to filter the selected baseband signal and detect its level accurately.

Values			
Frequency (MHz)	**Mixer ADL5801 Input P1dB (dBm)**	**Mixer ADL5801 OIP3 (dBm)**	**Estimated DRC block gain (dB)**
800	13.3	28.5	11.
900	13.3	28.5	11.8
1900	13.3	27	11.8
2400	14	24.5	11
3600	12.5	23.5	10.9
5500	11.5	23	10.8
HMC1020LP4E power detector input range: -65 to 7dBm (72dB dynamic range)			

Table 8 : Variable gain LNA requirements from DCR block

The gain control feature is required to equalize the level at the final power detector. We must be able to map the range of E-fields values, in this case from 5 mV/m to 5 V/m, into the dynamic range of the power detector. A calibration process will be performed to apply a gain adjustment according to the frequency of E-field to be measured.

Preliminary specifications for the variable gain LNA are summarized in Table 9:

Variable Gain LNA specifications					
Frequency (MHz)	**NF, typ (dB)**	**Gain, nominal (dB)**	**OIP3 (dBm)**	**P1dB (dBm)**	**Attenuation range (dB)**
800	5	24	28.5	13.3	20
900		24	28.5	13.3	
1900		18	27	13.3	
2400		16	24.5	14	
3600		14	23.5	12.5	
5500		17	23	11.5	
Operating voltage 5V (or 3.3V) // **Operating current** 75mA, typ (100mA, max)					

Table 9 : Variable gain LNA specifications

Two different RF configurations were proposed to fulfil all these requirements (Figure 16):

- **Option A:** LNA + variable gain amplifier solution
- **Option B:** LNA + digital attenuator + driver amplifier solution

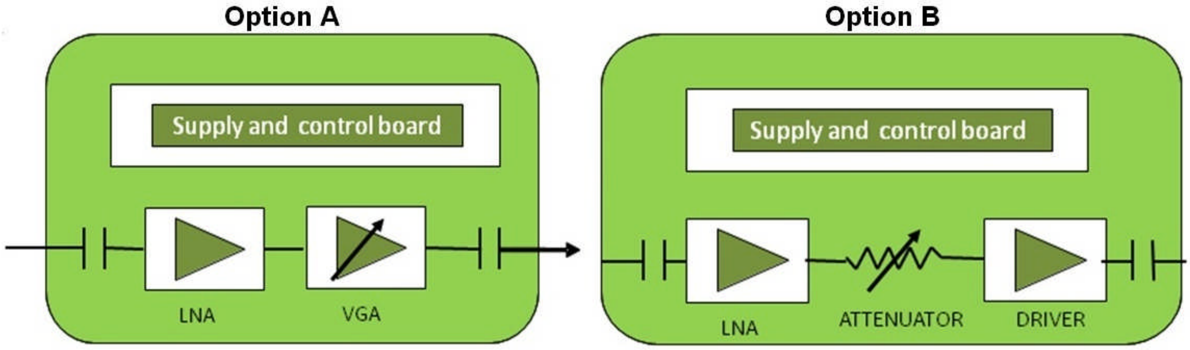

Figure 16 : Two possible configurations for the variable gain LNA: option A (left) and option B (right)

Based on these configurations, a component selection process was carried out:

- **Option A**:
  - ***VMMK-2303*** LNA from Avago Technologies [10] was selected. It offers 2 dB NF and 13-14 dB gain. P1dB and OIP3 are 9-10 dBm and 21-24 dBm respectively. It can works either with 3.3 V (24 mA) or 1.8 V (21mA).
  - ***HMC625LP5*** variable gain amplifier from Hittite [11] provides 20 dB maximum gain at 0.8 GHz and 9 dB at 5.5 GHz. P1dB values are 20 dBm and 13 dBm at these frequencies, and OIP3 goes from 35 to 26 dBm.
- **Option B**:
  - ***VMMK-2303*** LNA from Avago Technologies [10] was selected.

- ***HMC624LP4*** digital attenuator from Hittite [11] has insertion losses lower than 4 dB at 6 GHz. It offers an attenuation range of 31.5 dB that can be set with a 6-bits resolution allowing steps of 0.5 dB.
- 3 driver amplifiers were evaluated:
    - ***GVA-83+*** from Minicircuits [12]
    - ***PGA-1021+*** from Minicircuits [12]
    - ***NBB-400*** from RFMD [13]

GVA-83+ presents higher OIP3 level (29-31 dBm) with higher power consumption (72 mA @ 5 V), while ***PGA-1021+*** has lower OIP3 level (26.5-27 dBm) with lower power consumption (57 mA @ 3.3 V). Finally, ***NBB-400*** has an intermediate power consumption (50 mA @ 5 V) but lower P1dB (13-15 dBm) even having a good OIP3 performance (29 dBm).

3.4.2 Experimental characterization of the Variable Gain LNA parts

Once the main specifications were clearly defined, and possible RF configurations were presented, some measurements on evaluation boards from individual parts were carried out. As the final design should find a trade-off between power consumption and P1dB/OIP3 performance, option A was discarded and in option B, ***PGA-1021+*** was selected as the most promising part to fulfil RF requirements. Therefore only measured values from selected parts are presented.

Below test results from evaluation boards for selected parts for the variable gain LNA (***VMMK-2303 + HMC624LP4 + PGA-1021+)*** are presented.

VMMK-2303 characterization:

LNA is suitable for the first stage of the variable gain LNA. It can work with 3.3 V or 1.8 V supply, having low current consumption, and few external components (an advantage in terms of board size and mounting ease).

After modifying some component values on the evaluation board (Figure 17) to improve its performance over the full operating band, we made some gain, P1dB and OIP3 measurements.

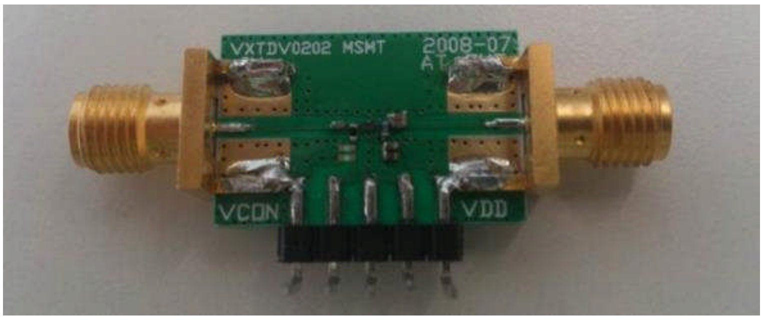

Figure 17 : Photograph of the VMMK-2303 evaluation board

VMMK-2303 experimental characterization Vd = 3.3V ; Vc = 1.8V ; Id = 24mA							
Freq. (MHz)	S11 (dB)	S21 (dB)	S22 (dB)	S22 (dB)	P1dB (dBm)	G1dB (dB)	OIP3 (dBm)
650	-5.1	12.7	-20.9	-8.4	8.9	11.7	24.0
890	-7.1	13.6	-19.9	-10.1	10.1	12.6	24.0
950	-7.5	13.7	-20.0	-10.4	10.2	12.6	24.1
1750	-11.0	13.7	-19.8	-14.8	10.6	12.7	24.7
1840	-11.2	13.7	-19.8	-15.1	10.5	12.7	24.8
1890	-11.3	13.7	-19.9	-15.2	10.6	12.6	24.9
1950	-11.4	13.6	-20.0	-15.3	10.5	12.6	25.0
2140	-11.7	13.6	-20.1	-15.6	10.6	12.5	25.2
2450	-12.4	13.4	-20.2	-15.3	10.5	12.4	25.2
3600	-13.6	12.9	-21.3	-12.6	10.1	11.9	24.8
5500	-13.1	12.3	-25.7	-8.1	10.5	11.3	24.2

Table 10 : VMMK-2303 measured features with 3.3 V supply

VMMK-2303 experimental characterization Vd = 1.8V ; Vc = 1.8V ; Id = 21mA							
Freq. (MHz)	S11 (dB)	S21 (dB)	S22 (dB)	S22 (dB)	P1dB (dBm)	G1dB (dB)	OIP3 (dBm)
650	-5.2	12.8	-21.0	-8.8	8.2	11.8	23.0
890	-7.3	13.7	-20.1	-10.7	9.2	12.7	23.0
950	-7.6	13.7	-20.0	-11.2	9.3	12.7	23.1
1750	-11.2	13.7	-19.9	-17.1	9.7	12.8	23.7
1840	-11.4	13.7	-19.9	-17.5	9.7	12.7	23.8
1890	-11.6	13.7	-19.8	-17.7	9.7	12.7	23.9
1950	-11.7	13.7	-20.0	-18.0	9.7	12.7	23.9
2140	-12.0	13.6	-19.9	-18.5	9.7	12.6	24.1
2450	-12.7	13.5	-20.0	-18.4	9.7	12.5	24.2
3600	-13.9	13.0	-21.0	-15.0	9.5	12.0	24.1
5500	-14.2	12.6	-24.4	-10.0	10.0	11.6	24.0

Table 11 : VMMK-2303 measured features with 1.8V supply

As we can see in Table 10 and Table 11, the LNA achieves good performance with both polarization points. Therefore, 1.8 V is the suitable bias point with an operating current of 21 mA. Furthermore, it provides around 2 dB wideband NF that allows a total NF lower than the specified 5 dB.

HMC624LP4 characterization:

The digital attenuator can work with 3.3 V or 5 V supply, and shows high OIP3. Its operating current is almost negligible, 2 mA. It offers a dual mode control interface which is CMOS/TTL compatible, and accepts either a three wire serial input or a 6 bits parallel word.

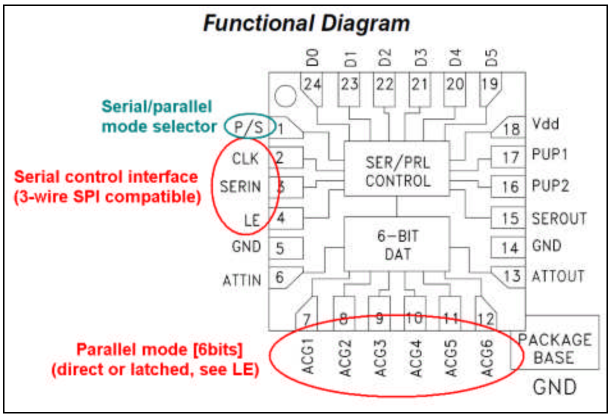

Figure 18 : HMC624LP4 functional diagram showing its control interfaces

PGA-1021+ characterization:

Measurements from the evaluation board of the ***PGA-1021+*** (Figure 19) are shown in Table 12.

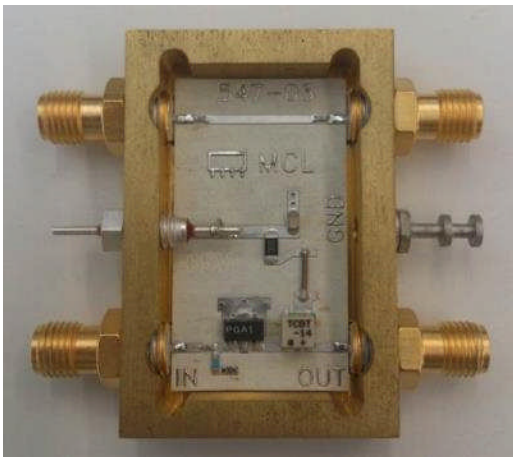

Figure 19 : Photograph of the PGA-1021+ evaluation board

PGA-1021+ experimental characterization Vcc = 3.3V ; Icc = 57mA							
Freq. (MHz)	**S11 (dB)**	**S21 (dB)**	**S22 (dB)**	**S22 (dB)**	**P1dB (dBm)**	**G1dB (dB)**	**OIP3 (dBm)**
650	-18.0	15.1	-21.2	-25.7	17.6	14.2	26.3
890	-16.6	14.7	-21.3	-24.4	17.7	13.8	26.3
950	-16.2	14.7	-21.2	-24.1	17.7	13.8	26.4
1750	-12.3	13.3	-21.6	-18.3	17.8	12.5	26.7
1840	-11.9	13.1	-21.6	-16.9	17.8	12.2	26.9
1890	-11.5	12.6	-22.0	-14.7	17.4	11.7	27.0
1950	-11.5	13.0	-21.7	-17.5	17.6	12.2	26.9
2140	-11.1	12.8	-21.9	-17.6	18.0	11.9	26.5
2450	-10.5	12.3	-21.9	-16.5	18.1	11.5	26.5
3600	-9.5	11.1	-22.4	-14.9	18.1	10.2	26.8
5500	-11.4	10.4	-22.0	-13.2	17.4	9.4	27.3

Table 12 : PGA-1021+ measured features

Based on measured results from evaluation boards, a block diagram analysis at 4 different frequencies was performed.

Table 13 evaluates the expected variable gain LNA specifications (with no attenuation applied) once the 3 stages are merged in a single block.

LNA + ATTV + PGA-1021+ @ 900MHz

Component P/N	VMMK-2303	HMC624LP4	PGA-1021+
Component type	LNA	Variable ATT	Driver
NF (dB)	2.0	1.6	2.3
Gain (dB)	13.7	-1.6	14.8
OIP3 (dBm)	23.0	50.0	26.3
P1dB (dBm)	9.3	30.0	17.7
Aggreg. values	VMMK-2303	HMC624LP4	PGA-1021+
NF (dB)	2.0	2.1	**2.2**
Gain (dB)	13.7	12.1	**26.9**
OIP3 (dBm)	23.0	21.4	**25.9**
P1dB (dBm)	9.3	7.6	**16.4**

LNA + ATTV + PGA-1021+ @ 1900MHz

Component P/N	VMMK-2303	HMC624LP4	PGA-1021+
Component type	LNA	Variable ATT	Driver
NF (dB)	2.0	1.9	2.4
Gain (dB)	13.8	-1.9	12.6
OIP3 (dBm)	23.9	50.0	27.0
P1dB (dBm)	9.8	30.0	17.4
Aggreg. values	VMMK-2303	HMC624LP4	PGA-1021+
NF (dB)	2.0	2.1	**2.2**
Gain (dB)	13.8	11.9	**24.5**
OIP3 (dBm)	23.9	22.0	**26.3**
P1dB (dBm)	9.8	7.8	**15.7**

LNA + ATTV + PGA-1021+ @ 2300MHz

Component P/N	VMMK-2303	HMC624LP4	PGA-1021+
Component type	LNA	Variable ATT	Driver
NF (dB)	2.0	2.0	2.6
Gain (dB)	13.5	-2.0	12.6
OIP3 (dBm)	24.2	50.0	26.5
P1dB (dBm)	9.7	30.0	18.1
Aggreg. values	VMMK-2303	HMC624LP4	PGA-1021+
NF (dB)	2.0	2.1	**2.2**
Gain (dB)	13.5	11.5	**24.1**
OIP3 (dBm)	24.2	22.2	**25.9**
P1dB (dBm)	9.7	7.7	**16.0**

LNA + ATTV + PGA-1021+ @ 5500MHz

Component P/N	VMMK-2303	HMC624LP4	PGA-1021+
Component type	LNA	Variable ATT	Driver
NF (dB)	2.0	4.5	3.6
Gain (dB)	12.6	-4.5	10.4
OIP3 (dBm)	24.0	50.0	27.3
P1dB (dBm)	10.0	30.0	17.5
Aggreg. values	VMMK-2303	HMC624LP4	PGA-1021+
NF (dB)	2.0	2.3	**2.7**
Gain (dB)	12.6	8.1	**18.5**
OIP3 (dBm)	24.0	19.5	**25.4**
P1dB (dBm)	10.0	5.5	**13.6**

Table 13 : Evaluation of the variable gain LNA expected performance

The expected NF is pretty lower than the specified one, keeping suitable gain level which can be adjusted thanks to 31.5 dB attenuation range from the digital attenuator. Finally, the selected driver amplifier fits P1dB and OIP3 requirements.

The total power consumption is around 80 mA with 3.3 V supply voltage.

Next step will be to evaluate a single PCB prototype with 3 stages (***VMMK-2303 + HMC624LP4 + PGA-1021+)*** to be finally integrated in the wearable dosimeter.

3.4.3 Experimental characterization of the Variable Gain LNA prototype

A prototype integrating the 3 stages (***VMMK-2303 + HMC624LP4 + PGA-1021+***) was developed and manufactured (see Figure 20) to evaluate its performance.

A 3-pin connector was placed to supply the 3.3V needed and its ground, and an optional shutdown line. A low dropout regulator was included to be able to generate two independent 1.8 V supplies for the VMMK-2303 (enabled or not with the shutdown line mentioned).

Before characterizing the RF features of the Variable Gain LNA prototype, its power consumption was measured to validate the initial specification. A total current consumption of 80mA from the 3.3 V input line was observed, matching the initial estimations based on the individual stages evaluation.

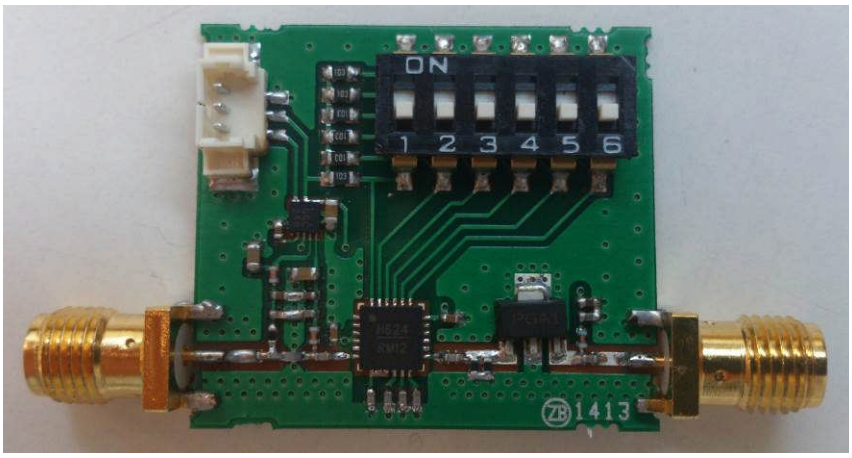

Figure 20 : Board of the Variable Gain LNA prototype

After the power supply test, measurements of the S-parameters, NF, 1dB compression point and OIP3 measurements were carried out to validate the prototype before being integrated in the wearable dosimeter.

Figure 21 shows the prototype gain as function of the attenuation applied. Note that a manual switch was included in this board in order to facilitate the attenuation control.

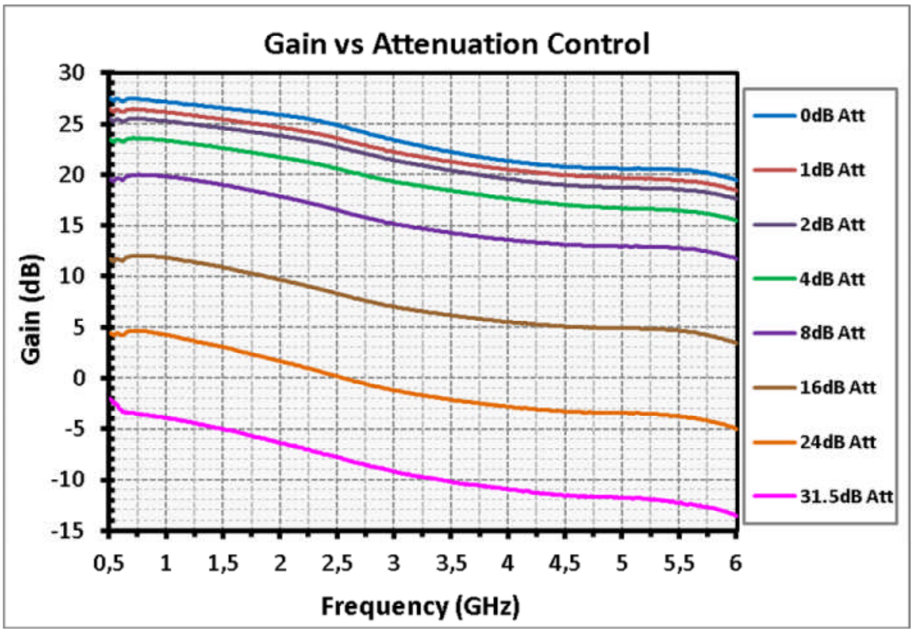

Figure 21 : Variable Gain LNA response as a function of the attenuation

A nominal 31.5 dB attenuation range is defined by the HMC624LP4 digital attenuator, but values among 30.8 and 32.7 dB were observed depending of the frequency of operation.

Figure 22shows the return losses characterization of the Variable Gain LNA prototype. Input matching is measured in terms of S11 parameter while S22 parameter determines the output matching.

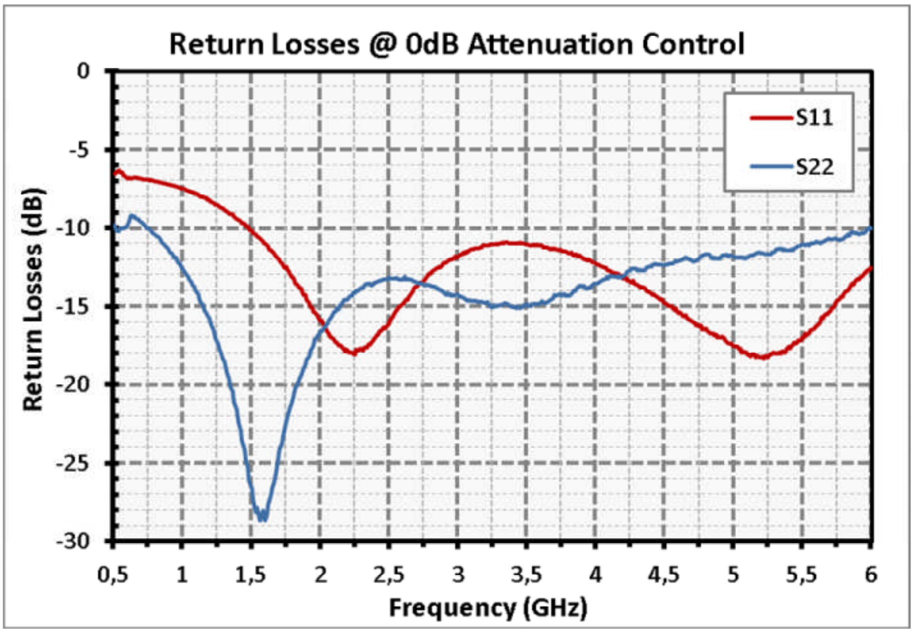

Figure 22 : Variable Gain LNA input and output return losses

An evaluation of the NF response was performed, and measurements at 0 dB attenuation can be observed in Figure 23.

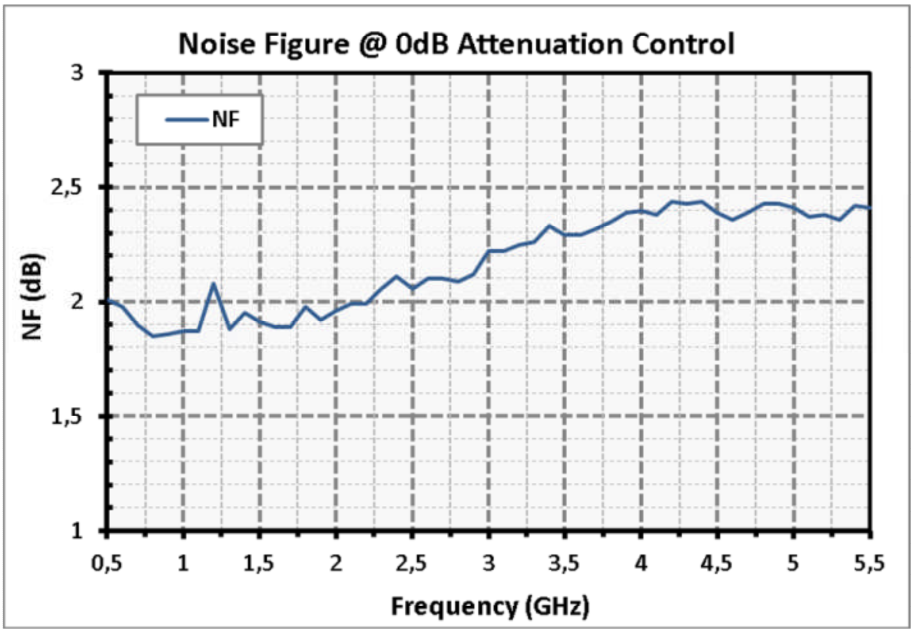

Figure 23 : Variable Gain LNA NF

Apart from the S-Parameter and NF characterization, measurements of the 1dB-compression point (output P1dB) and intermodulation, in terms of OIP3, were taken. These are really important specifications to be fulfilled in order to fit the requirements fixed by the DCR block.

P1dB feature and the associated gain at that point (G1dB) can be observed in Figure 24

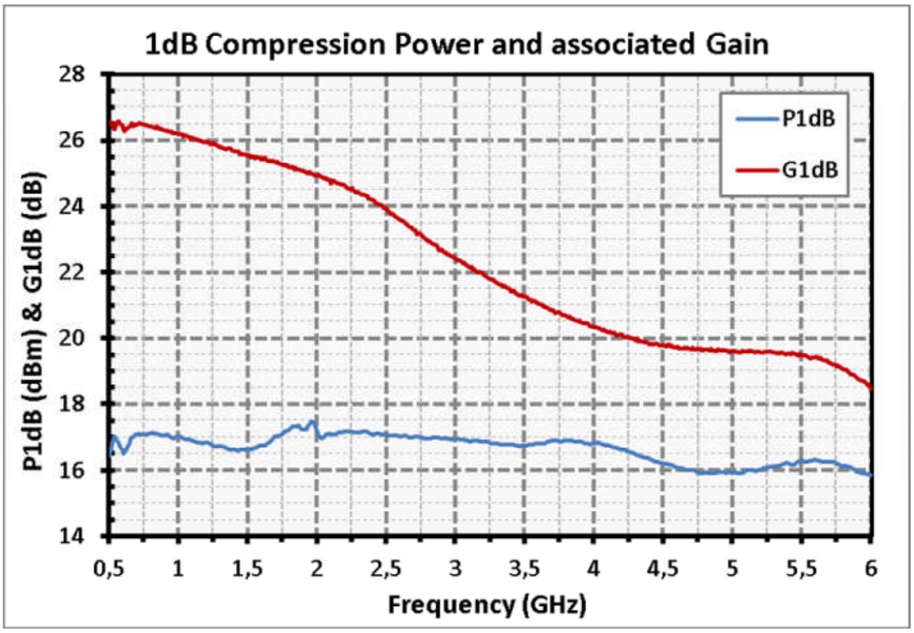

Figure 24 : Variable Gain LNA 1dB compression point

In case of OIP3 feature, it was characterized at certain relevant frequencies due to its complexity to be measured in a large number of points.

Table 14 summarizes the main features of the Variable Gain prototype.

Variable Gain LNA measurements summary							
Freq. (MHz)	**S11 (dB)**	**S21 (dB)**	**S22 (dB)**	**Att range (dB)**	**NF (dB)**	**P1dB (dBm)**	**OIP3 (dBm)**
650	-6.8	27.4	-9.3	30.8	1.95	17.0	28.5
890	-7.2	27.3	-11.3	31.1	1.86	17.1	28.7
950	-7.4	27.2	-11.9	31.1	1.86	17.0	28.8
1750	-12.5	26.2	-22.3	32.0	1.94	17.1	28.9
1840	-13.8	26.1	-19.8	32.1	1.95	17.3	29.0
1890	-14.3	26.0	-18.8	32.1	1.92	17.2	29.0
1950	-15.4	25.9	-17.5	32.2	1.94	17.5	29.0
2140	-17.5	25.7	-14.9	32.4	1.99	17.1	29.0
2450	-16.5	25.0	-13.3	32.7	2.09	17.1	29.0
3600	-11.1	22.0	-14.8	32.4	2.29	16.8	28.8
5500	-17.0	20.5	-11.1	32.7	2.42	16.3	28.7

Table 14 : Summary of the Variable Gain LNA measured features

In conclusion, all the specifications defined were fulfilled, providing some remaining gain to cover possible extra losses at the input, having a good range of attenuation control, and improving the NF requested while keeping good values of P1dB and OIP3 to ensure a suitable performance.

3.5 DCR block

After the signal is amplified from the LNA block, the next step is the down-conversion. The proposed architecture for the DCR block is presented in Figure 25 with references for each of the sub-components.

The RF signal coming from the amplification block enters the wide band RF mixer. This mixer has an operating range from 10 MHz up to 6 GHz. The local oscillator (LO) signal for this mixer comes from a wide band controlled reference clock. The Phase Locked Loop – Voltage Controlled Oscillator (PLL-VCO) operating range is between 25 MHz up to 6 GHz. Next the intermediate frequency (IF) signal at the output of the wide band mixer goes to the IF base band tunable LPF. This filter has two paths (for the I and Q channels). In our case, only one of the two paths is used. The IF filter block includes two base-band variable gain amplifiers per path, to provide increased gain at baseband frequencies. The tuning frequency for the Low Pass Filter (LPF) can be set between 3.5 MHz and 50 MHz. Once the IF signal is amplified and filtered, it goes towards the RMS power detector. This detector has a wide dynamic range at base band frequencies (up to 70 dB) and it is the main limiting component in the dynamic range and sensitivity of the whole dosimeter. Once the base-band power is converted to a voltage level, it is then sampled easily by the ADC in the microcontroller. Using a lookup table, the digital voltage level is then converted to RMS power using the characteristic of the power detector. This power can then be converted to E-field (in V/m) using the RF chain characteristics (antenna factor and RF chain gain).

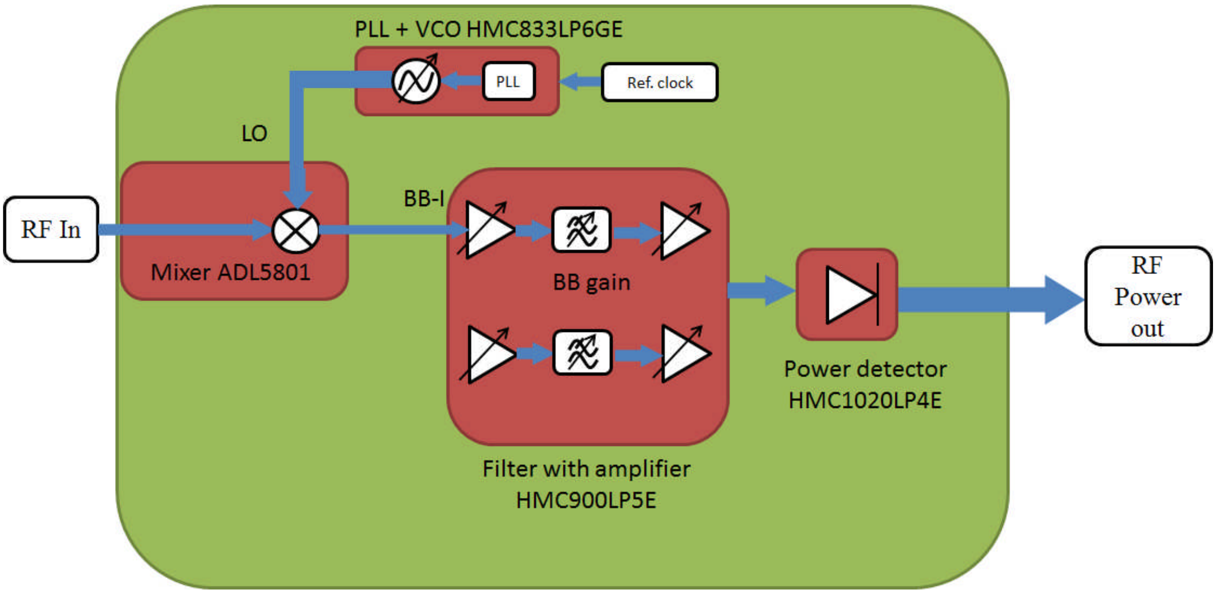

Figure 25 : Direct Conversion Receiver block diagram

Individual experimental validation of each of sub-component and the complete DCR block test results are presented in the following.

3.5.1 Wide band PLL-VCO: HMC833LP6GE

The wide band PLL-VCO [14] was tested separately at Satimo industries, Brest, France using a demo-board, a PC, and a spectrum analyzer. The test bench is presented in Figure 26 in the form of a block diagram and the actual setup.

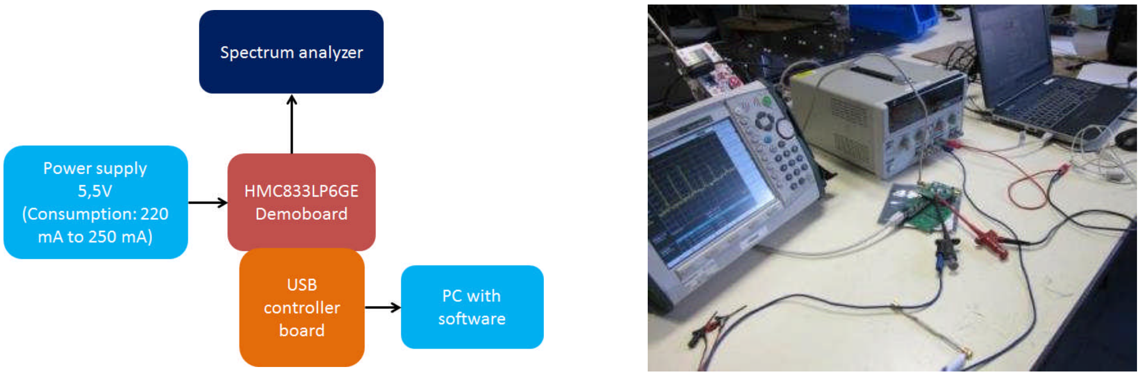

Figure 26 : PLL VCO HMC833LP6GE test bench for characterization

To characterize this component, we programmed the PLL-VCO using the software provided with the demoboard at different frequencies and studied the spectral response on the spectrum analyzer over the whole LEXNET bandwidth (up to 6 GHz). The aim was to compare the accuracy of the LO signal frequency and the harmonic levels with those specified in the datasheet. As seen in the Table 17, the total consumption of this component is around 250 mA maximum which is quite significant. This component is the most power consuming one in the LEXNET dosimeter architecture.

In the Figure 27, we present some screen shots of the spectrum analyzer at different frequencies. We can see that when the PLL-VCO is programmed to 900 MHz, it has high level of harmonics which could disturb the output of the mixer when the incoming RF signal is composed of all frequencies. To avoid this phenomenon, the output of the PLL-VCO will be filtered to suppress the harmonic levels.

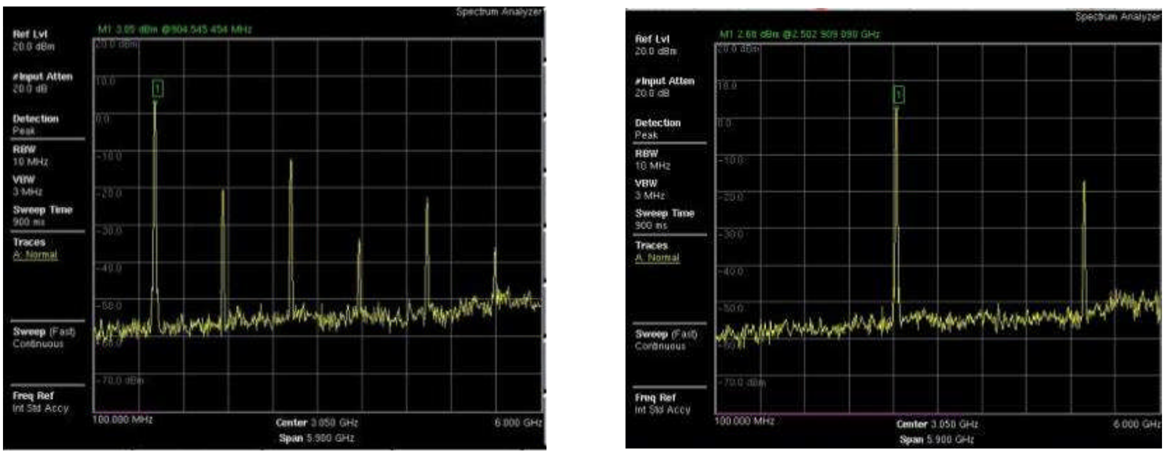

(a) (b)

Figure 27 : Output of the PLL-VCO on the spectrum analyzer for (a) 900 MHz, and (b) for 2500 MHz

Comparing the measured performance with the one in the data sheet, the harmonic levels are in good agreement as shown in Table 15.

Parameter	Condition	Min.	Typ.	Max.	Units
Harmonics for Fundamental Mode					
fo Mode at 2 GHz	2nd / 3rd / 4th		-20/-29/-45		dBc
fo/2 Mode at 2GHz/2 = 1 GHz	2nd / 3rd / 4th		-23/-15/-35		dBc
fo/30 Mode at 3 GHz/30 = 100 MHz	2nd / 3rd / 4th		-25/-10/-33		dBc
fo/62 Mode at 1550 MHz/62 = 25 MHz	2nd / 3rd / 4th		-17/-8/-21		dBc
Harmonics in Doubler Mode					
2fo Mode at 4 GHz	½ / 3rd / 4th/5th		-7/-23/-15/-40	-4/-15/-7/-28	dBc

(a)

Fundamental frequency (MHz)	Fundamental mode power at o/p (dBm)	Harmonic levels up to 6GHz with reference to the fundamental mode (dBm) 2nd / 3rd / 4th
900 MHz	3.05	-24 / -16 / -37
1800 MHz	4.97	-19 / -20
2500 MHz	2.70	-20

(b)

Table 15 : Harmonic levels for the PLL-VCO from (a) datasheet, and (b) measurements

3.5.2 Wide band mixer: ADL 5801

The wide band mixer demo board was used for its characterization. The test bench setup is shown in Figure 28. Two input RF sources were used. The RF input to the mixer comes from a wide band signal generator and the LO input from a signal generator at first and then from the PLL-VCO which was presented in the previous section. The mixer requires two power supply voltage levels. The 5 volt supply is the one which consumes 130 mA of current. The 3.8 V level can be applied using a resistive voltage divider circuit as it does not consume any current. The output of the mixer (IF frequency) was observed on a spectrum analyzer.

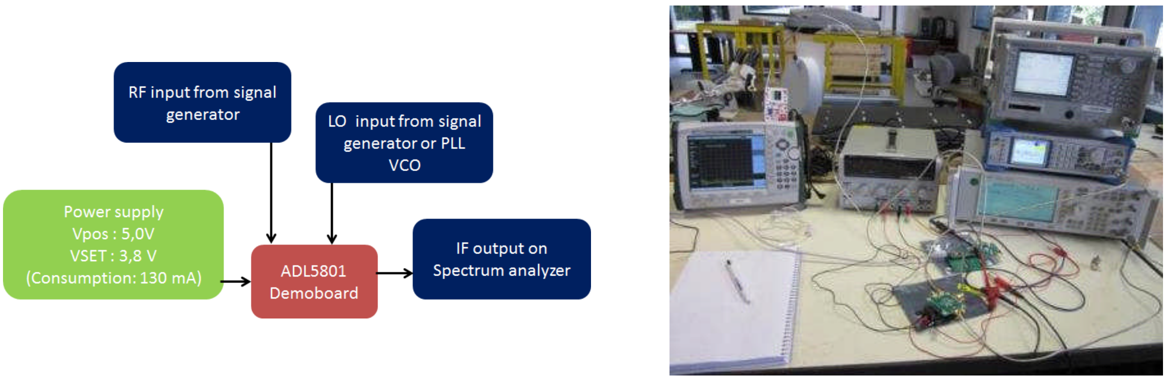

Figure 28 : Mixer ADL5801 test bench for characterization

The ADL5801 is a high linearity, doubly balanced, active mixer with operating range between 10 MHz up to 6 GHz. The IF output can vary from DC up to 6000 MHz. To characterize this mixer, we provided several input frequencies at the

RF input from the signal generator. Results from two extreme scenarios are shown in the Figure 29 below.

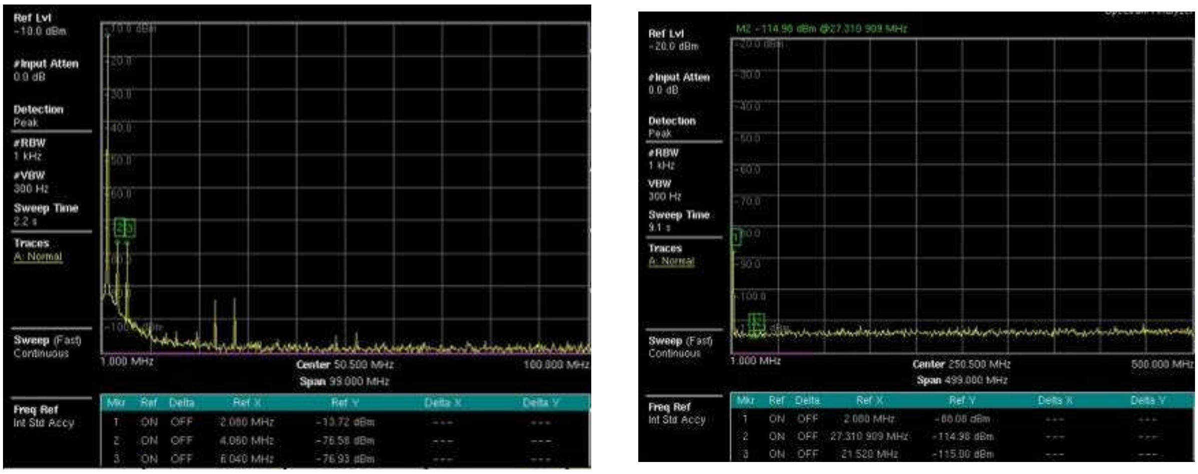

Figure 29 : Wide band mixer IF output for, (a) RF = 898 MHz @ -10 dBm; LO = 900 MHz @ 0 dBm, (b) RF = 898 MHz @ -85 dBm; LO = 900 MHz @ 0 dBm

The first case is with strong RF and LO input levels to see the harmonics at the IF output. The -10 dBm RF input level was chosen as it represents the worst case scenario for the LEXNET dosimeter. It corresponds to a maximum 5 V/m input at the dosimeter probe. The IF output (Figure 29a) shows a fundamental frequency at 2 MHz with 2^{nd} and 3^{rd} level harmonic levels around at -63 dB with respect to the fundamental frequency level. These values correspond to the ones announced in the datasheet.

Next a very low level RF input was used (-85 dBm), while the LO input levels remained the same as in the previous case. This RF level corresponds to the 5mV/m E-field at the dosimeter probe input (sensitivity level). The results (Figure 29b) show that the fundamental IF level is still at 2 MHz, with harmonics below the noise floor.

3.5.3 Tunable low pass filter: HMC900LP5E

The programmable LPF was evaluated using the demoboard and the software provided with it. The test bench setup is presented in Figure 30. This filter has two RF chains for use as I and Q channels. In our case, we need only one of the two filter chains. Hence, one of the RF chain was switched off. This reduces the current consumption by about 60 mA. The total consumption is thus 90 mA for this component.

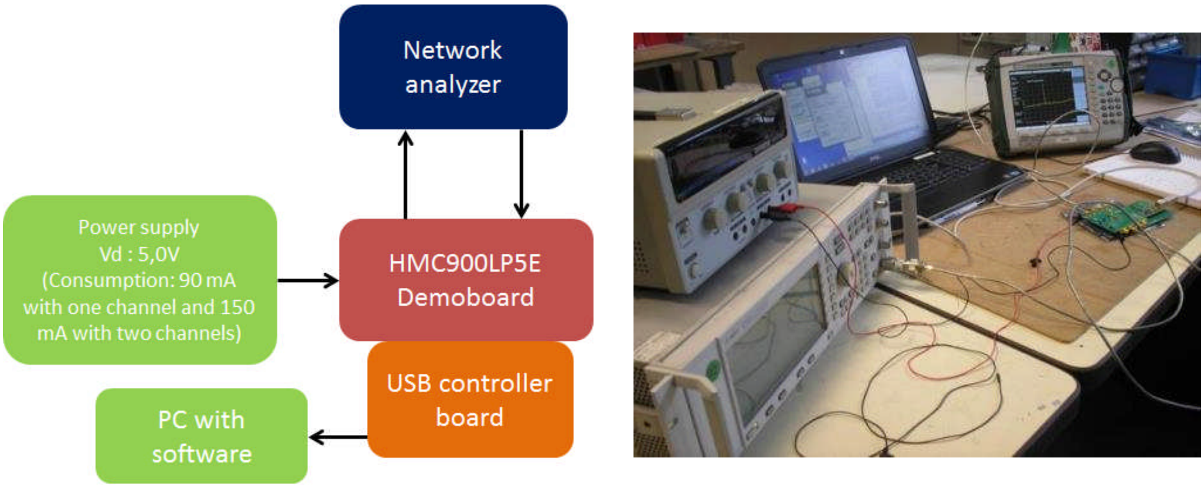

Figure 30 : Tunable low pass filter HMC900LP5E test bench for characterization

To evaluate this programmable filter, it was connected to a network analyzer and the software was used to program different cut-off frequencies. The results are compared in the Figure 31 below.

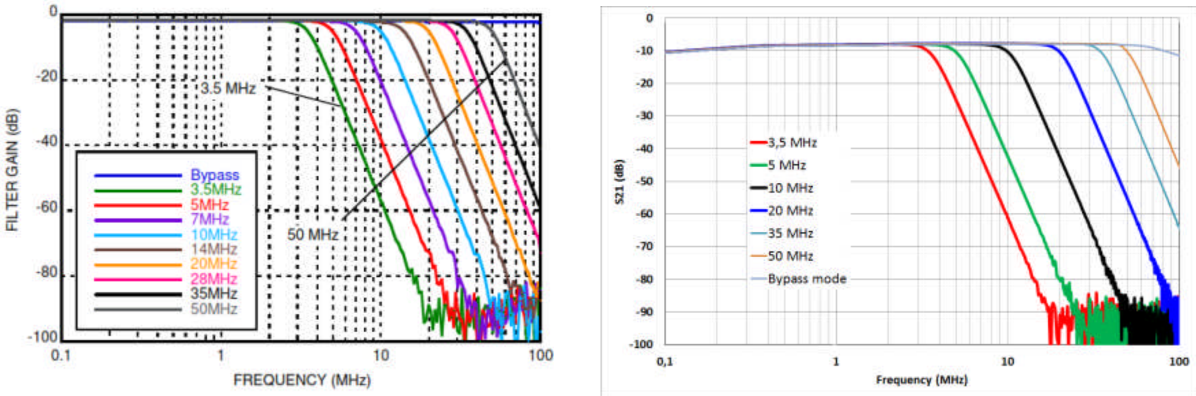

(a) (b)

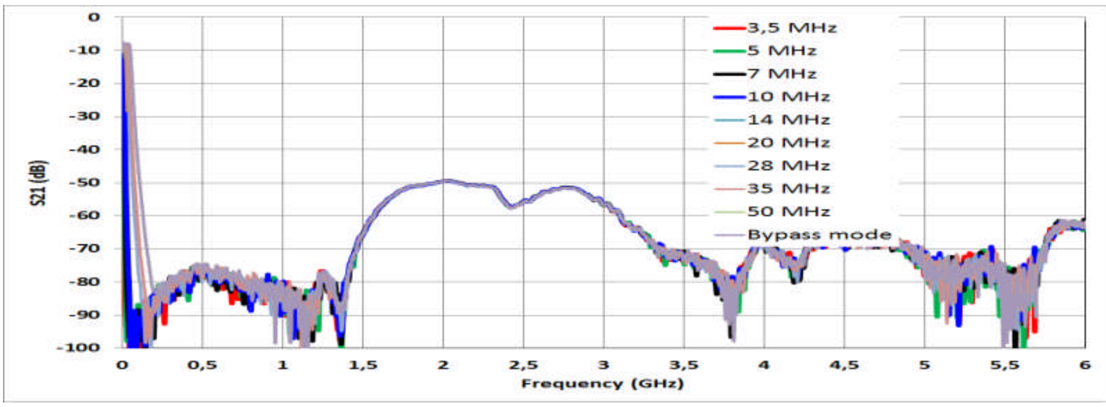

(c)

Figure 31 : Tunable low pass filter results from network analyzer, (a) datasheet, (b) measurements over narrow band, (c) measurements up to 6 GHz.

The results are in excellent agreement in terms of rejection levels. The loss of about -9 dB observed in the measurements is due to fact that there is an attenuator of -19.8 dB at the output of the low-pass filter demoboard (not taken into account for the results in the datasheet). And with the gain set at maximum of 10 dB, we find the -9dB value as observed in the measurements. The measurements up to 6 GHz are shown in Figure 31c which shows minimum attenuation levels of about 50 dB over the whole frequency band.

3.5.4 RMS power detector: HMC1020LP4E

The final component in the RF chain is the RMS power detector. The test bench for its characterization is presented in Figure 32. A 5v power supply is needed for the power detector with the consumption varying between 50 and 60 mA corresponding to the input power level. The input RF signal was generated using a signal generator. The output was observed on a voltmeter.

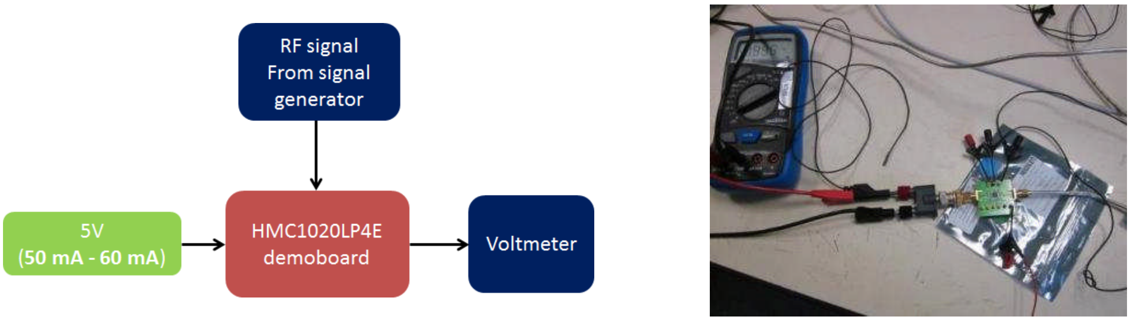

Figure 32 : RMS power detector HMC1020LP4E test bench for characterization

To evaluate this component, the RF input signal was varied over the IF frequency band (up to 100 MHz). The power levels were varied for each test frequency between -70 dBm and +10 dBm. The datasheet had results starting from 100 MHz up to the 3.9 GHz limit. After exchange with the suppliers, we managed to acquire results for the power detector for frequencies below 100 MHz. For these frequencies, the DC coupling capacitors at the detector input were changed to 10 µF (from 1 nF initially). The results are shown in Figure 33 below. Excellent agreement is observed with a measured dynamic range of more than 70 dB.

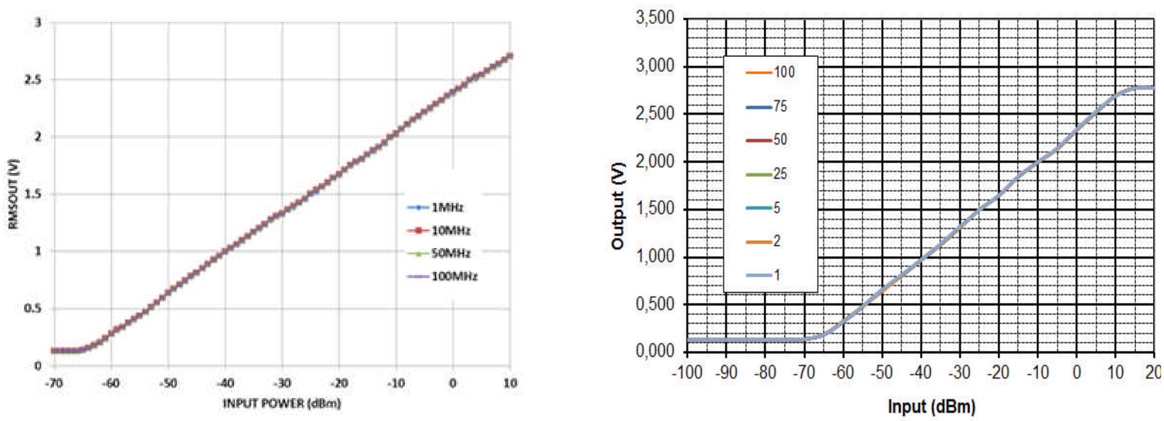

(a) (b)

Figure 33 : RMS power detector results from (a) datasheet, (b) measurements

3.5.5 DCR block measurements in CW

After validation of each of the individual components of the DCR block, several tests were carried out in cascading the whole DCR chain.

The first test was carried out with a two-tone RF input using two-signal generators (RF1 and RF2) and a power combiner circuit. The two-tone input signal was injected into the wide band RF mixer. The LO signal was provided through the programmable PLL-VCO. The output from the mixer (IF frequency) was connected to the tunable LPF. Finally the output of the filter was connected to the RMS power detector. The output of the power detector was observed on the oscilloscope. The test bench setup is presented in Figure 34 below.

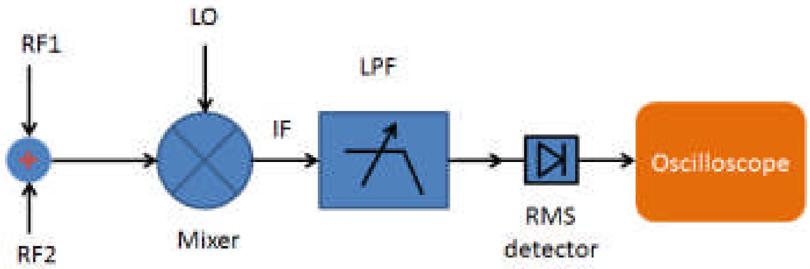

(a)

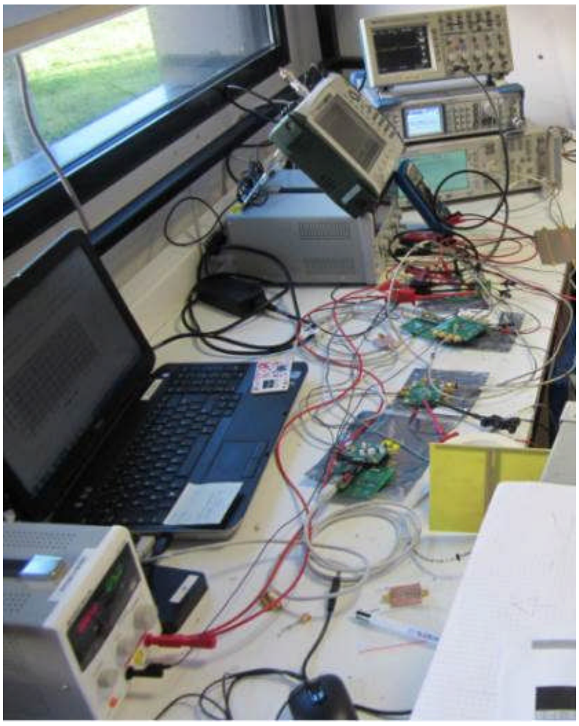

(b)

Figure 34 : Test bench setup for two-tone RF input characterization of the DCR block

The total current consumption of the DCR block was around 470 mA with two voltage levels of 5 V and 3.8 V. The 3.8 V level did not draw any current.

The RF1 frequency was set to 905 MHz and RF2 at 895 MHz. Both RF signal power levels were fixed at -50 dBm at first. The LO signal was fixed at 900 MHz at -10 dBm from the PLL-VCO. This corresponds to the worst case scenario, when the LO frequency is in the middle of two RF signals. Both signals when down-converted to baseband at the same frequency (IF = RF2 – LO = LO – RF1), generates a modulation which gives an incorrect reading of the total power. This problem can be avoided using an appropriate integration time for the RMS power detector. The power detector integration time was then varied using the 4bit-digital inputs from minimum (corresponding to 0000) to intermediate (1000) values. The LPF was programmed for a cut-off frequency of 5 MHz.

The RF1 and RF2 sources were switched ON and OFF and the behavior of the output voltage signal after the power detector was observed through an oscilloscope. The results are summarized in the Table 16 below.

	RMSOUT Rise-Time 10% -> 90% (µs) [3]			RMSOUT Rise Settling Time (µs) [2]			RMSOUT Fall-time 100% -> 10% (µs) [4]		
SCI4,3,2,1	Pin = 0 dBm	Pin = -20 dBm	Pin = -40 dBm	Pin = 0 dBm	Pin = -20 dBm	Pin = -40 dBm	Pin = 0 dBm	Pin = -20 dBm	Pin = -40 dBm
0000	0.0686	0.044	0.053	0.509	0.504	0.257	0.969	0.975	1
0010	0.0684	0.05	0.093	0.54	0.524	0.6788	2.98	3.193	3.35
0100	0.076	0.066	0.878	1.956	1.872	2.82	13.5	14.18	14.978
0110	1.624	3.432	4.84	7.8	8.056	8.92	62.9	65.384	69.224
1000	8.6	15.32	23.4	35.52	37.28	40.92	294.64	304.52	317.32
1010	38.6	65.8	109.6	165.2	156	188	1379.4	1423.6	1477.6
1100	186	325	509	802	770	831	6447	6640	6881

(a)

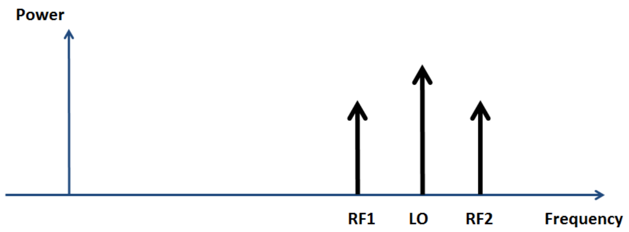

(b)

RF1 (905 MHz, -50 dBm)	RF 2 (895 MHz, -50 dBm)	LO (900 MHz, -10 dBm)	LPF cut off (MHz)	Power detector integration time (SCI-4321)	Output at Oscilloscope (V)
ON	OFF	ON	5	1000	0,608 (Stable o/p)
OFF	ON	ON	5	1000	0,656 (Stable o/p)
ON	ON	ON	5	1000	0,732 (Stable o/p)
ON	ON	ON	5	0000	0,9 (modulated o/p)
ON	OFF	ON	5	0000	0,644 (modulated o/p)

(c)

Table 16 : Results for two-tone RF input to the DCR block (a) integration time setting for the power detector from the datasheet, (b) RF and LO inputs, (c) summary of measured results.

It can be observed from the above results that as the integration time is increased the output of the power detector becomes more stable. The screenshot from the oscilloscope corresponding to four interesting cases are shown in the Figure 35 below.

RF1 / RF2 States | Output with minimum Integration time setting (0000) | Output with intermediate Integration time setting (1000)

ON / OFF

ON / ON

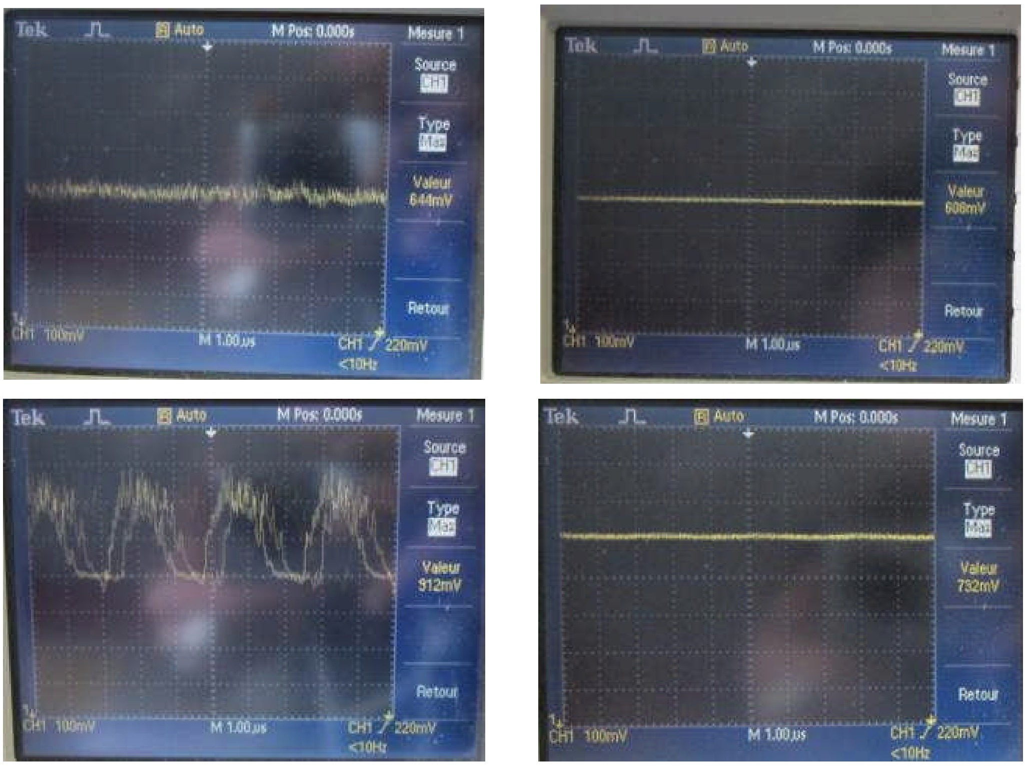

Figure 35 : Screen shots of the oscilloscope showing the output of the power detector for different cases.

From the above results, the importance of selecting an appropriate integration time for the power detector is highlighted. Even for a single tone RF input, using a small integration time gives a noisy result. For a two-tone RF input, with the LO in between the two tones, the output is highly modulated. Using an appropriate integration time suppresses the modulated signal and gives us a correct reading. It can be observed that the difference between the output levels, when we have a single tone and two-tones with same input power, corresponds to 3 dB (as expected).

3.5.6 DCR block measurements in real scenario

To validate the proposed DCR block architecture in a real scenario, a test bench was setup as presented below in Figure 36. A mobile phone calling a landline number was placed at about 1.2 meters from a receiving GSM antenna. The antenna was connected directly to a spectrum analyzer at first to obtain reference signal level for comparison.

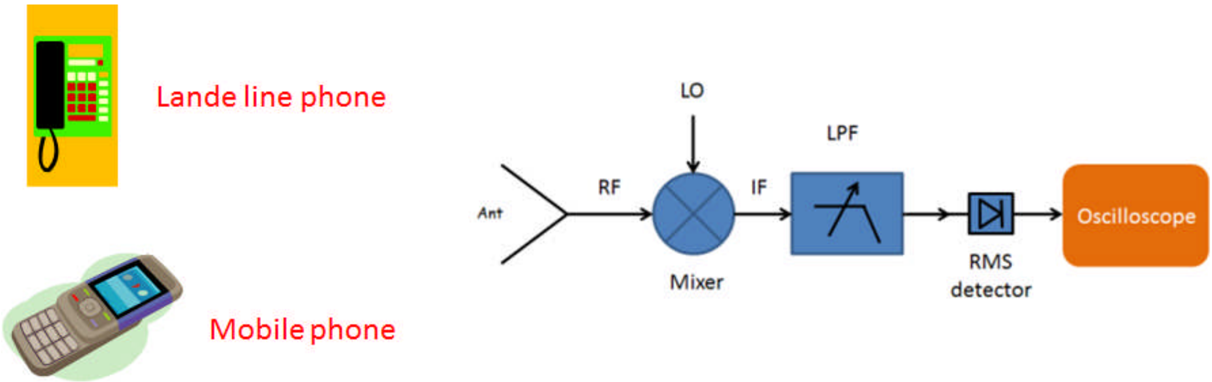

(a)

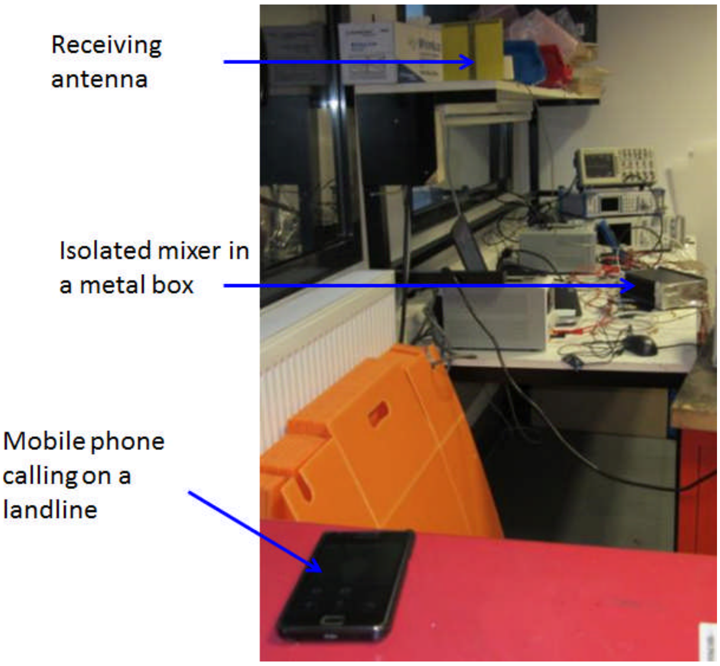

(b)

					Bouygues			Orange			Free			SFR		
	Center	Start	End	BW (MHz)	Start	End	BW (MHz)	Start	End	BW (MHz)	Start	End	BW (MHz)	Start	End	BW (MHz)
GSM 900 UL	895	880	915	35	880	890	10	890	900	10	900	905	5	905	915	10
GSM 900 DL	947	925	960	35	925	935	10	935	945	10	945	950	5	950	960	10

(c)

Figure 36 : Test bench setup DCR block test with real scenario, (a) block diagram, (b) photograph of the test bench, (c) GSM frequency band distribution in France.

The screenshot for the reference measurement, when the mobile is calling a landline number is presented in Figure 37. These results were obtained using the max-hold capture option on the spectrum analyzer. The first peak occurs instantaneously while the second peak is captured a bit later. The peak signal observed from the reference measurement is about -20 dBm. The frequency band extends from 895 MHz up to 900 MHz for the two peaks.

The LO frequency was set in the middle of the operator band (verified from the reference measurements). The output was observed on the oscilloscope. The objective was to detect successfully the GSM UL signal using the DCR block for the target operator. The GSM UL frequency range of the operator in question is between 890 – 900 MHz (Figure 36c). The LO was thus set to 895 MHz at first, and then varied to other center frequencies corresponding to other GSM UL operator frequencies. The rejection with other frequency bands could thus be evaluated in a real scenario.

The test in DL scenario could not be carried out using the complete DCR block, as the received signal strength was well below the power detector sensitivity levels, and a LNA would be required at the front end.

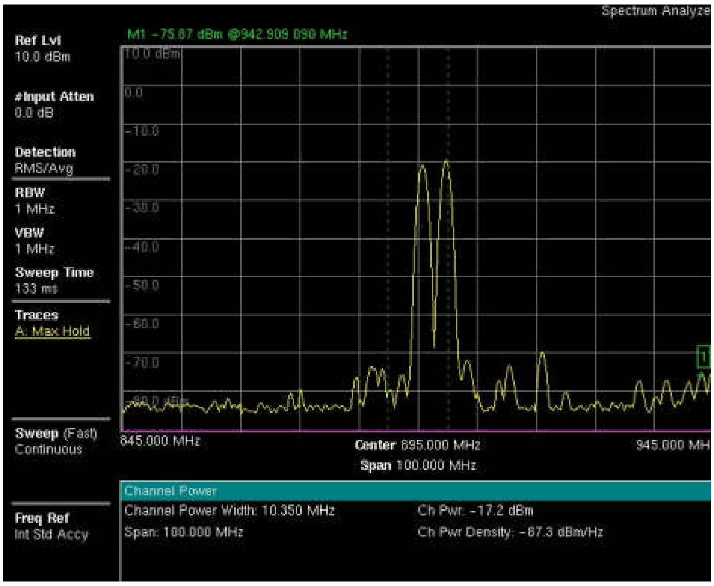

Figure 37 : Result from the reference measurement with the mobile calling a landline number after 1 minute of measurements with max-hold.

Next, the antenna is disconnected from the spectrum analyzer and is connected directly to the RF input of the DCR block (Figure 36a) while the mobile position is not changed and the call is not disconnected. The LO frequency is locked to 895 MHz (center frequency of the operator band from 890 MHz up to 900 MHz). The output on the oscilloscope is shown in Figure 38.

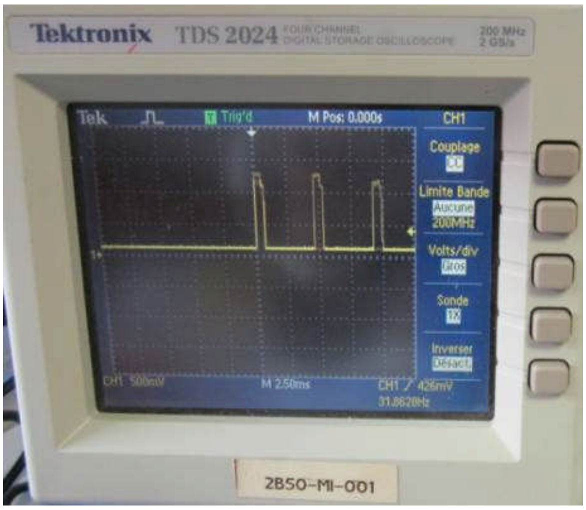

Figure 38 : Output of the DCR block on the oscilloscope with LO frequency locked to 895 MHz.

From the output of the oscilloscope (Figure 38), a clean GSM time domain signal is detected. The peak level of this detected signal is 1.22 V. Using the reference curve for the power detector (Figure 33), the output power is about -33 dBm. Subtracting the RF path losses in the DCR block (measured to be around -13 dB at 900 MHz), we obtain an input power level of -20 dBm at the receiving antenna. This is the same as the reference measurement level (Figure 37). To determine the rejection in adjacent operator bands, the LO frequency is changed and the output of the power detector is measured. The results are summarized in the Table 17 below.

Mobile	Landline	LO (MHz)	LPF (MHz)	DET o/p (V)	Power (dBm) From detector curve	Power at antenna output (dbm)
Calling	Receive	885	5	0	< 65	--
Calling	Receive	890	5	0,9	-42	-29
Calling	Receive	895	5	1,22	-33	-20
Calling	Receive	900	5	1,14	-35	-22
Calling	Receive	905	5	1,2	-34	-21
Calling	Receive	910	5	0,11	< -65	--
Calling	Receive	915	5	0	< -65	--

Table 17 : Output of the power detector for different LO frequency locks in the scenario studied in Figure 36.

Table 17 provides interesting results. As the LO is locked to center frequencies of different operators, the output of the power detector changes according to the rejection provided by the tunable low pass filter. The power at the antenna output (last column in the Table 17 above) is calculated by adding the 13 dB losses in the RF chain (from measurements at 900 MHz). These losses are due to the 19 dB attenuator present at the output of the low-pass filter.

When the LO frequency is locked to the center frequency of the first operator (at 885 MHz), the detector output is about 0 volt, which means there is no signal detected. When the LO moves to the center of the second operator frequency band (i.e. at 895 MHz), the signal is correctly detected (at -20 dBm). Moving 5 MHz below and 5MHz above this frequency, the signal still falls inside the low-pass filter bandwidth. That is why when the LO is locked to 905 MHz (third operator), we still detect a -21 dBm signal level, because the signal from the second operator is at 900 MHz (Figure 37), and falls in the LPF bandwidth. To correctly reject this band, we need a LPF with lower cut-off frequency (< 1.5 MHz). With the actual solution, we can correctly distinguish between the operators if there is a 10 MHz difference between their frequencies. Moving towards the center frequency of the fourth operator (910 MHz), a small signal level is observed, but it has sufficient rejection for it to be outside the power detector range.

To detect the third operator with a 5MHz frequency band (900 MHz – 905 MHz from Figure 36c), the low-pass filter is set to 3.5 MHz cut-off frequency (the minimum possible with the current available demoboard). This frequency does not reject sufficiently the signal at 5 MHz (about 15 dB of rejection). This means that if we want to detect an operator frequency with a frequency band of 5 MHz, we will have also some part of the adjacent operator. To solve this problem and to correctly detect the signals of the target operator, the following simple scheme is proposed.

The LEXNET dosimeter will be used to carry out measurements for the DL exposure essentially. Thus we will have a total of 8 frequency standards to measure defined in Table 18 below.

					Bouygues			SFR			Orange			Free		
	Centre	Start	End	BW (MHz)	Start	End	BW (MHz)	Start	End	BW (MHz)	Start	End	BW (MHz)	Start	End	BW (MHz)
LTE bande XX DL	806	791	821	30	791	801	10	801	811	10	811	821	10			
GSM 900 DL	947	925	960	35	925	935	10	950	960	10	935	945	10	945	950	5
DCS 1800 DL	1842	1805	1880	75	1853	1880	27	1805	1808	3	1808	1832	24			
								1832	1853	21						
UMTS DL	2140	2110	2170	60	2125	2140	15	2110	2125	15	2140	2145	5	2145	2150	5
								2150	2155	5	2155	2170	15			
Wifi	2450	2400	2483,5	83,5												
LTE bande VII DL	2650	2620	2690	70	2655	2670	15	2620	2635	15	2635	2655	20	2670	2690	20
Wimax	3600	3300	3900	600												
Wifi 5 G	5500	5150	5850	700												

Table 18 : DL exposure target frequency bands (e.g. France spectrum) for the LEXNET dosimeter

The first 6 bands will be measured through the DCR block. The last two bands (due to larger bandwidths) will be measured using fixed filters. Thus, this leaves us with only 6 frequency bands to be measured using the DCR block. These six bands are further divided among the service providers. The distribution in France is shown in Table 18 above among the four operators.

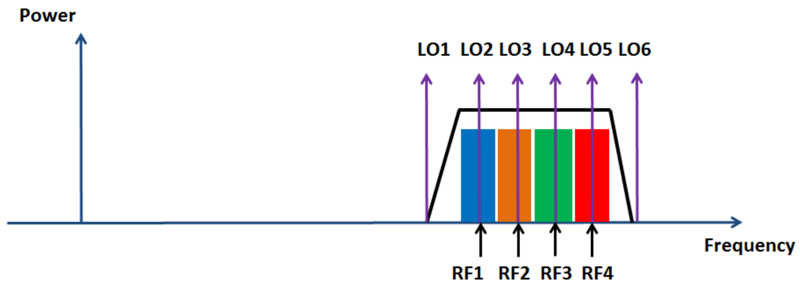

Figure 39 : Measurement scenarios with the DCR block and LO frequency positions for measurements.

Now looking at a typical scenario, we have four operators inside one frequency standard. To correctly detect each of the four operators, the LO frequency needs to be set at 6 different frequency points as shown in Figure 39. These positions will give us six measurements in base band. Knowing the rejection of the LPF, we can calibrate the measurements to correctly separate the response from each operator.

3.6 Microcontroller

After studying the control signals required for the whole dosimeter and characteristics requirements of each component, a suitable microcontroller component was identified. The ST microelectronics reference STM32F103 offers all the necessary driving system and connectivity, i.e. SPI bus, ADC, USB, GPIO, and UART.

This microcontroller is a 32 bit system with speeds up to 72 MHz for different calculations. The total size of the microcontroller depends on the total control signals that we will need. Two solutions are considered; either *i)* a single microcontroller chip will be used which will drive all the control signals (up to 80 control signals are available), or *ii)* an I/O expander will be used with a small size microcontroller for driving all controls.

3.7 Memory block

Two memory blocks will be used for the LEXNET dosimeter. One of them will be used for the storage of all the required parameters for driving the dosimeter for different configurations, and the other one for storage of the measurements.

Both memory slots will be of EEPROM type so that even when the power supply is disconnected, the data on is not erased. The memory chip size will be determined depending on the data necessary to store for the dosimeter configuration and for the measurements.

3.8 Bluetooth / USB connectivity block

The Bluetooth module identified for connectivity with the mobile devices is developed by Roving networks RN-42. This module requires very low power and is easily driven using an UART interface.

The connectivity block has a mini USB connector and the device reference identified for the LEXNET dosimeter is Molex 54819-0519.

3.9 Integration proposal for the LEXNET dosimeter

The integrated front end of the dosimeter is presented in detail in the form of an electrical diagram in Figure 40. The purpose is to show the different sub-components of the RF chain up to the power detector before the signal is sampled by the ADC in the microcontroller (Figure 4).

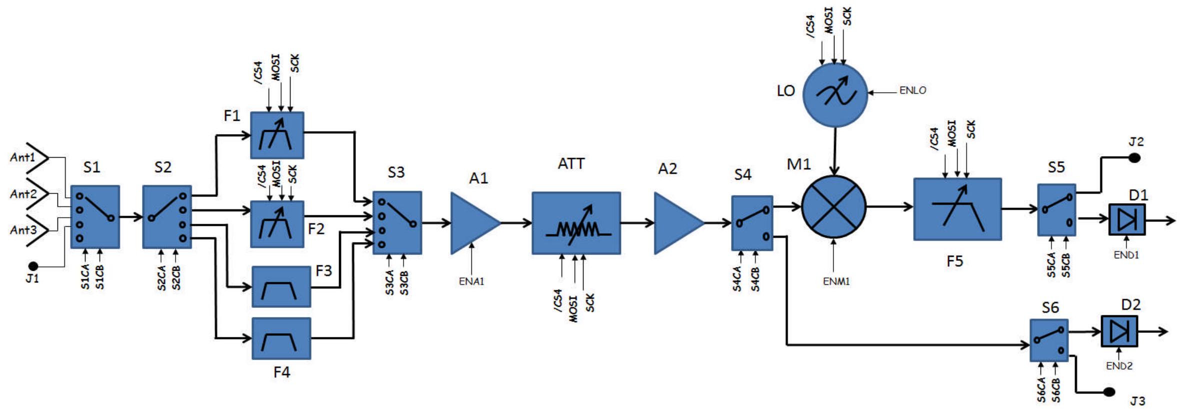

Figure 40 : Electrical diagram of the RF front end of the dosimeter

Starting from the left side, first we have the three antenna probes along with an RF connector for calibration and debugging purposes. A four-way RF switch *S1* allows us to select among the three antenna probes or the debugging switch J1. Then two four-way switches *S2* and *S3* select one of the four filters (*F1* to *F4*). *F1* and *F2* are the tunable filters as presented in section 3.3. F3 and F4 are fixed filters for detection of the WiMAX and WLAN 5GHz frequency bands.

The amplification block consists of *A1*, *ATT* and *A2* as described in section 3.4. After that, a two-way switch *S4* separates the DCR block, used for measurements up to 3 GHz, from the measurements of the WiMAX and WLAN 5GHz frequency bands. The DCR block is composed of the mixer *M1*, the PLL-VCO designated as *LO*, and the tunable LPF *F5*. A two-way switch *S5* selects between the second debugging RF connector (*J2*) and the LPF output. Power detector *D1* is used for measurements up to the 3 GHz frequency bands. The RMS power detector *D2* is used for measurements for WiMAX and WLAN 5GHz frequency bands and is chosen using the two-way switches *S4* and *S6*. The debugging RF connector J3 is used for characterizing the RF chain for the two highest frequency bands. The output of *D1* and *D2* then goes through to the ADC of the microcontroller.

The characteristics of each of the sub-component of the dosimeter are summarized in the Table 19 below from individual component measurements and from datasheet specifications.

	Component func. & model	Reference	Operating bandwidth	Gain (dB) Typical	Voltage supply (typ) V	Current supply (typ) mA	Current supply (Max at startup) mA	Control circuit	Enable / disable voltage + current	On / Off time	Estimated size in mm (x * y * z)
1	SP4T HMC344LP3E	S1,S2,S3,	DC- 8GHz	-1,8	-5	3	6	0V off , -5V ON		150 ns	3x 3x 1
2	SPDT HMC536MS8G	S4,S5, S6	DC- 6,0 GHz	-0,8	+3,3	0,025	0,025	0V off, 3,3 Volts ON TTL	0,025	30 ns	5 x 3 x 1,3
3	Programmable band pass filter CEA-LETI	F1	700 MHz – 960 MHz	-7	+3,3	0.18	0.18	SPI	Standby 0.12mA	20 us	16*16*4
4	Programmable band pass filter CEA-LETI	F2	1,8 GHz – 2,7 GHz	-9	+3,3	0.84	0.84	SPI	Standby 0.15mA	70 us	16*16*4
5	WiMAX filter DEA203600BT	F3	3,3 GHz - 3,9 GHz	-1,4							2 x 1,25 x 0,95
6	WLAN 5GHz filter DEA205425BT_2028A4	F4	4,9 GHz - 5,95 GHz	-1,6							2 x 1,25 x 0,95
7	LNA VMMK2303	A1	0,5 GHz - 6 GHZ	14	1.8V	21mA	28mA	0V off, 1.8V ON	0V off 0.02mA, 1.8V on 21mA	NA	1x0.5x0.25
8	Attenuator HMC624LP	ATT	DC- 6GHz	-2,8	0V & 5V	2mA	2mA	SPI	-	150ns	4x4x1
9	Driver PGA-1021+	A2	0.05- 6GHz	12	3.3V	52mA	60mA	-	-	-	4.6x4.2x1.6
10	Mixer ADL5801	M1	10 MHz - 6 GHz	0	5 V & 3,8V	130 mA @ 5V 0mA @ 3,8V	200 mA		5V off, 0V ON 50 mA off current	182 ns / 28 ns	4 x4 x 1
11	PLL-VCO HMC833LP6GE	LO	0,025 - 6 GHz	-5	3,3 V & 5V	220 total 170 mA @ 5V 50 mA @ 3,3 V	250	SPI	0V off, 5V ON TTL	250 us	6 x 6 x 1
12	VGA + LPF HMC900LP5E	F5	3,5 MHz-50 MHz	10	5	70	150	SPI	Through SPI	250 us	5 x 5 x 1
13	Power detector HMC1020LP4E	D1	DC- 3,9 GHz		5	50	60	TTL	5V off, OV ON, 5mA off current	44 ns / 1 us	4 x 4 x1
14	Power detector ADL 5902	D2	DC- 9 GHz		5	73	90	TTL	0V off, 5V ON, 0,3mA off current	5 us /3 us	4 x 4 x1
15	Microcontroller				3,3		100				

Table 19 : Power consumption, size, and time delay estimation for the LEXNET dosimeter

3.10 Battery design

To identify a suitable battery size, the power consumption of all the components in the LEXNET dosimeter discussed above was evaluated. The required voltage levels, current consumption, time delays for different components were estimated from the Table 19 above. These values were evaluated from demo-board measurements and datasheet specifications.

From the above table, the total typical current consumption for the dosimeter is estimated to be between 650 mA (with D1) and 690 mA (with D2). The peak current of 890 mA can be expected. Voltage levels of +5V, -5V, and 3.3V will be required through regulators or battery supply. The voltage levels of 1.8V and 3.8V will be provided through resistive dividers as they do not draw large current levels.

Figure 41 : Flat battery identified for the LEXNET dosimeter

The suitable battery with a flat profile and small size identified for the LEXNET dosimeter is presented in Figure 41 below. The reference number for this component is LPC884765 [15]. It has a capacity of 3000 mAh and provides a stable 3.7 V level.

The size of this battery is 68 mm x 46 mm x 8.5 mm with a weight of 52 g. A battery with larger capacity (3700 mAh for example) is also available and will increase the operational time of the dosimeter, but it was not available with a demoboard at the time of the study.

3.11 Mechanical design proposal

A preliminary mechanical structure proposed to enclose the RF board, the battery, and the probe is proposed in the Figure 42.

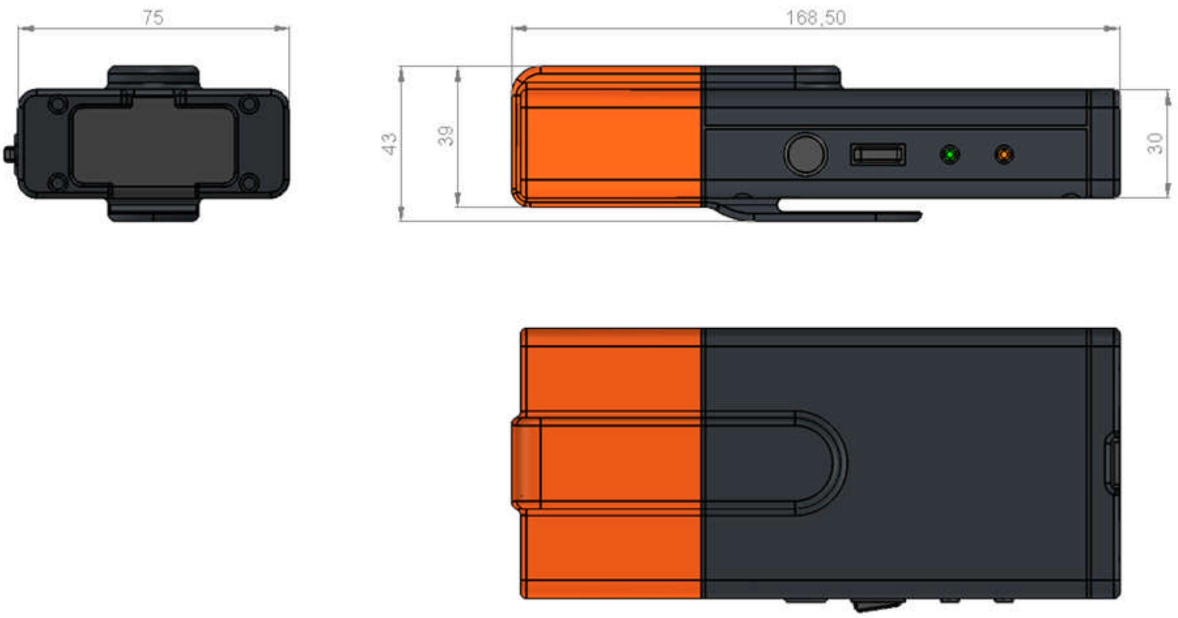

Figure 42 : Proposal for the mechanical structure for the LEXNET wearable dosimeter

The dimensions of this preliminary design are 75 mm x 168.5 mm x 43 mm (including the belt clip). There are two buttons and two LEDs on the side of the dosimeter. The circular button is designed for starting or stopping the measurement cycle. The rectangular button is used for switching on/off the device. One of the LED shows the state of the battery charge and the other the measurement cycle.

The USB and charger connectors are at the bottom behind a protective cover in order to achieve the IP67 standard.

4 CONSOLIDATED RESULTS ON WEARABLE DOSIMETER CHARACTERIZATION AND ENVIRONMENT IMPACT STUDY

4.1 Goals and approach description

The EMF exposure of the population due to wireless communications (2G, 3G, 4G and WLANs) originates both from DL emissions incoming from Base Stations (BS) and Access Points (AP), and from Up-Link ones produced by the terminals (cell phones, tablets and lap-tops). Although the main peak contribution comes generally from the last, the former must be considered as well, as contributions can be competitive for some cases for which both levels are low (e.g. in femtocells). Note however that in this case, the EMF levels are particularly low. In any case, DL emissions are continuous (and undergone by non-user as well) whereas UL ones are time limited.

This section addresses the issue of the field level assessment and more specifically its evaluation with dosimeters. The main technical challenge resides in the modelling of the measurement errors of body-worn sensors, induced by proximity effects, notably the shadowing effect of the body.

The section is organized as follows: first measurements of a triaxial sensor, both isolated and body-worn are analysed twofold, with a polarimetric approach on the one hand, and with a non-polarimetric one on the other hand; then, these analyses are carried on and deepened thanks to 3D electromagnetic simulations with realistic numerical anthropomorphic phantoms, which offer a greater flexibility regarding the possible “scenarios” (notably with regards to the “population variability” and the sensor positioning).

Simulations with simplified numerical models are addressed in order to reduce the simulation time and allow the opportunity to assess a large variability of different configurations. This task is still on-going and will be included in the second version of this deliverable.

Possible correction strategies are eventually rapidly drawn, but will be deepened in the second version.

4.2 Preliminary measurements

Measurements were carried out in an anechoic chamber with an EME Spy 140® dosimeter comprising a three-axial sensor, first isolated (Figure 43), and second placed near a whole body phantom (Figure 56). Various positions on the phantom were considered.

The analysis of the isotropy variance of both the isolated and worn sensor is presented in the following sections. For both cases, the polarimetric characteristics are first presented, followed by non-polarimetric approaches, “intrinsic” as a first step, then including the characteristics of the propagation channel for various environments.

4.2.1 Isolated triaxial sensor

4.2.1.1 Polarimetric approach

The triaxial sensor provided by Satimo was characterized in reflection and transmission for each probe axis (Figure 44) over 0.5 – 6.5 GHz.

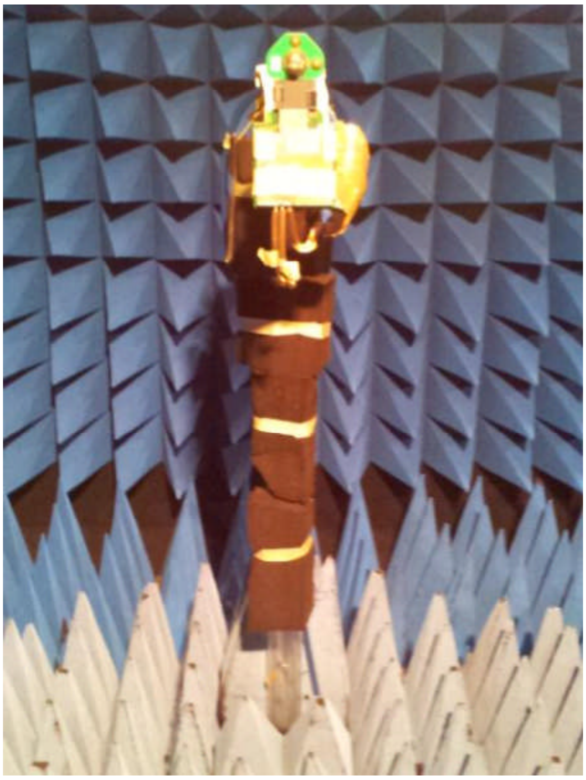

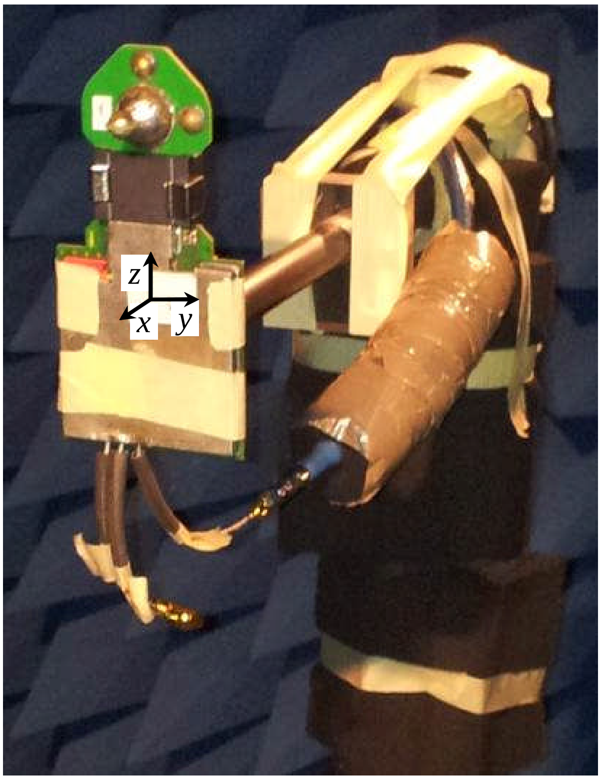

Figure 43 : Experimental setup for the measurement of the isolated sensor in anechoic chamber.

Although used in reception by essence, the sensor can be first characterized in emission. Indeed, the received signal at each probe port n can be written as [16]:

$$b_n(f,\hat{\mathbf{r}}) = e^{-j\mathbf{k}_i\cdot\mathbf{r}}\sqrt{\frac{4\pi}{\eta_0}}\mathcal{H}_n^R(f,\hat{\mathbf{r}})\cdot\mathbf{E}_i(\mathbf{k}_i,\mathbf{r}) = -\frac{1}{2}j\sqrt{\frac{4\pi}{\eta_0}}\frac{c}{\omega}\mathcal{H}_n^T(f,\hat{\mathbf{r}})\cdot\mathbf{E}_{i0} \tag{3.11.1}$$

where $\mathcal{H}^R$ (resp. $\mathcal{H}^T$) are the antenna transfer functions in the receiving (resp. transmitting) modes, η_0 the free space impedance, r the radial distance, $\hat{\mathbf{r}}$ the unit radial vector, $\omega = 2\pi f$ the angular frequency, $\mathbf{k}_i$ the wave vector of the incident plane wave $\mathbf{E}_i$ and $\mathbf{E}_{i0} = \mathbf{E}_i(f,0)$ denotes the field at the origin chosen at the centre of the sensor spherical ground. Apart from a frequency scaling, the directional and polarization characteristics are the same in both modes.

The definition used for the Tx Antenna Transfer Function (ATF) is recalled hereafter for clarity:

$$\mathbf{E}_n^{\infty}(f,\hat{\mathbf{r}}) = \frac{e^{-jkr}}{r}\sqrt{\frac{\eta_0}{4\pi}}\mathcal{H}_n^T(f,\hat{\mathbf{r}})\,a_n \tag{3.11.2}$$

where a_n is the incident wave at the n-th probe port, k the wavenumber, and $\mathbf{E}_n^{\infty}$ the radiated Far Field (FF).

The radiation characteristics (polarimetric realized gain $G_r^{\theta,\varphi} = \left|\mathcal{H}_{\theta,\varphi}^T\right|^2$) are provided hereafter for each communication band of interest, i.e. the main current RATs: GSM 900, GSM 1800, UMTS (1.9 – 2.15 GHz), LTE 800 (0.7 – 0.8 GHz) & 2600 (2.6 – 2.7 GHz), and WiFi 2G (2.4 – 2.5 GHz) & 5G (5.15 – 5.85 GHz). The results are averaged over each frequency band, and normalized to the average of the realized gain in azimuth for each polarization, i.e.:

$$\hat{G}_r^{\theta,\varphi}(f_{RAT},\theta,\varphi) = \int_{\Delta f_{RAT}} G_r^{\theta,\varphi}(f,\theta,\varphi)\,df \Big/ \frac{1}{2\pi}\int_{\Delta f_{RAT}}\int_0^{2\pi} G_r^{\theta,\varphi}(f,\pi/2,\varphi)\,d\varphi\,df \tag{3.11.3}$$

This allows to focus on the isotropy variance considering polarization aspects.

The input matching is presented in Figure 44 and the realized gains in Figure 45. The antenna factors (AF) are shown in Figure 46; AF is defined as:

$$AF = \frac{E_{i0}}{V_r} = \left(\frac{4\pi\eta_0 f^2}{G_r Z_{ref} c^2}\right)^{1/2} = \frac{1}{\sqrt{4\pi}}\sqrt{\frac{\eta_0}{Z_{ref}}}\frac{1}{\left|\mathcal{H}^R\right|} \tag{3.11.4}$$

Radiation patterns (realized gain normalized to the mean in azimuth) are presented in Figure 47 and their variance in Figure 48.

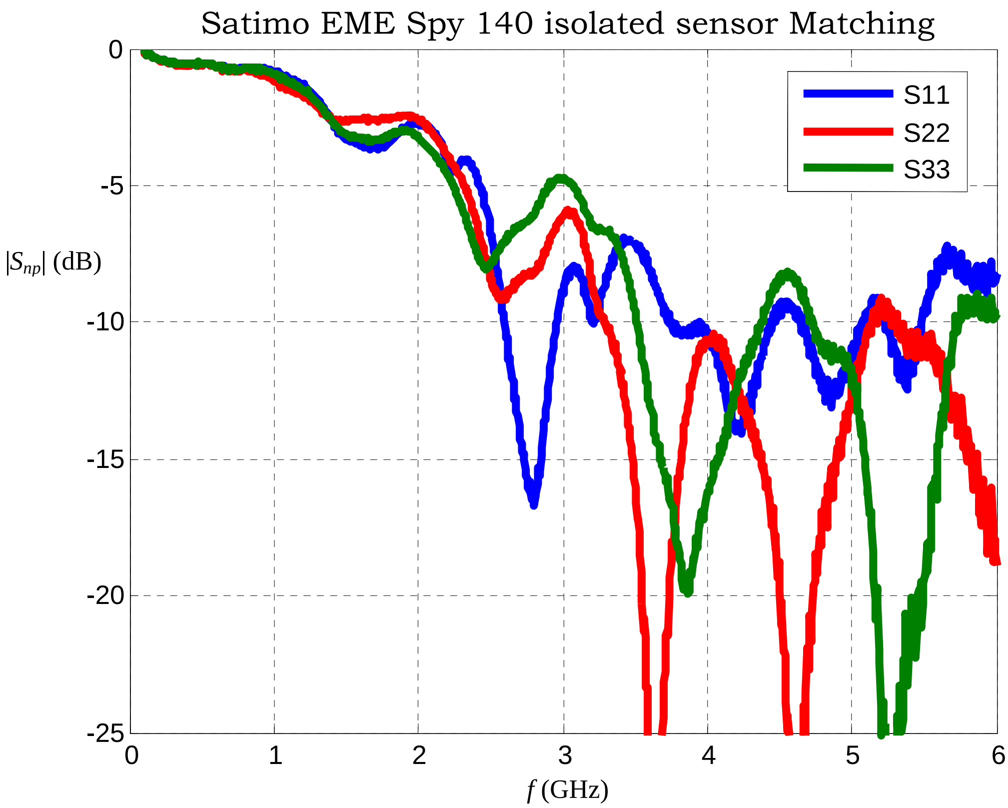

Figure 44 : Reflection coefficient of each probe sensor.

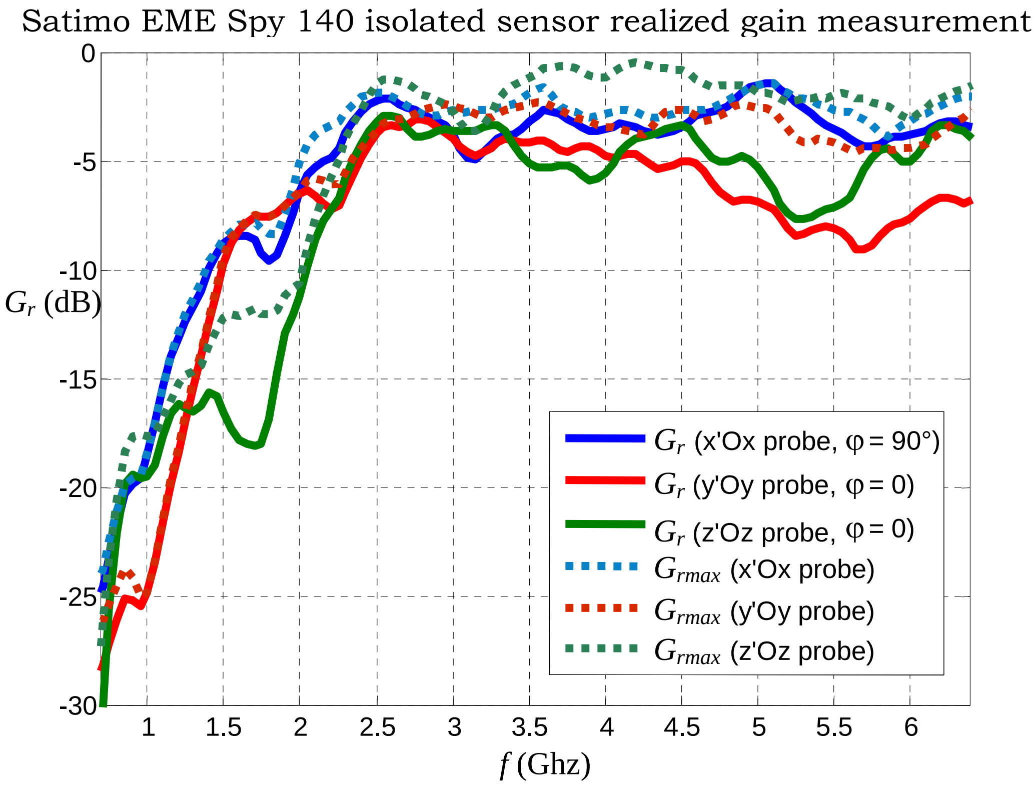

Figure 45 : Realized gains per probe.

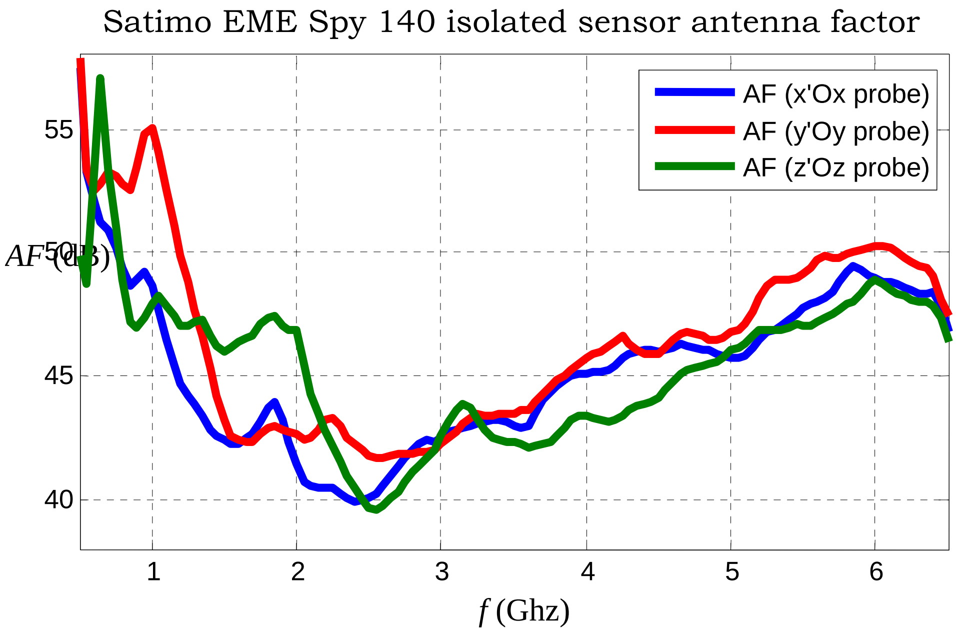

Figure 46 : Antenna Factor per probe.

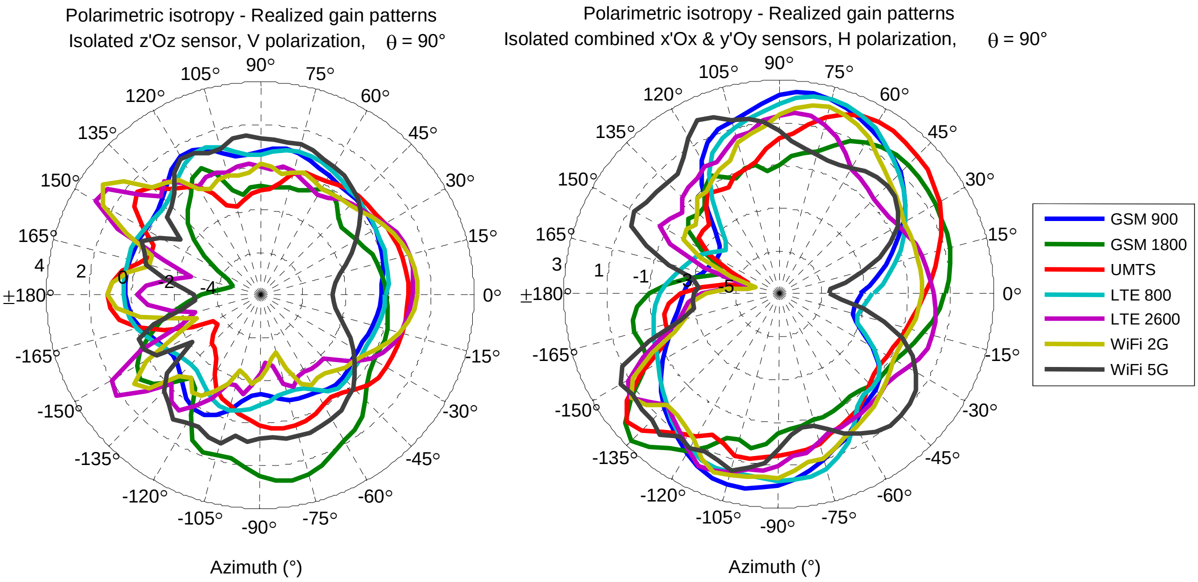

Figure 47 : Normalized realized gain patterns (averaged over each RAT band) of the “V”(z’Oz) probe and combined “H” probes (xOy) in the azimuthal plane, θ = 90°.

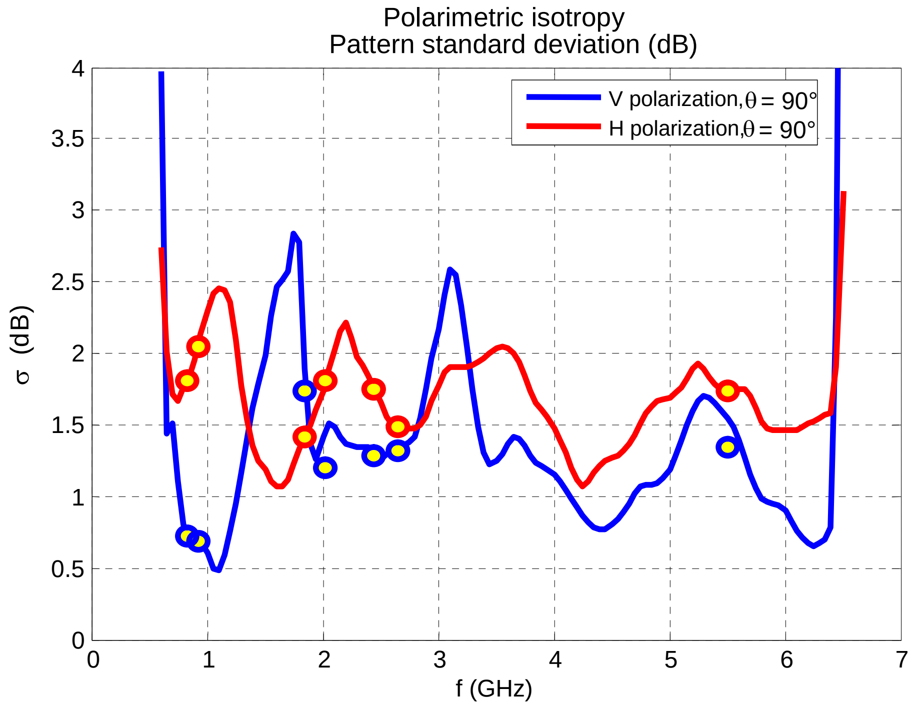

Figure 48 : Realized gain pattern standard deviation over azimuth (averaged over frequency for each RAT – yellow circles) of the “V”(z’Oz) probe and combined “H” probes (xOy), θ = 90°.

In the following tables, μ, σ and m are respectively the mean, the standard deviation and the median.

As can be observed in Figure 47 and in Table 18, the omni-directionality is very satisfactory (typ. σ_G < 2 dB), particularly for the “V” polarization.

Table 20 : Polarimetric isotropy statistics (over azimuth), in dB

	GSM 900	GSM 1800	UMTS	LTE 800	LTE 2600	WiFi 2G	WiFi 5G
μ_{Gv}	–0.05	–0.32	–0.15	–0.06	–0.20	–0.18	–0.19
σ_{Gv}	**0.68**	**1.7**	**1.2**	**0.72**	**1.3**	**1.3**	**1.35**
m_{Gv}	0.02	–0.26	0.16	0.06	–0.01	–0.20	0.11
μ_{Gh}	–0.45	–0.22	–0.34	–0.36	–0.21	–0.30	–0.30
σ_{Gh}	**2.1**	**1.4**	**1.8**	**1.8**	**1.5**	**1.7**	**1.7**
m_{Gh}	–0.30	–0.29	–0.22	–0.48	–0.09	–0.24	0.18

However, the polarization purity of the probes, although satisfactory for such small wideband sensor, is not very high, in particular for the "H" probes at low frequencies as can be observed in Figure 49 and Table 19 (the cross-polarization ratio (XPR) is defined as $XPR = G_r^{cx} / G_r^{co}$). For most of the cases, it is typically less than –10 dB for the vertical probe and less than –4 dB for the higher bands (LTE & WiFi) for the horizontal probes. However the XPR is high for the lower bands of the later. The *XPR* is even positive at low frequencies (up to +3 dB for the GSM900 and LTE800) in some directions. One of the first conclusions is hence that the polarization aspect should be considered cautiously for the calibration and next for the correction procedures in the wearable case.

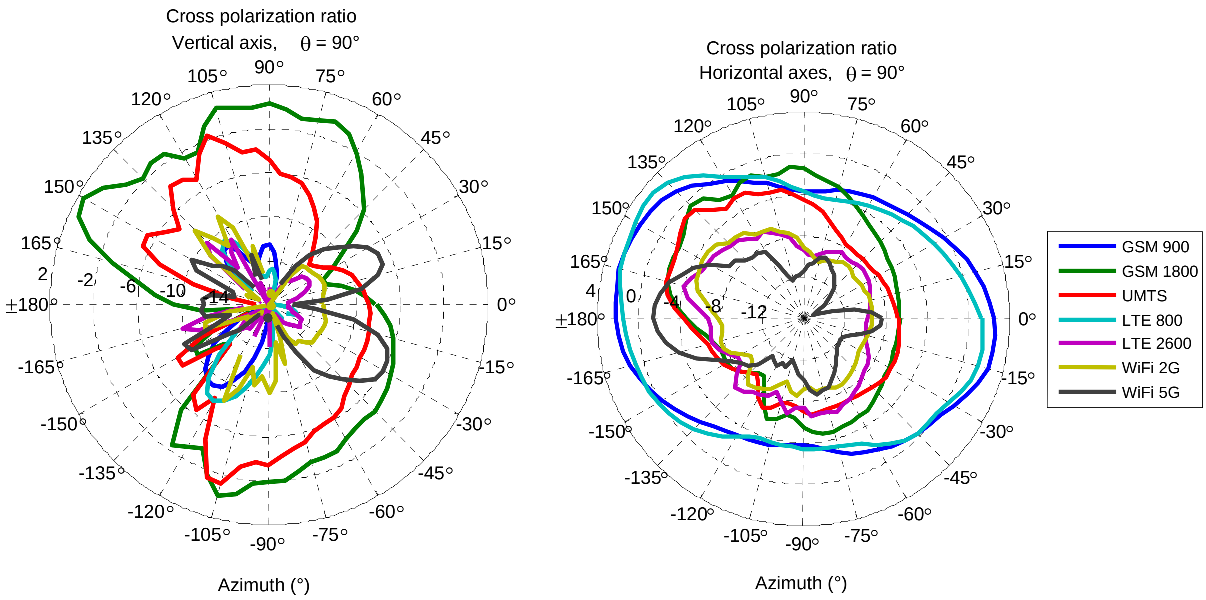

Figure 49 : XPR levels (averaged for each RAT) of the isolated "V"(z'Oz) probe and combined "H" probes (xOy) in the azimuthal plane, θ = 90°.

Table 21 : Polarimetric sensor XPR statistics (over azimuth), in dB.

XPR	GSM 900	GSM 1800	UMTS	LTE 800	LTE 2600	WiFi 2G	WiFi 5G
μ_{XPRV}	**–17.99**	**–5.10**	**–8.30**	**–17.86**	**–16.75**	**–14.42**	**–14.47**
σ_{XPRV}	5.20	4.69	4.53	5.49	3.71	3.44	5.35
μ_{XPRh}	**–0.57**	**–4.99**	**–5.89**	**–0.83**	**–7.75**	**–8.41**	**–9.33**
σ_{XPRh}	2.20	2.26	2.07	2.18	1.44	1.50	3.19

4.2.1.2 Non polarimetric approach

❑ *INFLUENCE OF THE INCIDENT FIELD POLARIZATION*

As the polarization of the incoming wave is a priori not known on the one hand, and, in the other hand, as the sensor XPR is not always low as shown in the previous section, a non polarimetric approach is presented hereafter. The influence of the incoming wave XPR is first considered. For simplicity, the analysis is restricted to linear polarization. To this end, the sensor is analysed in the receiving mode instead of in the transmitting mode as previously.

The XPR of the incident plane wave $\mathbf{E}_{i0} = E_{i0}^V \hat{\boldsymbol{\theta}} + E_{i0}^H \hat{\boldsymbol{\varphi}}$ is defined as $xpr = \left|E_{i0}^H\right|^2 / \left|E_{i0}^V\right|^2$ and the field strength is set to 1 V/m, so that:

$$E_{i0}^V = \pm \frac{1}{(1+xpr)^{1/2}} \tag{3.11.5}$$

$$E_{i0}^H = \pm \frac{xpr^{1/2}}{(1+xpr)^{1/2}} \tag{3.11.6}$$

expressed in V/m.

Note that, besides the field component amplitude, the signs (i.e. the phase) of these components is important, as the field can be in any quadrant of any plane tangent to the sphere, and as the probes are not purely polarized, so that each projection must be added at the field level and not in power.

The XPR is expressed in dB in the sequel, i.e.: $XPR = 20\,\log(xpr)$. Note that for this definition, the incoming field is horizontally polarized for large *positive* values of the XPR whereas it is vertically polarized for large *negative* values.

The received signal $\bar{b}$ is computed as a normalized combination of the signals received at each probe port, i.e.:

$$\bar{b} = \left(\bar{b}_v^2 + \bar{b}_h^2\right)^{1/2} \tag{3.11.7}$$

with

$$\bar{b}_v^2(f_{RAT},\varphi,xpr)=\frac{\int_{\Delta f_{RAT}}\left|\mathcal{H}_z\cdot\mathbf{E}_{i0}\right|^2 df}{\int_{\Delta f_{RAT}}<\left|\mathcal{H}_z^{\theta}\right|^2>_{\varphi}\,df}$$

$$\bar{b}_h^2(f_{RAT},\varphi,xpr)=\frac{\int_{\Delta f_{RAT}}\left|\mathcal{H}_x\cdot\mathbf{E}_{i0}\right|^2+\left|\mathcal{H}_y\cdot\mathbf{E}_{i0}\right|^2 df}{\int_{\Delta f_{RAT}}<\left|\mathcal{H}_x^{\varphi}\right|^2+\left|\mathcal{H}_y^{\varphi}\right|^2>_{\varphi}\,df} \quad (3.11.8)$$

where x, y (resp. z) refer to the “H” probes (resp. “V” probe), $<\cdot>_\varphi$ denotes an averaging over variable φ, and the superscript “*T*” has been omitted in the ATF notation to ease the readability (actually any of the Tx or Rx ATF can be used in these expressions).

It is easy to show that $\bar{b}=1$ for an “ideal” sensor, i.e. perfectly matched, lossless and fully isotropic.

The following figures show the influence of the incoming wave XPR on the received signal $\bar{b}$ for several RATs (some have been omitted because their behaviour is very similar to the presented ones, as the bands are very close, e.g. LTE 800 and GSM 900).

As can be observed in Figure 50, the deviation from isotropy depends on the field XPR and on the frequency bands. However, as compared to Figure 49 or Table 21, the deviation is lower (for the “V” polarization) or comparable. The main difference here is that the field polarization is not known a priori.

This shows actually, that we can take advantage of the polarimetric capabilities of the sensor to improve its isotropy using it as a non polarimetric probe. The improvement is rather low here, but as it depends on the probe isotropy and polarization purity on the one hand, and on the polarization and directional characteristics of the field (i.e. in practice on the channel characteristics, notably its depolarization effects) on the other hand, it is expected that the result will be more significant when the sensor will be placed near the body, because its presence induces a significant depolarization effect on both the incoming field and probe radiation characteristics.

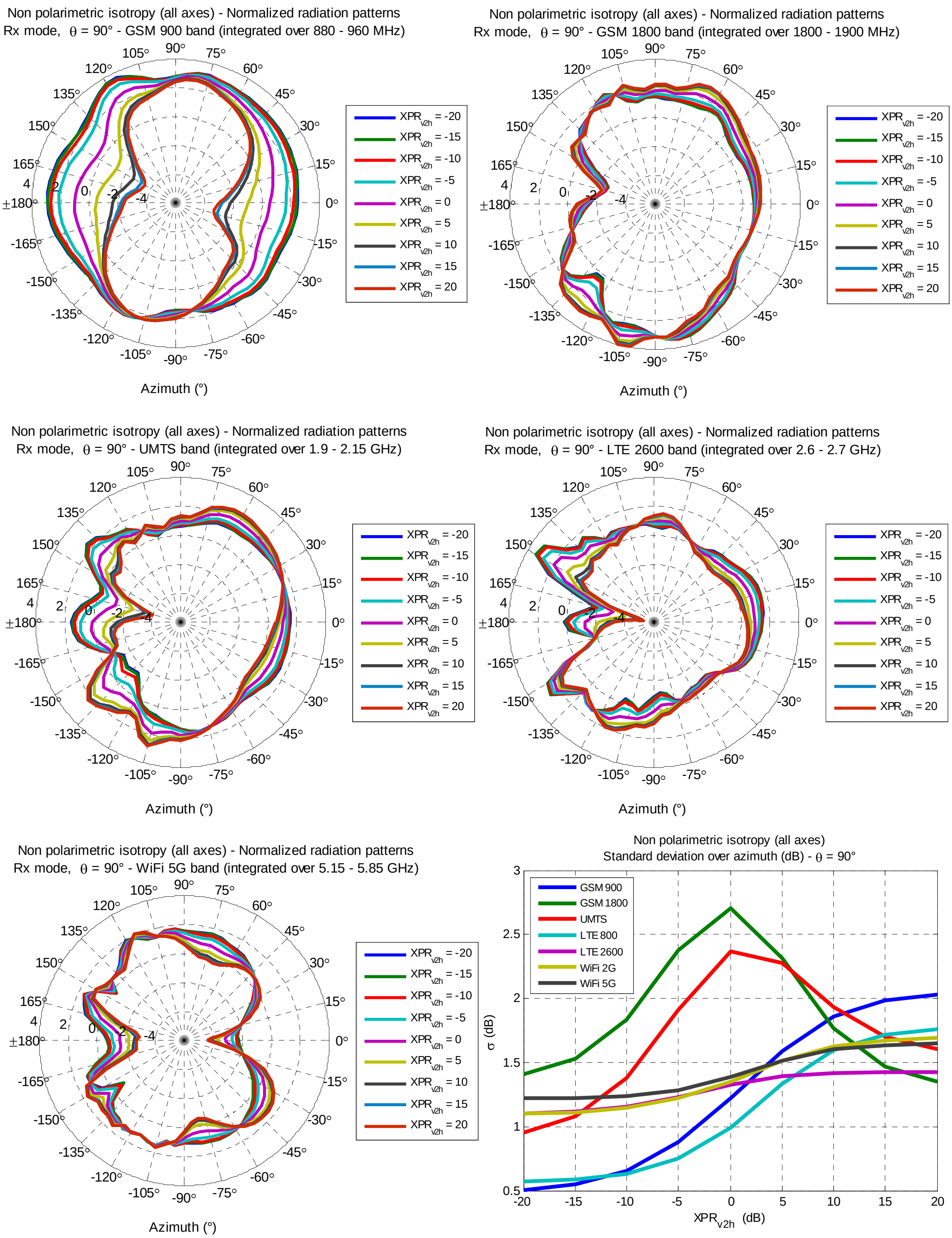

Figure 50 : Influence of the incoming wave XPR level on the isotropy (for various RATs), (a-e) received signal "patterns" in azimuth, (f) variance of the isotropy (θ = 90°).

- *INFLUENCE OF THE CHANNEL CHARACTERISTICS*

In order to extend the preceding analysis to take into account the channel characteristics, in particular its amplitude behaviour, angular spread and depolarization effect, a simplified version of the WINNER II / WINNER+ statistical channel model [19], [20], [21] for various scenarios is now introduced to assess the sensor performance.

The sensor probes are again considered in the Rx mode and the statistics of the received signal are analysed within this framework.

- *Channel model*

The received signal $\bar{b}$ is computed in the same way as before, but the field obeys now to the statistical laws of the channel model. The total field level is still fixed to $Ei_0 = 1$ V/m, but its energy is angularly spread in several "clusters" considered here for simplification as simple MPCs (Multi Paths Components). More precisely, the "intra-cluster" MPC structure is "aggregated" here in a single path (the intra-cluster statistics, in particular the angular spreads are accounted for globally). The PL (Path Loss) modelling is irrelevant here as we are dealing with received waves and not radio link budgets. In the same way, the delay domain is not of concern as the signal is integrated at the receiver over durations which are far larger than the delay spread. The carrier phase aspect, and related small scale (or selective) fading is neither considered in order to simplify the approach, and also, more fundamentally, because in practice measurements are averaged over time and/or space. In the same way, the departure angular spectrum – related to the BS or AP antennas Tx characteristics – is not directly considered here. It is supposed that their effect (sectorised or omni, etc.) is included in the channel angular spread properties. The environment type ("scenarios" in WINNER models such as Indoor, Outdoor to Indoor (O2I), Urban Macrocells (UMa), in LOS or NLOS, etc.), the number of clusters ("multipaths"), the angular spectrum (Angle of Arrival, AoA) and polarization statistics (XPR) are however taken into account. In this part, only the azimuth spread is considered as the measurements were only performed over the azimuthal plane ($\theta = 90°$).

In the simplified model which will be used, the number of paths, angular spectrum and XPR do not depend explicitly on the frequency, although they depend on the environment which is, for some, related to the RATs frequency bands (i.e. WLANs are mainly used in indoor environments and over WiFi bands). In other words any explicit frequency dependence of these parameters is neglected here. The channel model is briefly summarized below, and a detailed description is presented in appendix 4.

The model includes the statistics of: the number of paths N (normally distributed), the angle of arrival (AoA) and angular spread (AS) for both azimuth and elevation, the amplitude (Rayleigh or Rice distributed) and its dependence to the AS, and the XPR (lognormally distributed).

A summary of the characteristics of the four considered environments and their rough correspondence with WINNER scenarios is shown in Table 22 : Radio channel parameters for the considered environments..

Table 22 : Radio channel parameters for the considered environments.

Env. n°	Local environment	WINNER scenario	K factor Mean/Std (dB)	XPR Mean/Std (dB)	Azimuth Spread Mean/Std (°)	Nb clusters Mean/Std
1	Office/room indoor	A2, B4, C4		NLOS: 3.5/9.5	NLOS: 23/16	NLOS: 10.6/2.4
2	Urban (in street), LOS from BS	B1, C1	8.9/6.7	LOS: 12/4.5	LOS: 26/12	LOS: 6/3.5
3	Urban (in street), NLOS from BS	B1, C1-C3		NLOS: 7.5/3	NLOS: 34/17	NLOS: 14/3
4	Indoor small office / residential, LOS from AP	A1	8/3	LOS: 11.5/3.5	LOS: 44/9	LOS: 12/6

A typical example of 3D channel power, XPR and AoA spread in NLOS UMa scenario (Env. n° 3) is shown in Figure 51.

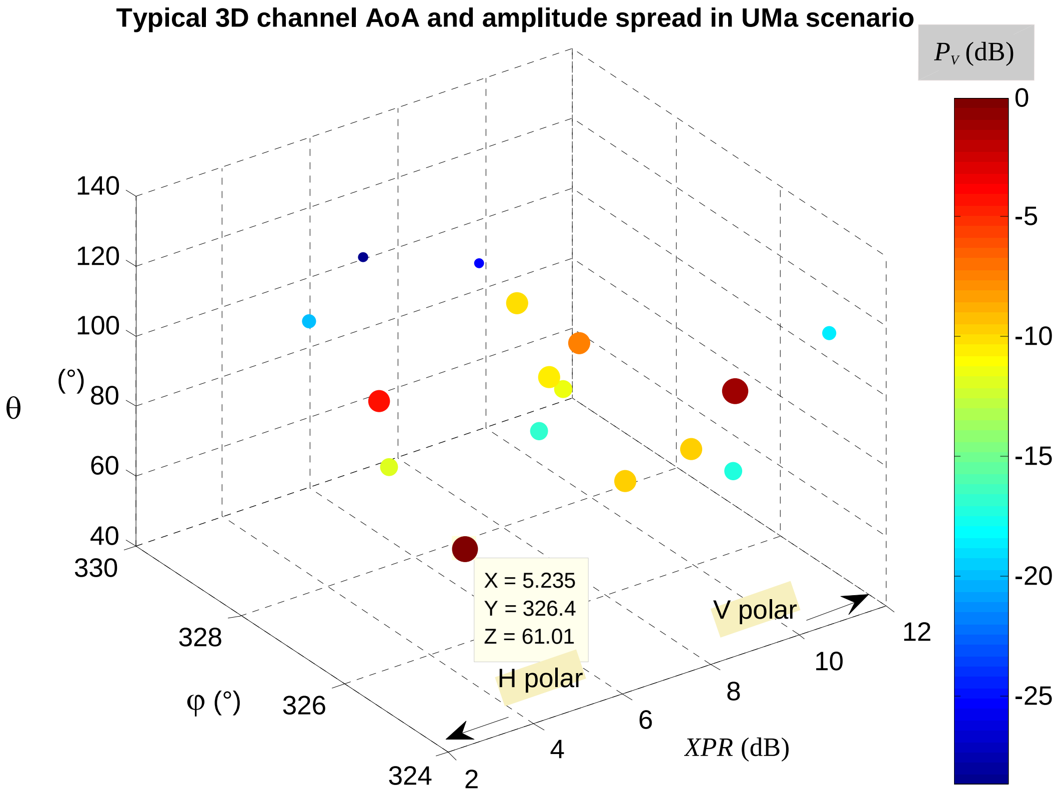

Figure 51 : Typical WINNER+ based 3D channel example.

➢ *Statistical results*

The statistics of the isotropy deviation based on 5000 channel statistical samples for each environment are shown below.

The field is represented in linear scale in Figure 52 (to assess the field variance) and in dB in Figure 53 to be able to fairly compare the variance with the results of the previous sections.

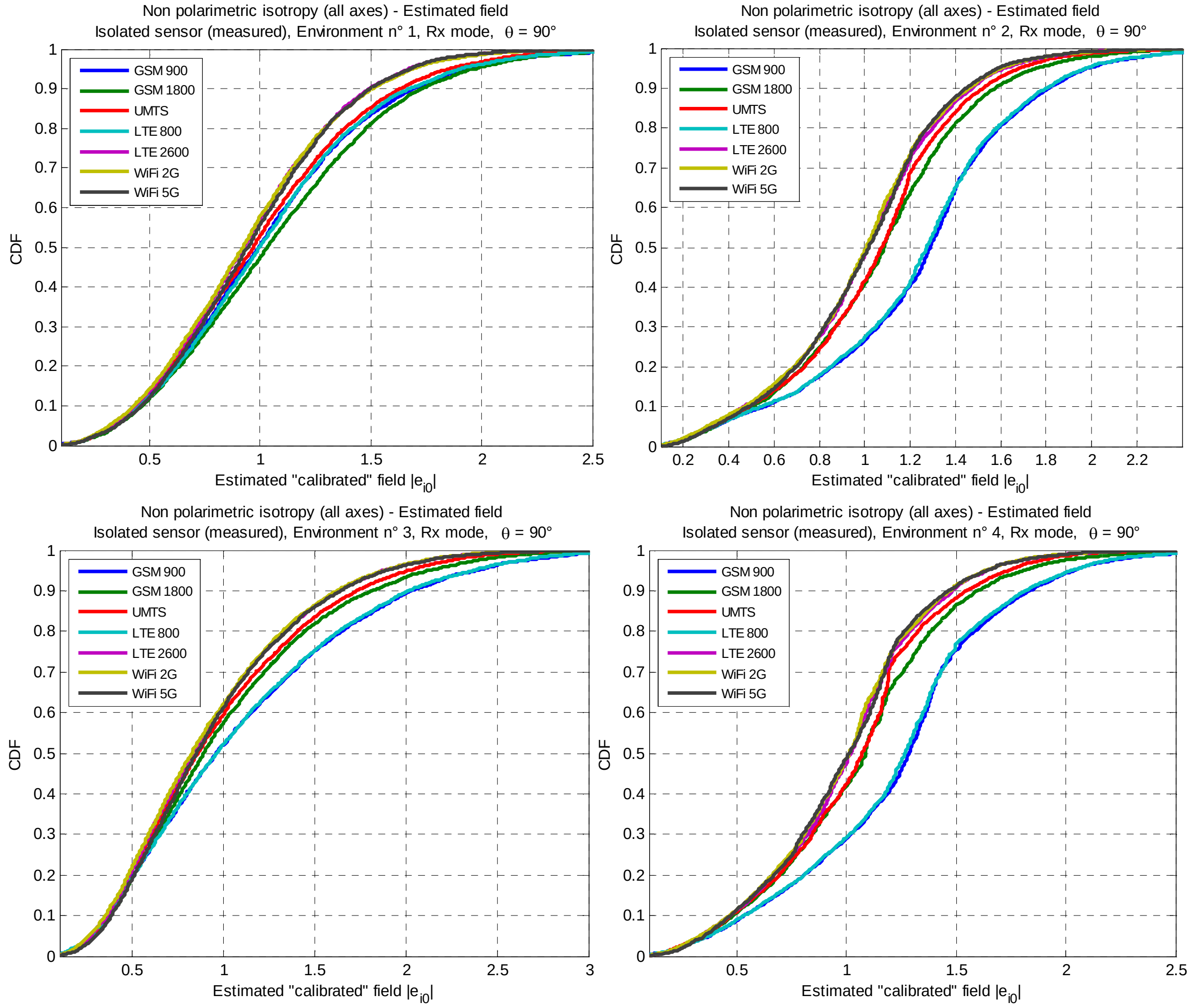

Figure 52 : Non polarimetric statistics (CDF) of isotropy deviation for 4 typical WINNER+ based 3D channel environments. The field strength ei0 is normalized to 1 V/m.

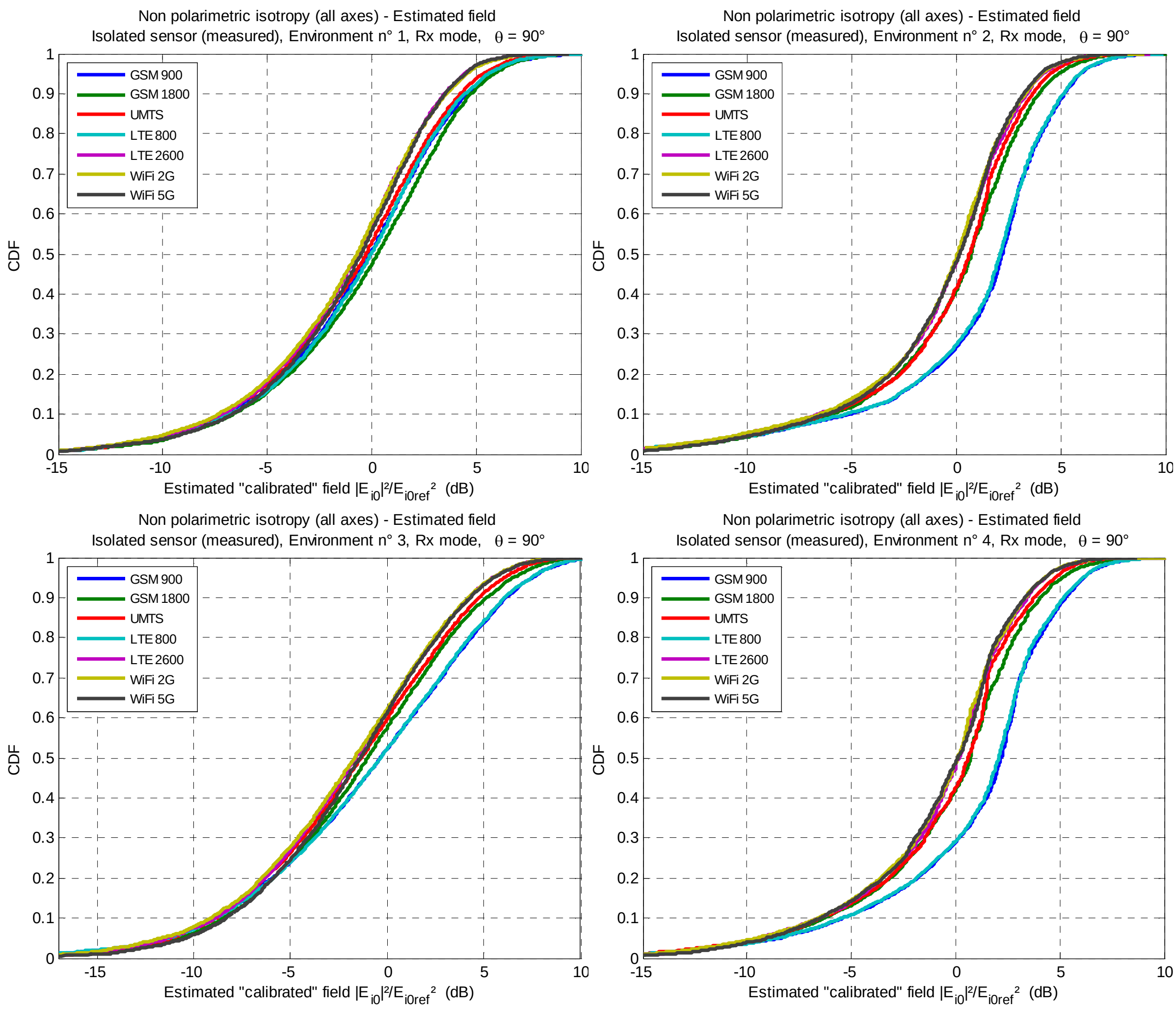

Figure 53 : Non polarimetric statistics (CDF) of isotropy deviation for 4 typical WINNER+ based 3D channel environments. Normalized field expressed in dB.

Table 23 : Non polarimetric sensor isotropy deviation statistics (over azimuth) for Env. n° 1.

e_{i0norm}	GSM 900	GSM 1800	UMTS	LTE 800	LTE 2600	WiFi 2G	WiFi 5G
μ_{ei0} †	**1.03**	**1.08**	**1.0**	**1.04**	**0.95**	**0.95**	**0.97**
σ_{ei0} †	0.48	0.50	0.46	0.47	0.40	0.41	0.40
m_{Ei0} (dB)	–0.15	0.27	–0.34	–0.06	–0.64	–0.76	–0.45
σ_{Ei0} (dB)	**4.66**	**4.67**	**4.61**	**4.58**	**4.32**	**4.41**	**4.19**

† In linear scale. These quantities, "normalized" to a total incident field of 1 V/m, can hence be considered either in relative scale or in V/m.

Table 24 : Non polarimetric sensor isotropy deviation statistics (over azimuth) for Env. n° 2.

e_{i0norm}	GSM 900	GSM 1800	UMTS	LTE 800	LTE 2600	WiFi 2G	WiFi 5G
μ_{ei0}	**1.24**	**1.07**	**1.04**	**1.23**	**1.0**	**0.99**	**1.0**
σ_{ei0}	0.46	0.41	0.38	0.46	0.37	0.37	0.36
m_{Ei0} (dB)	**2.19**	0.70	0.60	**2.08**	0.11	0.01	0.12
σ_{Ei0} (dB)	**4.36**	**4.11**	**4.03**	**4.34**	**4.04**	**4.07**	**3.83**

Table 25 : Non polarimetric sensor isotropy deviation statistics (over azimuth) for Env. n° 3.

e_{i0norm}	GSM 900	GSM 1800	UMTS	LTE 800	LTE 2600	WiFi 2G	WiFi 5G
μ_{ei0}	**1.10**	**1.0**	**0.96**	**1.09**	**0.92**	**0.92**	**0.94**
σ_{ei0}	0.66	0.57	0.54	0.65	0.50	0.50	0.50
m_{Ei0} (dB)	**–0.37**	**–1.02**	**–1.34**	**–0.33**	**–1.61**	**–1.66**	**–1.40**
σ_{Ei0} (dB)	**5.92**	**5.35**	**5.33**	**5.89**	**5.22**	**5.28**	**4.95**

As can be observed in Figure 52 or Figure 53 and Table 23 to Table 25, there is almost no bias in the field assessment for all the LOS scenarios (Environments n° 2 and 4) and almost all NLOS scenarios (Environments n°1 and 3): means are very close to 1 V/m, although the medians are clearly shifted for the environment n° 3 as the distribution is far from normality. Only 4 cases, for low frequency RATs (GSM 900 and LTE 800) in LOS situations (Env. n° 2 & 4), present such a bias of about 25 % (linear scale) or about 2 dB.

On the other hand, in all cases, the variance is significantly higher than previously (see Figure 48, Figure 50 and Table 18), ranging between 4 and 6 dB (instead of 0.7 – 2.7 dB). It is of course due to the fact that the channel characteristics were not previously taken into account: in particular, there is an interaction between the probes XPR and the channel depolarization effect, and above all, the signal received by each probe is a linear combination of signals proportional to the field of each MPC which consequently involves not only the directional amplitude variation of their transfer functions, but also their phase variation. This is probably why the variance is larger for the 3rd environment: its angular spread and number of MPCs is larger, on average, than the first two.

Note that if the same computations are performed with a hypothetic channel characterized by a small number N of MPCs and a small angular spread, we find back results similar to the previous ones.

A partial conclusion here is that the real dispersion of the sensor measurement, i.e. in real environments, is higher than expected if the sensor accuracy is characterized regardless of the channel.

Some of the obtained statistics have been analysed in order to bring out some theoretical distribution fits. It appears that the Nakagami distribution is suitable for NLOS environments, whereas LOS ones are well fitted by truncated double exponential distributions ("asymmetric Laplace" distribution). All cases are significantly far-off normality. In LOS, the Ricean or gamma distributions are other possibilities, better than Gaussian, but worth than Nakagami. In NLOS, none of the previous distributions are suitable, only a truncated Laplacian type is satisfactory, the pure Laplace distribution being clearly less accurate than the double exponential. In complement to the CDF, probability plots are also shown in Figure 54, as the "goodness of fit" is better underlined.

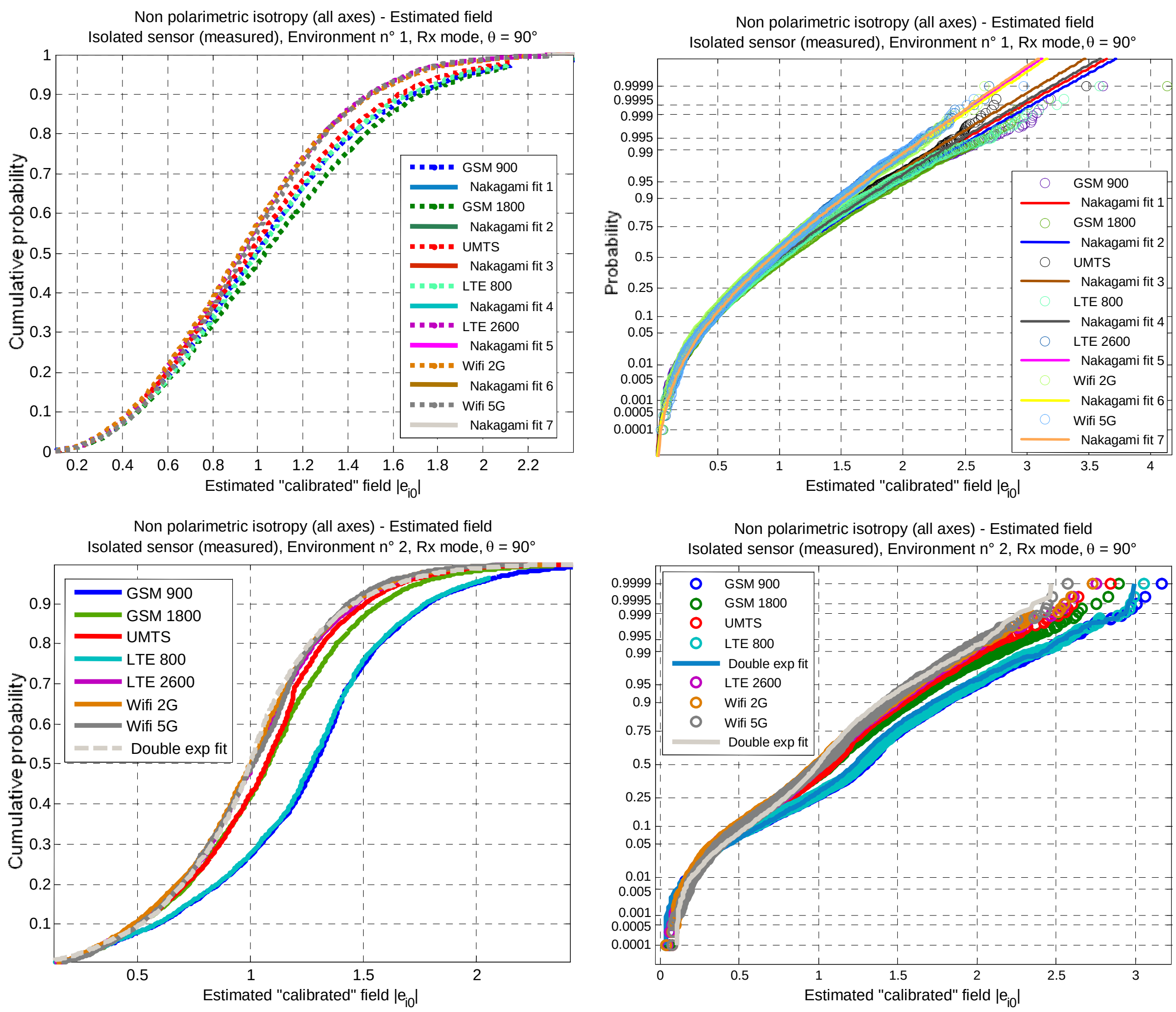

Figure 54 : Non polarimetric statistics (CDF) of isotropy deviation and examples of statistical fits for an NLOS and a LOS environments.

4.2.2 Sensor on whole body phantom

Measurements were carried out with a whole body phantom in an anechoic chamber, at IMT's premises, over an ultra wide band (0.5 – 6.5 GHz). An EME Spy 140® dosimeter comprising a three-axial sensor was used to probe the far field, bypassing its internal electronics with coaxial cables directly connected to each of the three probes. Three positions on the phantom were considered: on the "left chest", on the "left hip" and at the level of the right back pocket of trousers. This positioning was chosen based on a criterion of realistic practical use, e.g. in the internal pocket of a jacket or in a pocket of a shirt for the first, and in a front pocket of trousers or attached to the belt for the second. For each location, three distances to the body were considered (about 0, 10 and 20 mm) in order to extend the practical relevance and test the spacing influence. For each configuration and axis, the antenna transfer function $\mathcal{H}(f,\theta,\varphi)$, was measured over the azimuthal plane for three elevations (0, 20° and –16°) and two orthogonal polarizations (vertical, parallel to the rotation axis in azimuth, i.e. to the phantom, and horizontal). The reflection coefficients S_{11} were also measured for each configuration. This constitutes a total measurement set of 11 691 frequency responses (comprising 162 conical cuts (3 probes x 3 sensor positions x 3 elevations x 2 polarizations) and 27 S_{11}). All relevant quantities, either in emission (realized gain G_r, power gain G) or in reception (e.g. (loaded) antenna factor AF), can be computed from the measured quantities, for each polarization. Any signal received at each probe port can be computed as well for a given incident power density or field strength.

4.2.2.1 Phantom characteristics

The whole body phantom used is 1.69 m tall (Figure 56). Its dielectric properties have been determined by T. Alves (University of Paris-Est Marne-la-Vallée) with an original experimental method [17]. They are illustrated in Figure 55. For comparison, the relative permittivity of the skin, fat and muscles (mainly based on Gabriel & Grabriel's work and provided by ITIS' Foundation [18]) are also shown in the Figure 55. The homogeneous phantom properties appear, at least for the $\varepsilon_r^{'}$, as a weighted average of the skin, fat and possibly muscles ones. The $\varepsilon_r^{''}$ seems however slightly larger than required for the frequencies of interest in the project. Nevertheless, this experimental model is globally really satisfactory.

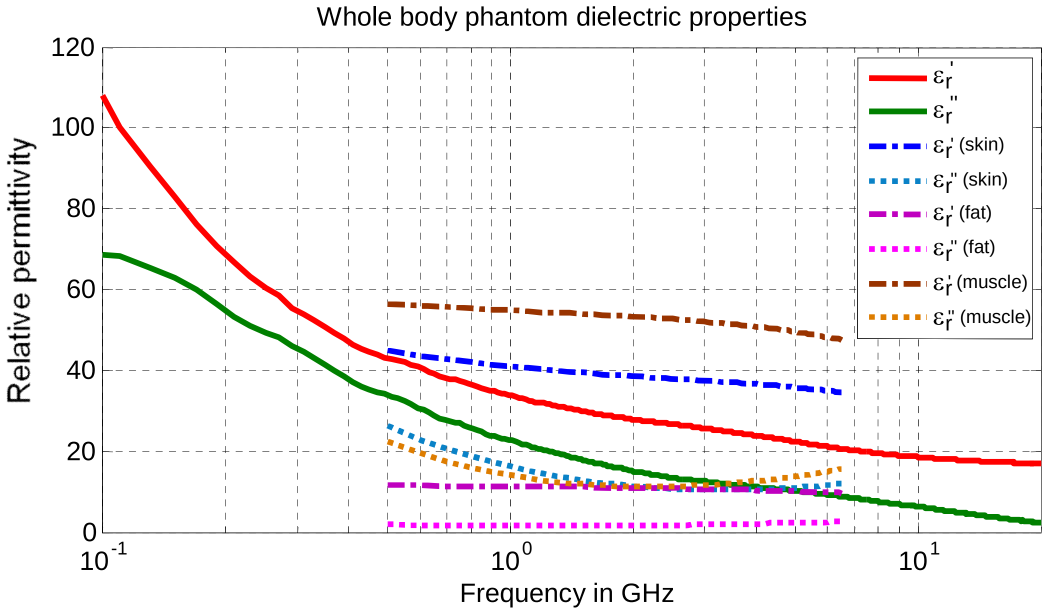

Figure 55 : Whole body phantom ("Kevin") dielectric properties (from [17]).

4.2.2.2 Measurement setup

Measurements are carried out in an anechoic chamber. The phantom is placed at the rotation center of a positioning turntable (Figure 56), and transmission measurements for each of the three probes are performed in azimuth with a VNA (Vector Network Analyser R&S ZVA40), for three elevations (0, 20° and –16° from "horizon", i.e. θ = 90°, 70° and 106°, see Figure 60) and two orthogonal polarizations ("V" and "H").

Three sensor positions on the phantom are considered (Figure 56): on the "left chest" (Figure 59), on the "left hip" (Figure 60) and at the level of the right back pocket of trousers (Figure 60). For each location, three distances to the body, thanks to foam spacers (Figure 58), are considered (about 0, 10 and 20 mm), in order to extend the practical relevance and test the spacing influence.

The measurement frequency band is 0.5 – 6.5 GHz, with a frequency step of δf = 50 MHz.

In the following, the retained approaches are similar to those presented in the previous section (polarimetric and non polarimetric, influence of the incoming field XPR and taking into account the channel). The notations are the same.

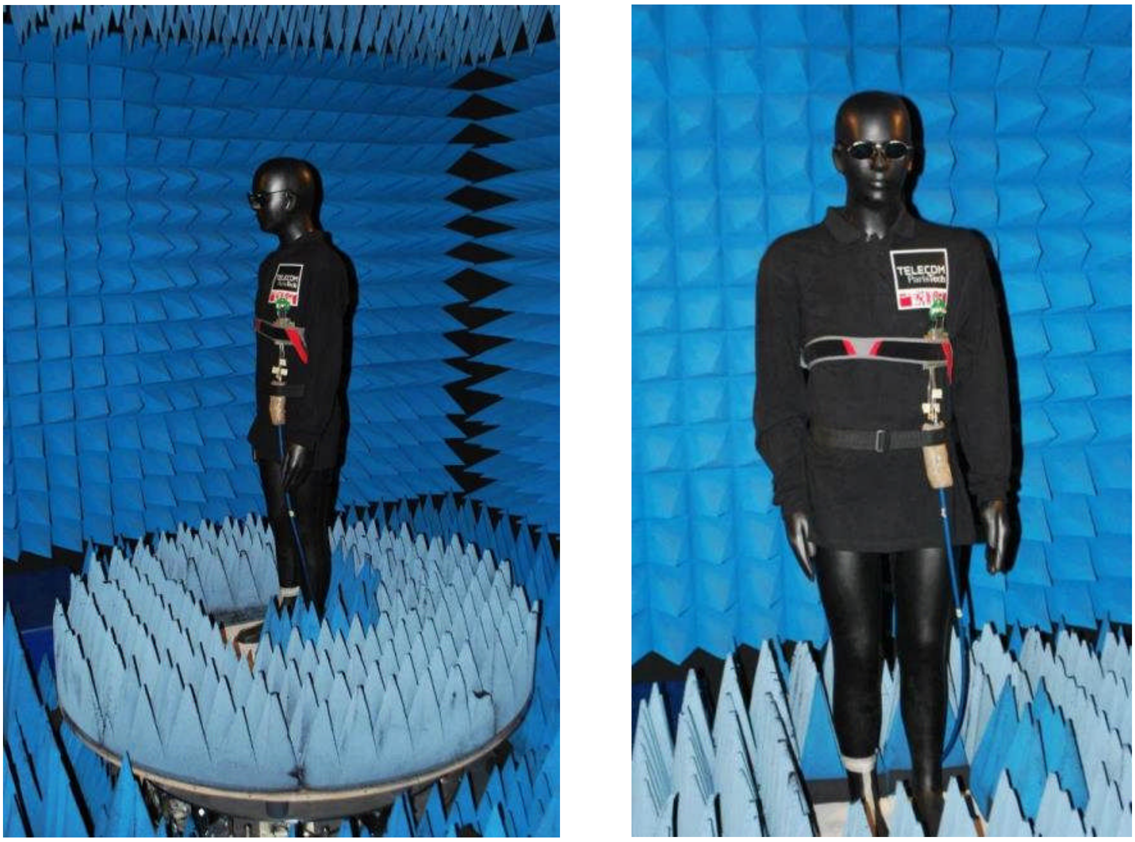

Figure 56 : Phantom positioning in anechoic chamber.

Figure 57 : Sensor positioning on the phantom: left chest, left hip and right back.

Figure 58 : Sensor/phantom spacing: ~ 0, 10 and 20 mm (not shown here).

Figure 59 : Sensor positioning details: left chest,. ~12.5 cm from the saggital plane and ~ 23.5 cm from the top of the shoulder.

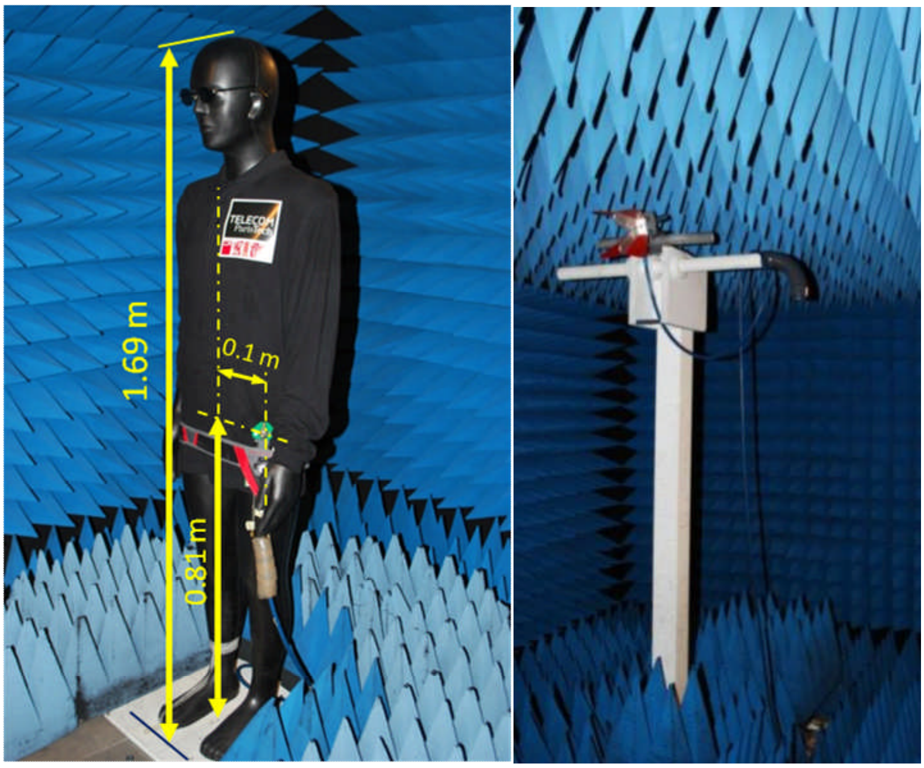

Figure 60 : Left: Sensor positioning details on left hip,. ~10 cm from the saggital plane and ~ 81 cm from the ground; Right: reference antenna positioning for the conical cut at an elevation of 20° above horizon.

Figure 61 : Sensor positioning details: right back,. ~5 cm from the saggital plane and ~ 87 cm from the ground.

4.2.2.3 Measurement results – Elementary approach and global view

The input matching is presented in Figure 62 for the three sensor positions and the smallest spacing (δ ~ 0). As can be observed, the body proximity effect on the $|S_{11}|$ is moderate even for the closest positioning.

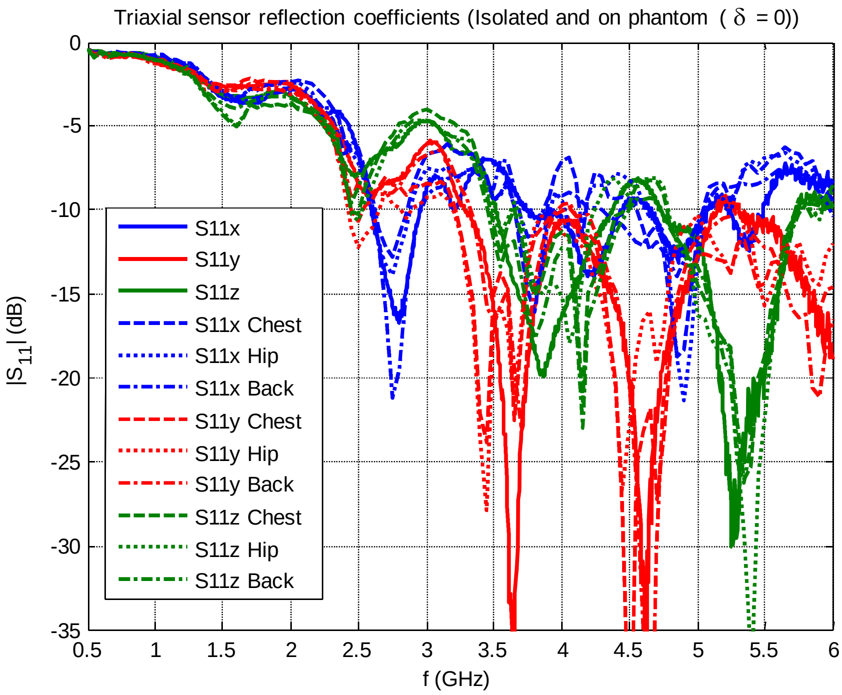

Figure 62 : Reflection coefficient of each probe sensor and for all "scenarios" (compared to the isolated case).

An example of measurements offering a "global view" of the body shadowing effect is given in Figure 63: it shows the total (including all axes) Mean Realized Gain (MRG averaged over 0.7 – 6 GHz) in horizontal polarization, in the azimuthal plane (θ = 90°). As expected, the body masking is the dominant effect, with FTBR of about 13 dB (resp. 15 dB) for the Chest (resp. for the Back). The Hip case is less "unidirectional", but the MRG is globally lower, both aspect being probably due to the effect of the hand. Such high FTBRs induce a high uncertainty of the exposimeter measurements, if it is used as is, without correction strategy. In addition, because of reflections or absorption and shadowing of the body, the exposimeter gain, hence the measured field, can be either higher or significantly lower than in the absence of the carrier.

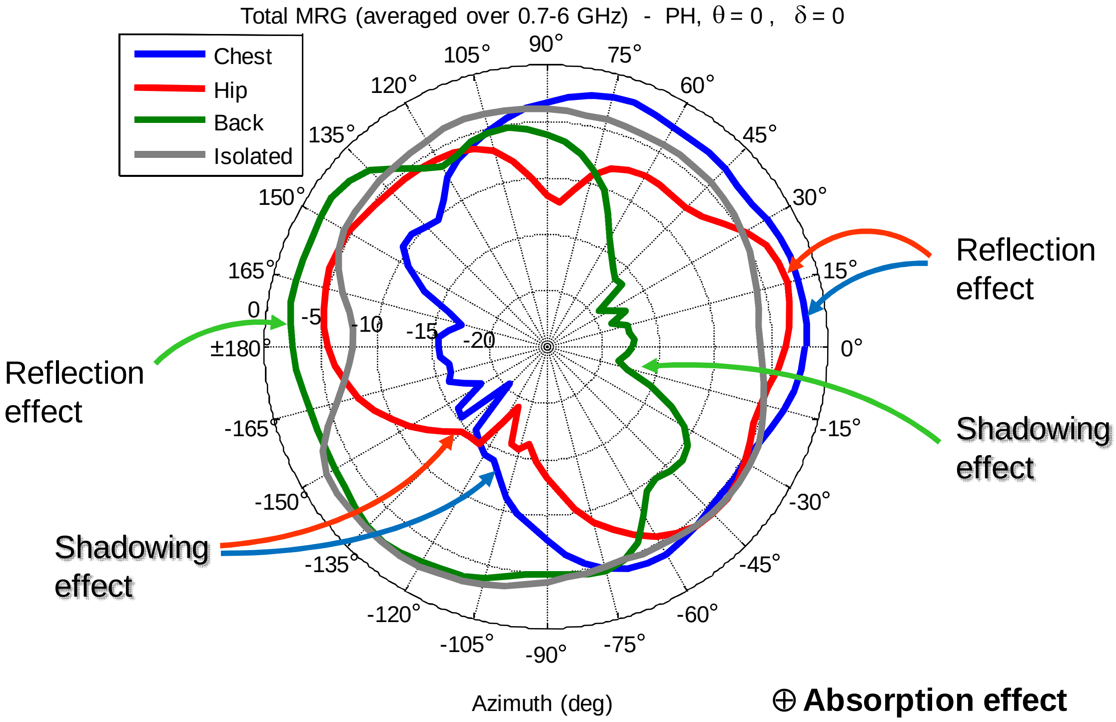

Figure 63 : MRG of each probe sensor and for all "scenarios" (azimuthal cut).

4.2.2.4 Polarimetric approach

- POLARIMETRIC GAIN "ISOTROPY"

As previously, the radiation characteristics (polarimetric realized gain $G_r^{\theta,\varphi} = \left|\mathcal{H}_{\theta,\varphi}^T\right|^2$) are provided hereafter for each considered RAT. The results are as well averaged over each frequency band, but the normalization is now operated relative to the isolated sensor (i.e. its averaged realized gain over azimuth, in the azimuthal plane and for each polarization), instead of normalizing to its own mean, i.e.:

$$\hat{G}_{r,phant}^{\theta,\varphi}(f_{RAT},\theta,\varphi) = \int_{\Delta f_{RAT}} G_{r,phant}^{\theta,\varphi}(f,\theta,\varphi)\,df \Big/ \frac{1}{2\pi}\int_{\Delta f_{RAT}}\int_0^{2\pi} G_{r,isol}^{\theta,\varphi}(f,\pi/2,\varphi)\,d\varphi\,df \qquad (3.11.9)$$

This allows not only to focus on the isotropy variance considering polarization aspects, but also to underline the body effect, compared to the isolated case.

In addition, in practice, the radiation characteristics of the worn sensor won't be exactly known for each carrier user (but only statistically – this is the object of the simulation campaign carried out with various phantom models), whereas the isolated sensor is a priori known with precision.

➢ *"Chest scenario"*

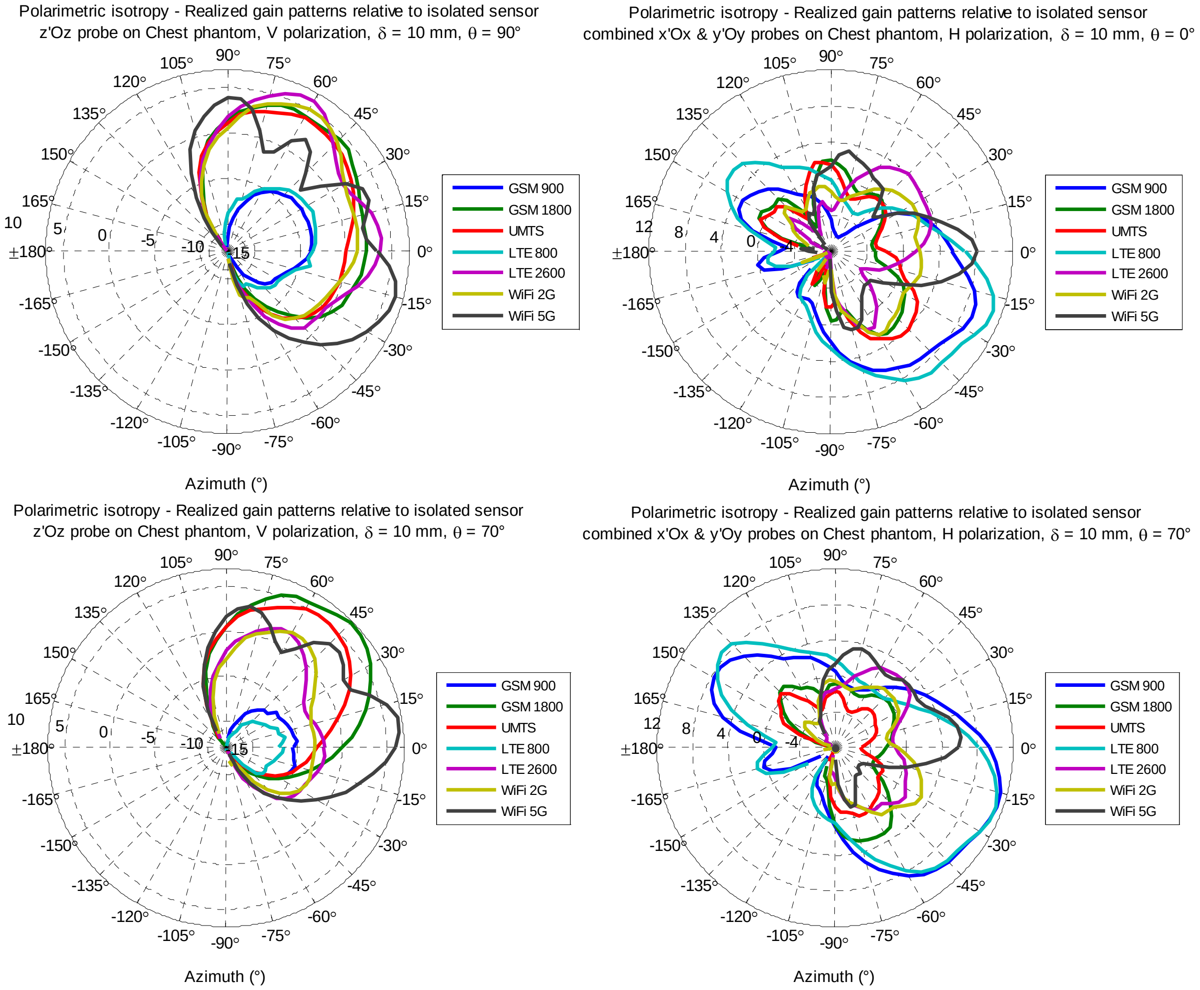

Figure 64 : Normalized (co-polar) realized gain patterns (averaged over each RAT band) of the "V"(z'Oz) probe and combined "H" probes (xOy) in the azimuthal plane for the "Chest scenario", θ = 90° and 70°, φ = 10 mm.

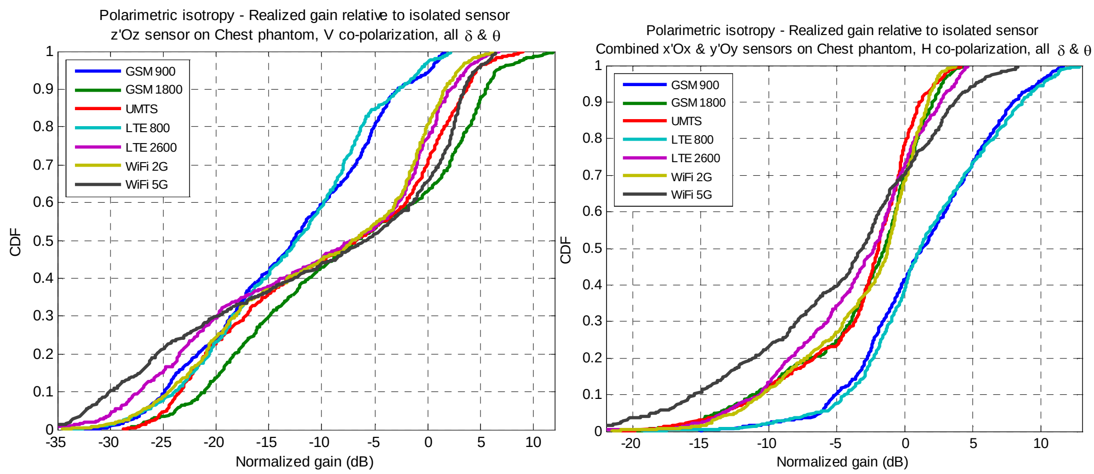

Figure 65 : Normalized (co-polar) realized gain CDF (averaged over each RAT band) of the "V"(z'Oz) probe and combined "H" probes (xOy) in the azimuthal plane for the "Chest scenario", all φ and θ.

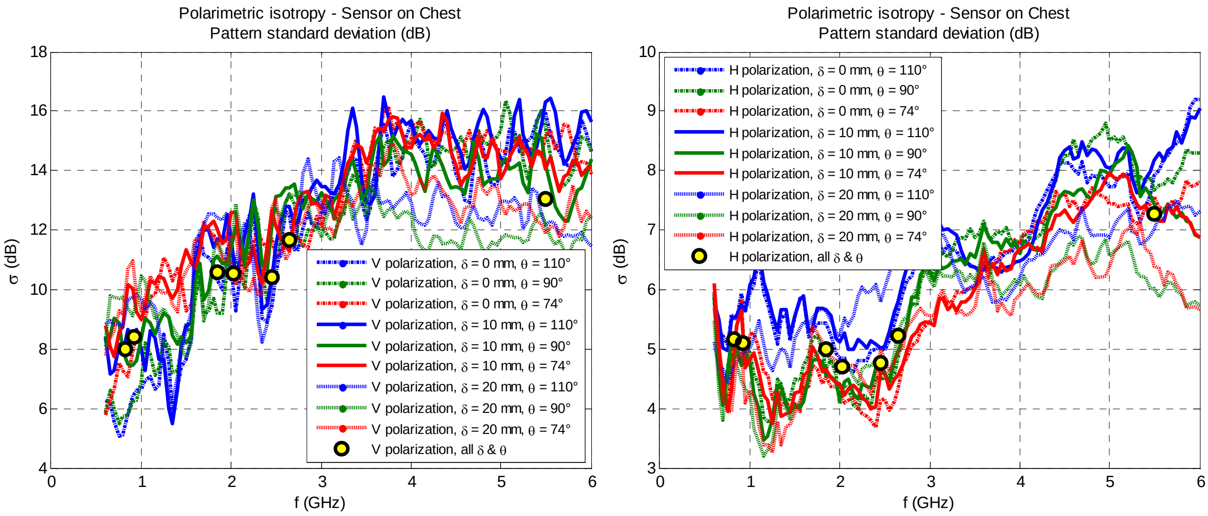

Figure 66 : Normalized (co-polar) realized gain patterns (averaged over each RAT band) of the "V"(z'Oz) probe and combined "H" probes (xOy) in the azimuthal plane for each "scenario", all φ and θ.

The significant reduction of the vertical probe gain at low frequency bands (GSM 900 & LTE 800) *in the visible region* (i.e. in the solid angle for which the sensor is not masked by the body, roughly a semi-space for the vertical probe; see e.g. the top left polar pattern of Figure 64) is probably due to a higher power absorption due to a deeper penetration of the waves in the tissues, related to the polarization which is tangent to the body. EM simulations show that the elevation plays also a non-negligible role.

Apart for the highest band (WiFi 5G), the "isotropy" variance depends only moderately on the elevation and on δ (Table 26).

The results are qualitatively similar for the "Back scenario".

Table 26 : Polarimetric isotropy statistics (over azimuth), Chest, all θ and φ (dB).

	GSM 900	GSM 1800	UMTS	LTE 800	LTE 2600	WiFi 2G	WiFi 5G
μ_{Gv}	–13.13	–7.05	–8.80	–13.14	–10.59	–9.89	–10.21
σ_{Gv}	**8.40**	**10.58**	**10.55**	**7.99**	**11.65**	**10.40**	**13.06**
m_{Gv}	–12.74	–6.64	–6.79	–12.35	–6.92	–7.13	–5.72
μ_{Gh}	1.37	–3.04	–3.29	1.61	–3.56	–3.02	–4.57

σ_{Gh}	**5.10**	**5.00**	**4.71**	**5.16**	**5.22**	**4.76**	**7.27**
m_{Gh}	1.30	–1.50	–1.97	1.12	–2.30	–1.28	–3.10

- *"Hip scenario"*

The situation is significantly different for the "Hip scenario". As can be observed in Figure 67 and Figure 68, the power is spread both towards the front and toward the back for both polarizations. This is partly attributed to the effect of the hand (and arm) which plays somehow a role of reflector. However, on average, the isotropy deviation is similar.

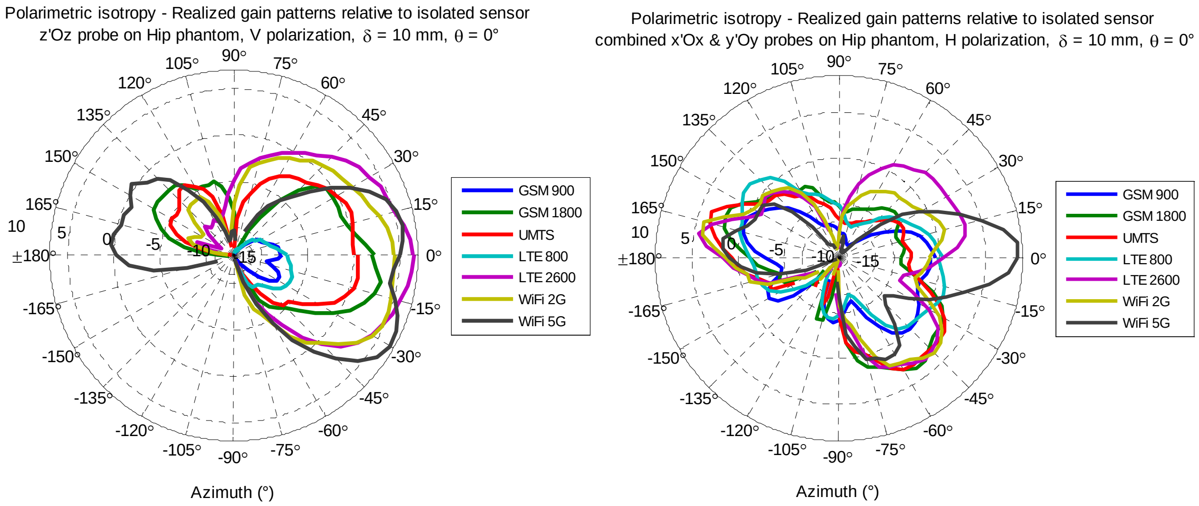

Figure 67 : Normalized (co-polar) realized gain patterns (averaged over each RAT band) of the "V"(z'Oz) probe and combined "H" probes (xOy) in the azimuthal plane for the "Hip scenario", θ = 90°, δ = 10 mm.

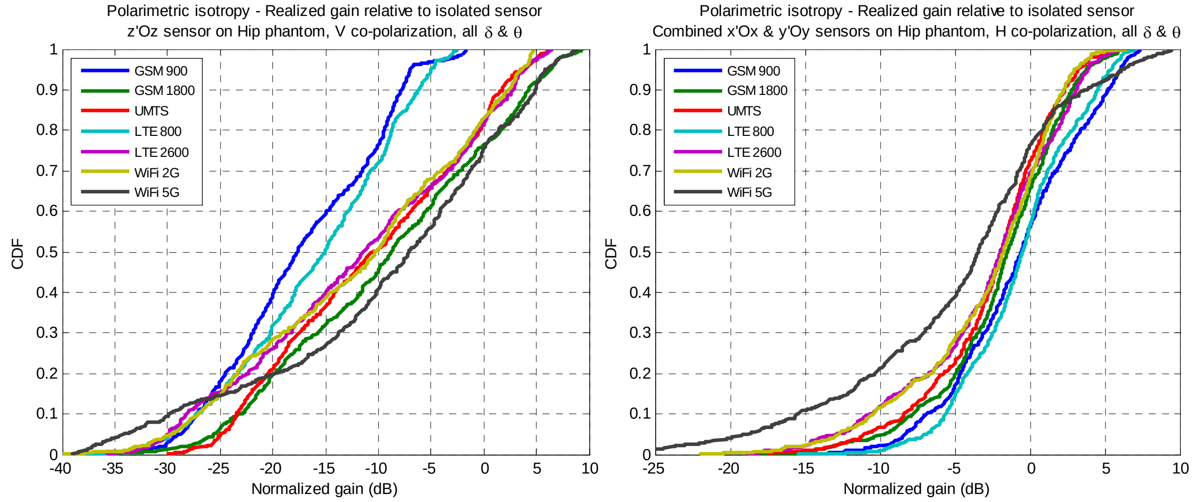

Figure 68 : Normalized (co-polar) realized gain CDF (averaged over each RAT band) of the "V"(z'Oz) probe and combined "H" probes (xOy) in the azimuthal plane for the "Hip scenario", all φ and θ.

Table 27 : Polarimetric isotropy statistics (over azimuth), Hip, all θ and φ (dB).

	GSM 900	GSM 1800	UMTS	LTE 800	LTE 2600	WiFi 2G	WiFi 5G
μ_{Gv}	–17.21	–9.17	–10.55	–15.99	–11.77	–11.85	–9.37
σ_{Gv}	**7.50**	**10.30**	**9.46**	**7.77**	**10.99**	**10.88**	**12.21**
μ_{Gh}	–17.66	–8.73	–10.49	–15.03	–11.34	–10.28	–7.15
σ_{Gh}	**4.40**	**4.18**	**4.19**	**3.81**	**5.11**	**4.91**	**7.30**

- *POLARIMETRIC XPR*

The XPR is still defined as: $XPR = G_r^{cx} / G_r^{co}$. The relative XPR is defined as the ratio of the “on-body XPR” and “isolated XPR”:

$$. XPR_{rel} = \frac{XPR_{ph}}{XPR_{isol}} = \frac{G_{r,ph}^{cx} / G_{r,ph}^{co}}{G_{r,isol}^{cx} / G_{r,isol}^{co}} \quad \text{or} \quad XPR_{rel} = XPR_{ph} - XPR_{isol} \quad \text{in dB.} \qquad (3.11.10)$$

For the sensor on the chest and the vertical probe, the XPR is typically increased, on average, by 2 – 15 dB (compared to the isolated case, Table 21), and up 35 dB for some directions and bands (comparing Figure 69 to Figure 49). This depolarization effect due to the presence of the body is less pronounced for the horizontal sensors. Results are comparable for the hip case. However, these high values occur in the shadow region (masked by the body). In the visible region, the XPR increase is less significant, ranging between –15 dB to 15 dB for the vertical probe (depending on directions and bands) and typically less than 8 dB for the horizontal ones.

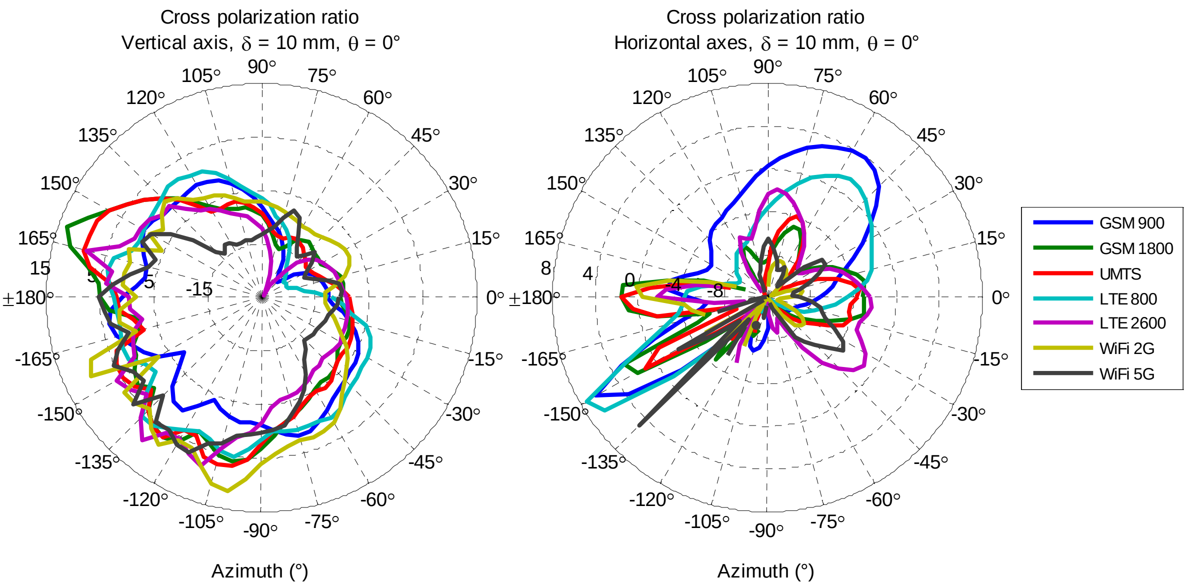

Figure 69 : XPR levels (averaged for each RAT) of the “V”(z’Oz) probe and combined “H” probes (xOy) in the azimuthal plane. Sensor on chest, δ = 10 mm, θ = 90°.

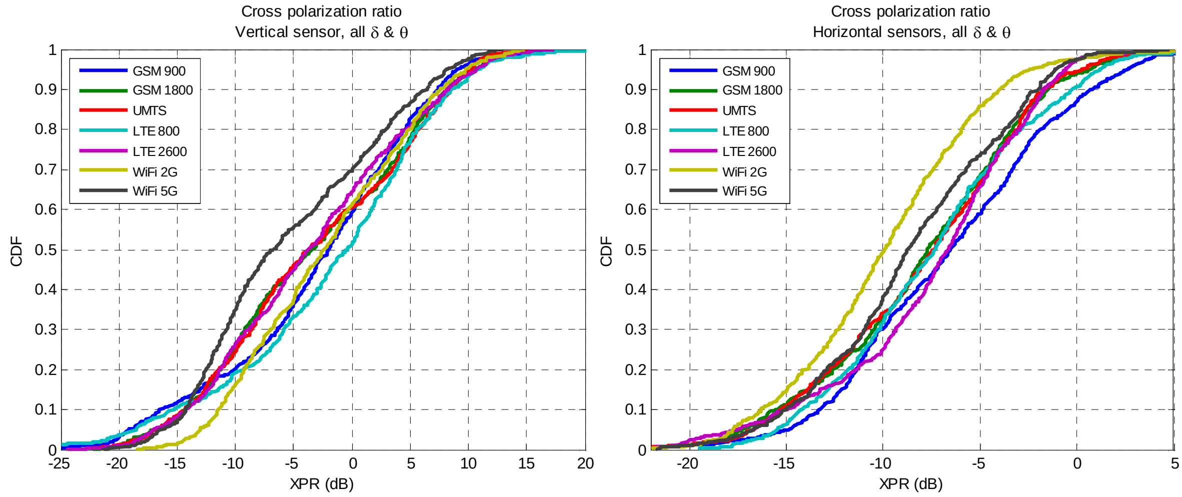

Figure 70 : XPR levels CDF (averaged for each RAT) of the "V"(z'Oz) probe and combined "H" probes (xOy) in the azimuthal plane. Sensor on chest, all θ and φ.

Table 28 : Polarimetric sensor XPR statistics (over azimuth) – Sensor on Chest (all θ and φ).

XPR	GSM 900	GSM 1800	UMTS	LTE 800	LTE 2600	WiFi 2G	WiFi 5G
μ_{XPRV}	**–2.94**	**–3.13**	**–3.07**	**–1.79**	**–3.40**	**–2.11**	**–5.18**
σ_{XPRV}	8.54	8.65	8.65	9.10	8.41	7.22	7.87
μ_{XPRh}	–6.57	–7.90	–7.86	–7.33	–7.44	–9.89	–8.51
σ_{XPRh}	5.56	5.33	5.30	5.11	5.15	4.77	4.89
$\Delta\mu_{XPRV}$	**15.05**	**1.97**	**5.23**	**16.06**	**13.35**	**12.31**	**9.30**
$\Delta\mu_{XPRh}$	–6.0	–2.91	–1.98	–6.50	0.29	–1.49	0.82

Regarding the “Back” scenario, the relative XPR is similar on average, but for the Hip case, the XPR is significantly increased (Figure 71), including in the visible region (around φ = 0, Figure 69).

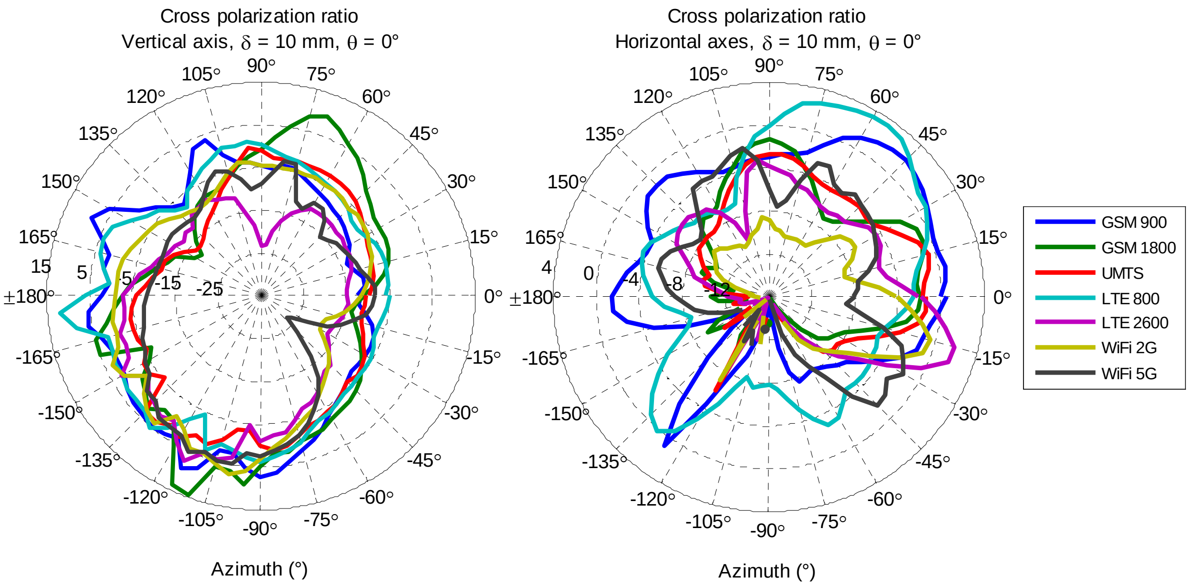

Figure 71 : XPR levels (averaged for each RAT) of the “V”(z’Oz) probe and combined “H” probes (xOy) in the azimuthal plane. Sensor on hip, δ = 10 mm, θ = 90°.

❑ *PARTIAL CONCLUSIONS*

First partial conclusions regarding the worn sensor can be drawn here:

- First, as obviously expected, the isotropy variance is considerably increase compared to the isolated case, by typically 7 to 11 dB for the vertical probe and 2 to 6 dB for the horizontal ones, depending on the band.
- The XPR is clearly modified, significantly increased in many cases, which seriously compromise the perspective of performing reliable polarimetric measurements with the wearable triaxial sensor.
- Hence, resorting to non-polarimetric measurements is more promising.

This last point is considered in the following, based on 3D electromagnetic simulations.

4.3 Simulations

Electromagnetic simulations are based on various numerical phantoms, from simple canonical geometry based models to realistic fully non homogeneous anthropomorphic ones. The last are based on the Virtual Population suit from ITIS’ Foundation (Table 29) [18].

Table 29 : Virtual Population (ITIS’ Foundation) anthropometric characteristics.

Name	Sex	Age [year]	Height [m]	Weight [kg]	BMI† [kg/m²]	Number of Tissues
Duke	male	34	1.77	72.4	23.1	77

Ella	female	26	1.63	58.7	22.0	76
Louis	male	14	1.69	50.4	17.7	77
Billie	female	11	1.47	35.4	16.5	75
Eartha	female	8	1.36	30.7	16.7	75
Dizzy	male	8	1.40	26.0	13.4	66
Thelonious	male	6	1.17	19.3	14.0	76
Roberta	female	5	1.09	17.8	14.9	66

† Body Mass Index

4.3.1 Simplified model of isolated sensor

As a first approach, simulations of a simplified model (provided by Satimo®) of the sensor part of the EME Spy 140® dosimeter first isolated (Figure 72), then “worn” by a numerical phantom of the Virtual Population suit (from ITI’S foundation) are carried on.

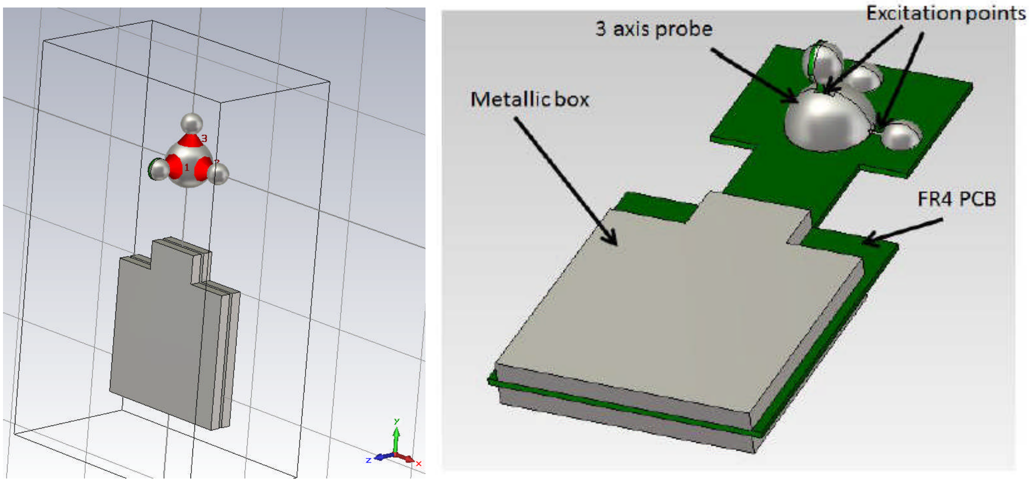

Figure 72 : Sketch of the sensor simplified model (from Satimo).

As done in the measurements se , the main characteristics of the sensor are presented first in Figure 73 to Figu

Note that the fact that a high mismatch can be observed at low frequencies (with a significant deviation from the measured results), which is probably due to the model simplification, is not of primer importance as we are dealing with isotropy considering normalized or relative quantities (i.e. the fact that the realized gain is particularly low at low frequencies is actually compensated in practice with an appropriate calibration, so that it only impacts the dosimeter sensitivity).

The quantities used in the following are the same as those defined in section 4.3.2.

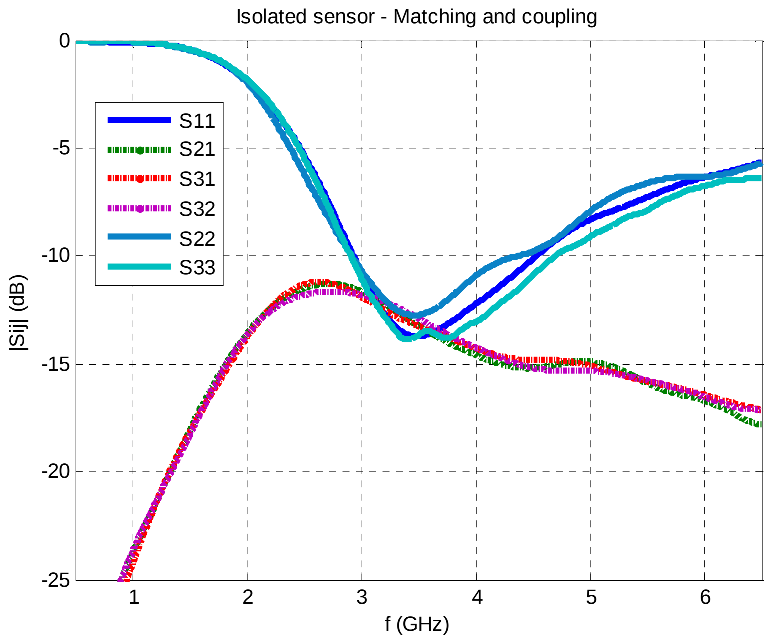

Figure 73 : Simulated reflection coefficient of each probe sensor.

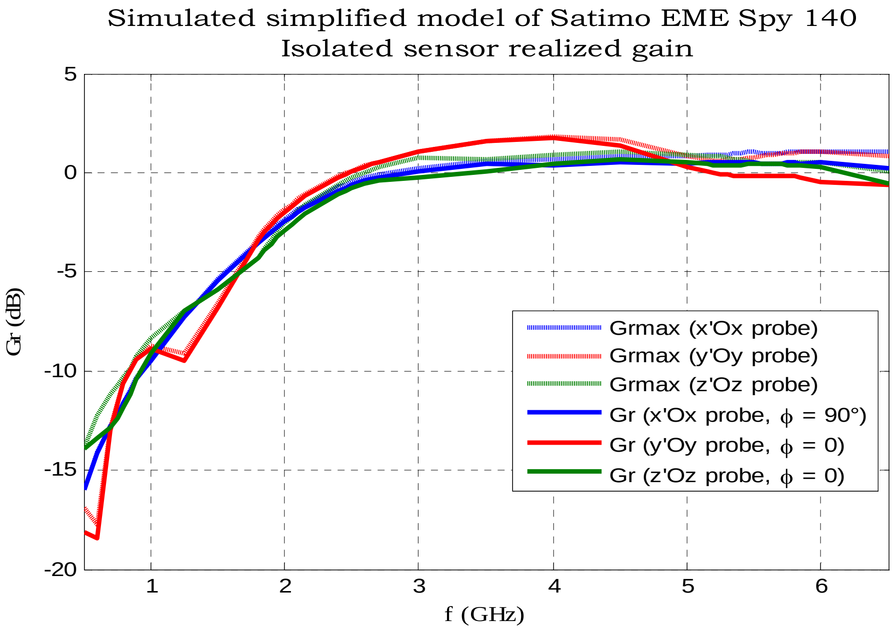

Figure 74 : Simulated realized gains per probe.

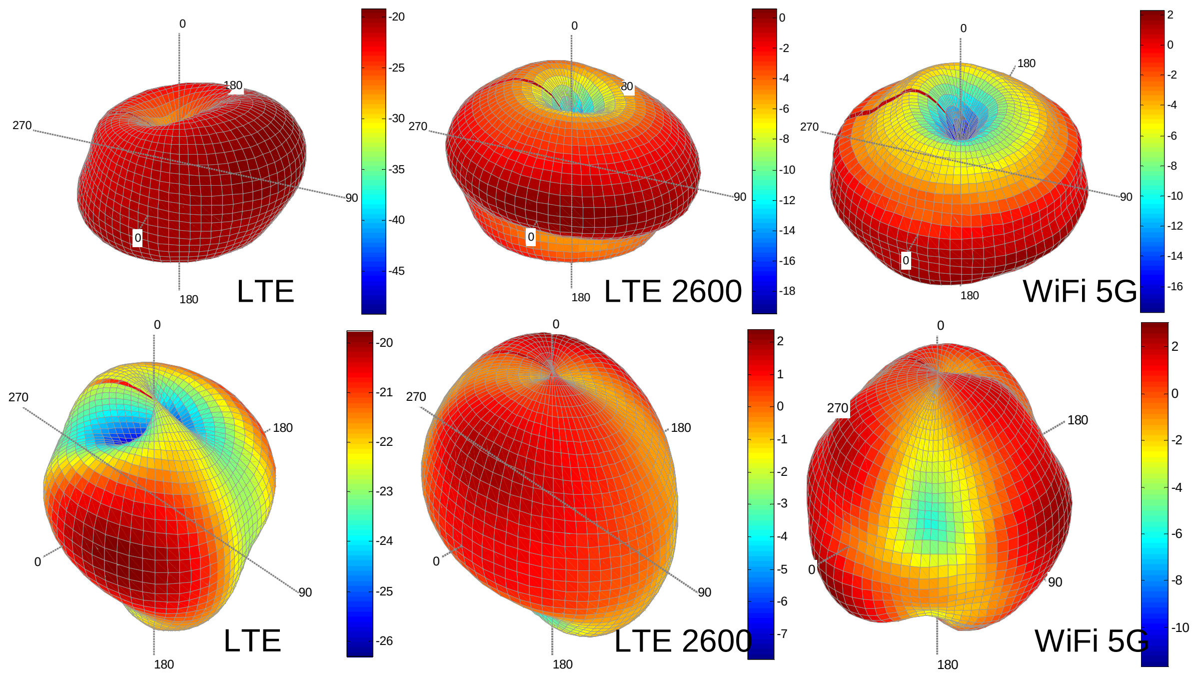

Figure 75 : Simulated 3D co-polar realized gain patterns (averaged over each RAT band, LTE 800, LTE 2600 and WiFi 5G) of the "V"(z'Oz) probe (top) and combined "H" probes (xOy) in the azimuthal plane (bottom).

4.3.1.1 Polarimetric approach

We follow the same approach here as in section 4.2.1.1.

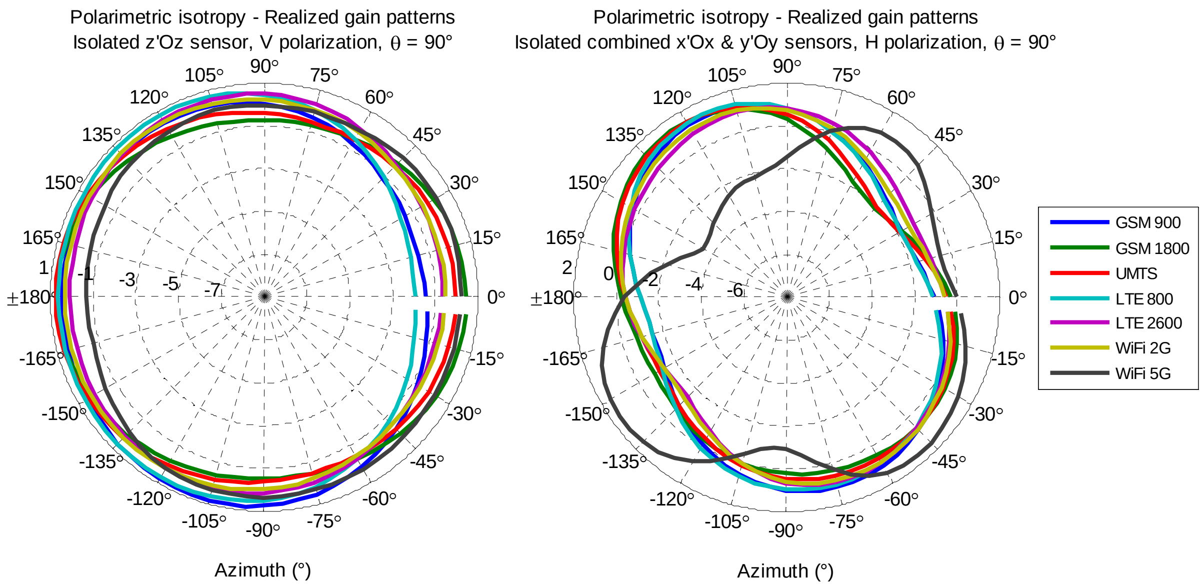

Figure 76 : Simulated normalized realized gain patterns (averaged over each RAT band) of the "V"(z'Oz) probe and combined "H" probes (xOy) in the azimuthal plane, θ = 90°.

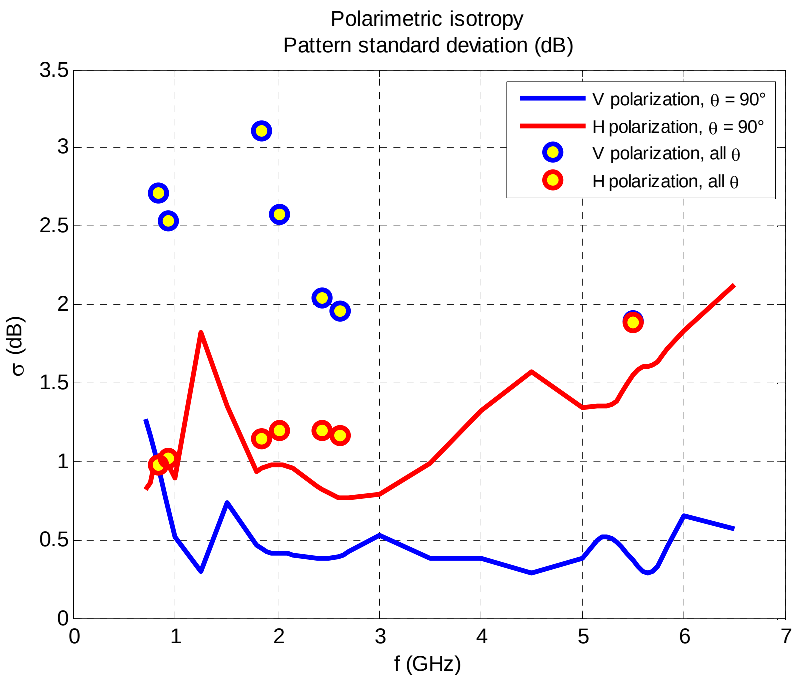

Figure 77 : Simulated normalized realized gain pattern standard deviation over azimuth (averaged over frequency for each RAT – yellow circles) of the "V"(z'Oz) probe and combined "H" probes (xOy), all θ (circles) and φ = 90° (plain).

Table 30 : Polarimetric isotropy statistics (over azimuth and elevation), in dB

	GSM 900	GSM 1800	UMTS	LTE 800	LTE 2600	WiFi 2G	WiFi 5G
μ_{Gv}	–0.52	–0.75	–0.56	–0.59	–0.32	–0.35	–0.33
σ_{Gv}	**2.53**	**3.10**	**2.57**	**2.71**	**1.96**	**2.04**	**1.89**
μ_{Gh}	0.12	0.14	0.16	0.11	0.14	0.16	0.19
σ_{Gh}	**1.02**	**1.14**	**1.19**	**0.98**	**1.16**	**1.20**	**1.89**

As can be observed in Figure 76, Figure 77and in Table 30, the "isotropy" is very satisfactory (typ. $\sigma_G < 3$ dB), and similar to the measured one (Figure 47, Figure 48 and Table 20) in particular in H polarization. The variance is slightly higher in V polarization (by about 1.5 – 2 dB) because all θ are considered (whereas only the azimuthal plane was considered in the measurements).

The XPR is very satisfactory for the V probe over a wide solid angle around the horizon (typ. less than –10 dB). It is a little bit higher for the H probes in particular for the lower frequency bands (typ < –5 dB), in agreement with the measurements.

4.3.1.2 Non polarimetric approach

❑ *INFLUENCE OF THE INCIDENT FIELD POLARIZATION*

As expected, the isotropy is slightly improved when we resort to a non polarimetric received signal (combining all probe signals), as can be observed in the following figures.

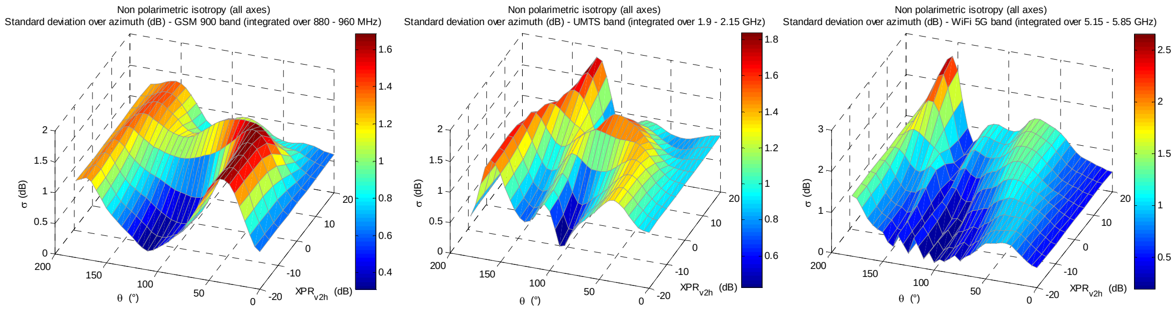

Figure 78 : Influence of the incoming wave XPR level on the isotropy (for various RATs): standard deviation of the received non polarimetric signal.

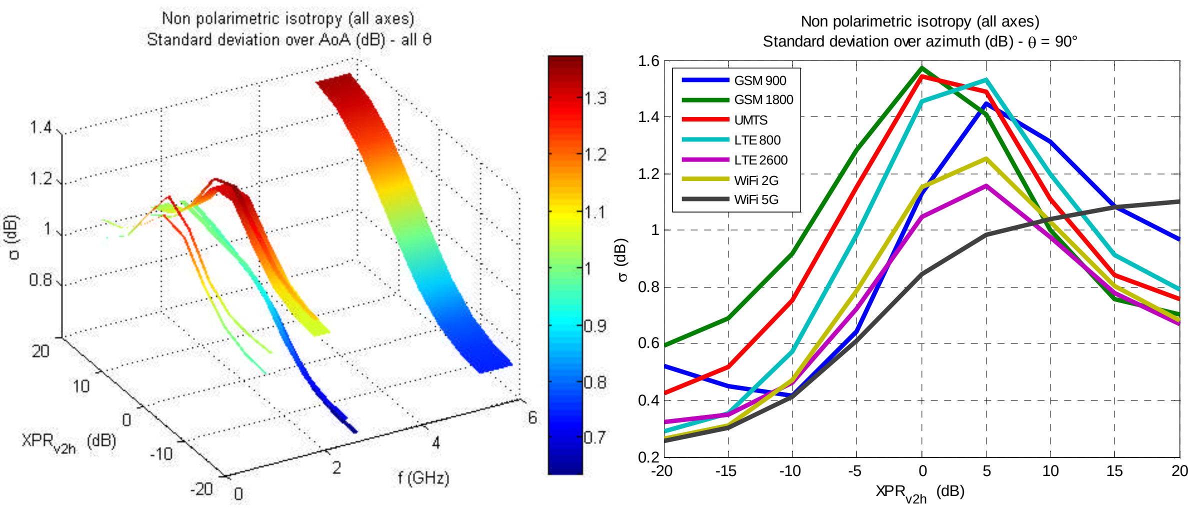

Figure 79 : Influence of the incoming wave XPR level on the isotropy (for each RATs): standard deviation of the received non polarimetric signal.

❑ *INFLUENCE OF THE CHANNEL CHARACTERISTICS*

We give only a few results for Environments n° 1 and 2 here, for sake of brevity.

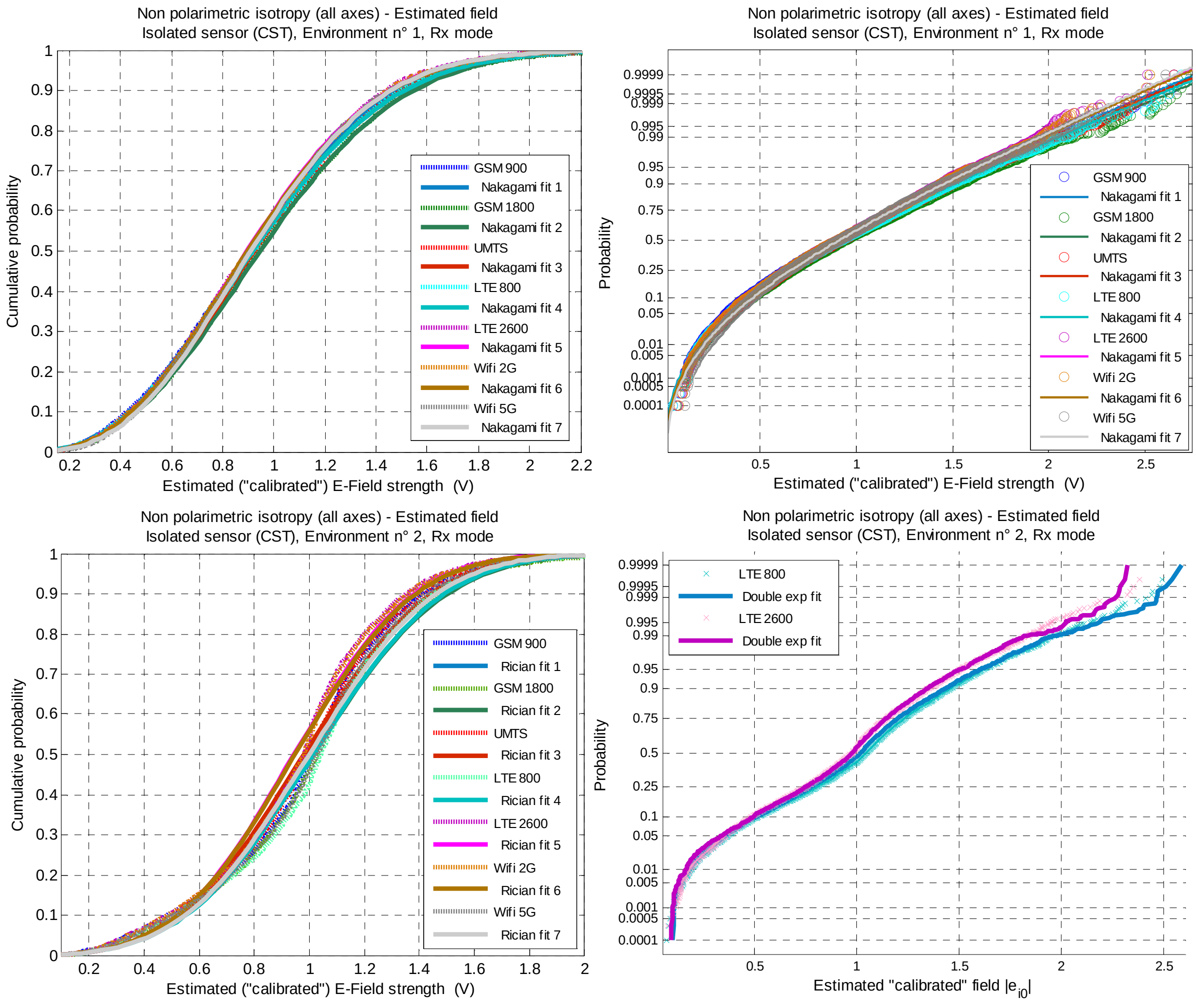

Figure 80 : Non polarimetric statistics (CDF) of isotropy deviation and examples of statistical fits for an NLOS and a LOS environments (n° 1 & 2, based on WINNER+ 3D channel models).

For Env. n° 1 (LOS), Nakagami fits are convenient, whereas for Env. n° 2 (NLOS) double exponential fits are clearly better than Rician (or Nakagami). All are rather far from normality.

Both for the "bias" (μ_{ei0}) and the isotropy deviation (σ_{Ei0}), results (Figure 80 and Table 31 and Table 32) are similar to the measured ones (Table 23 and Table 24), but all elevations are taken into account here whereas only the azimuthal plane was considered in the measurements. The same conclusion holds for both environments.

In addition, it must be underlined that these moments are almost independent on the frequency band.

Table 31: Non polarimetric sensor isotropy deviation statistics (over θ and φ) for Env. n° 1.

e_{i0norm}	GSM 900	GSM 1800	UMTS	LTE 800	LTE 2600	WiFi 2G	WiFi 5G
μ_{ei0}	**0.93**	**0.98**	**0.96**	**0.95**	**0.93**	**0.93**	**0.94**
σ_{ei0}	0.41	0.42	0.41	0.41	0.39	0.39	0.
m_{Ei0} (dB)	–0.91	–0.55	–0.70	–0.73	–0.90	–0.88	–0.84
σ_{Ei0} (dB)	**4.34**	**4.22**	**4.21**	**4.33**	**4.18**	**4.19**	**3.98**

Table 32: Non polarimetric sensor isotropy deviation statistics (over θ and φ) for Env. n° 2.

e_{i0norm}	GSM 900	GSM 1800	UMTS	LTE 800	LTE 2600	WiFi 2G	WiFi 5G
μ_{ei0}	**0.99**	**1.02**	**0.99**	**1.02**	**0.95**	**0.95**	**1.00**
σ_{ei0}	0.35	0.37	0.35	0.36	0.33	0.34	0.35
m_{Ei0} (dB)	0.10	0.24	–0.02	0.35	–0.17	–0.16	0.25
σ_{Ei0} (dB)	**3.95**	**3.87**	**3.85**	**3.95**	**3.86**	**3.84**	**3.87**

❑ *POLARIMETRIC XPR*

For brevity, the detailed results are not presented here, but the trends are the same as for the measurements, i.e. a significant increase of the XPR notably for the "V" probe, including in the visible region.

4.3.2 Realistic body model simulations

4.3.2.1 Simulated body impact (Duke): static body

The simulations of the body impact with a realistic model (static) were performed with the time domain solver of CST MWS®,, using a male voxel model (Duke, from the Virtual Population [18]). The results vary depending on:

- frequency: [0.4, 6] GHz,
- location of the dosimeter: waist or chest,
- distance from the dosimeter to the body: {0, 5} cm, *i.e.*, dosimeter attached to the skin or to the clothes, respectively.

The results of this study contain, for each of the 3 dosimeter's probes, the reflection coefficient (S_{11}), as well as the gain patterns for:

• isolated dosimeter (without the body),

• dosimeter on the body with given placement.

An evaluation parameter describing the influence of the body on the performance of the dosimeter is also proposed. This parameter is based on the probe's realised gain, which is the probe's gain reduced by the losses due to the mismatch factor of the antenna input impedance to a specified impedance, [33]:

$$G_R(\theta,\varphi) = \eta \times G(\theta,\varphi) \quad (3.11.11)$$

where η is the impedance mismatch factor, defined as:

$$\eta = (1 - S_{11}^2) \quad (3.11.12)$$

The proposed metric is termed realised gain difference, as it corresponds to the difference between the realised gain patterns of the on-body dosimeter and the isolated one, calculated in all directions (*i.e.*, horizontal and elevation angles):

$$\Delta G_R(\theta,\varphi)_{[\mathrm{dB}]} = G_{R\,body}(\theta,\varphi)_{[\mathrm{dBi}]} - G_{R\,isolated}(\theta,\varphi)_{[\mathrm{dBi}]} \quad (3.11.13)$$

The added value of this metric is that it can be easily used to quantify the measurement uncertainty, as well as being included into the probe's reading, in order to compensate the losses caused by the presence of the user.

In **Figure 81**, the impact of the presence of the body on the probes' reflection coefficient, S_{11}, is presented for the dosimeter located on the waist. The analysis of S_{11} is important to quantify the reflection losses caused by the presence of the body.

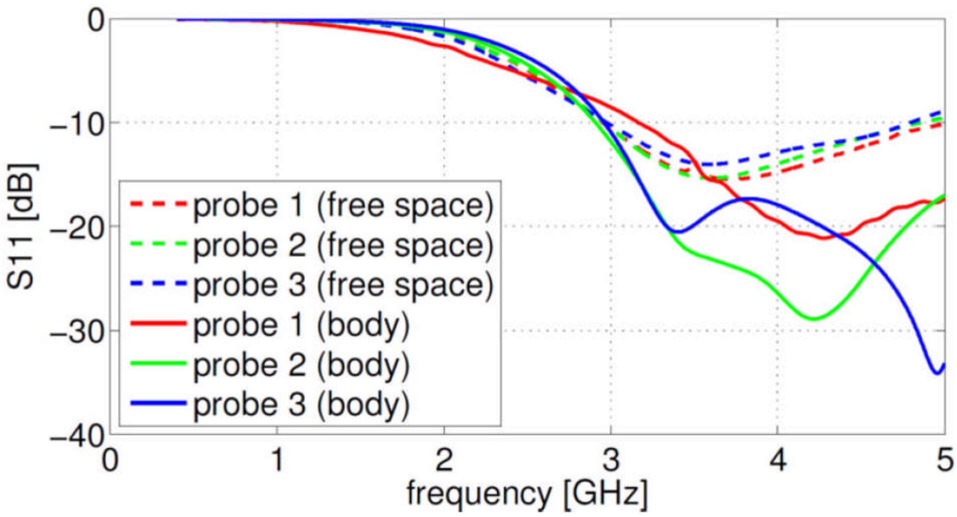

Figure 81: s_{11} for the dosimeter's probes (waist)

The input reflection coefficient of the 3 probes is affected by the presence of the body, particularly for probes 2 and 3. For instance, the S_{11} coefficient of probe 3 can decrease up to 20 dB at higher frequencies. Additionally, there is a detuning from the isolated dosimeter, affecting the EMF readings for some frequencies.

Figure 82 and Figure 83 show the gain patterns of the dosimeter probes for the isolated case and for the dosimeter located on the waist, respectively.

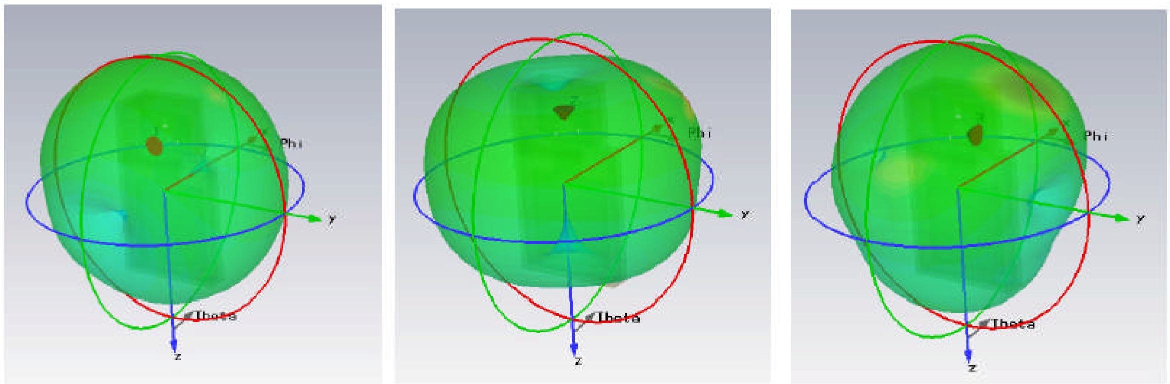

(a) probe 1 (b) probe 2 (c) probe 3

Figure 82: Radiation of the Isolated Dosimeter at 2.6 GHz

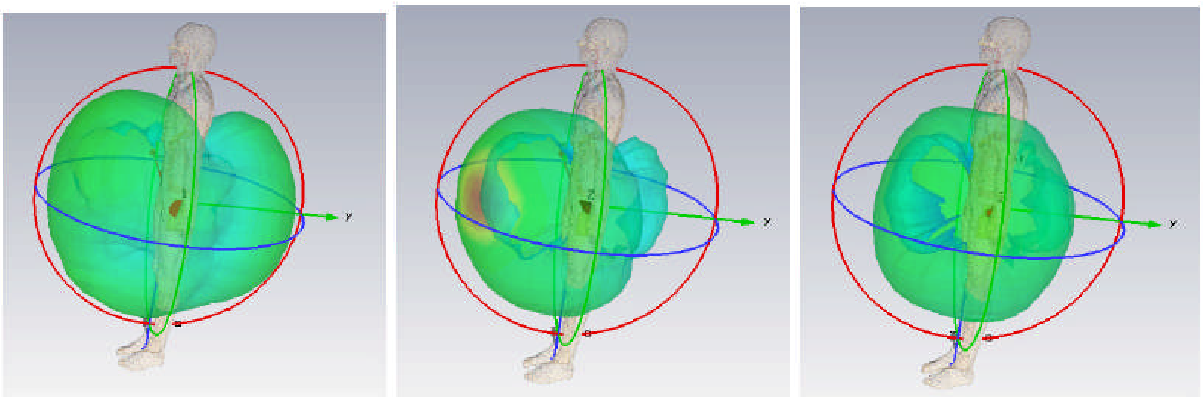

(a) probe 1 (b) probe 2 (c) probe 3

Figure 83: Radiation of the dosimeter at 2.6 GHz (waist)

At this frequency, all the probes show disturbed patterns, when compared to the isolated case. Probes 2 and 3 are particularly affected, mainly on user's direction. Probe 1 has a perpendicular orientation with respect to the user's body, thus, being less disturbed. These differences in the gain patterns were quantified for each probe, through the ΔG_R metric, whose distribution is presented in Figure 84, while Table 33 Realized gain pattern difference statistics for 2.6 GHz (waist). presents its statistics, *i.e.*, the average ($\overline{\Delta G_R}$) and the standard deviation ($\sigma_{\Delta G_R}$).

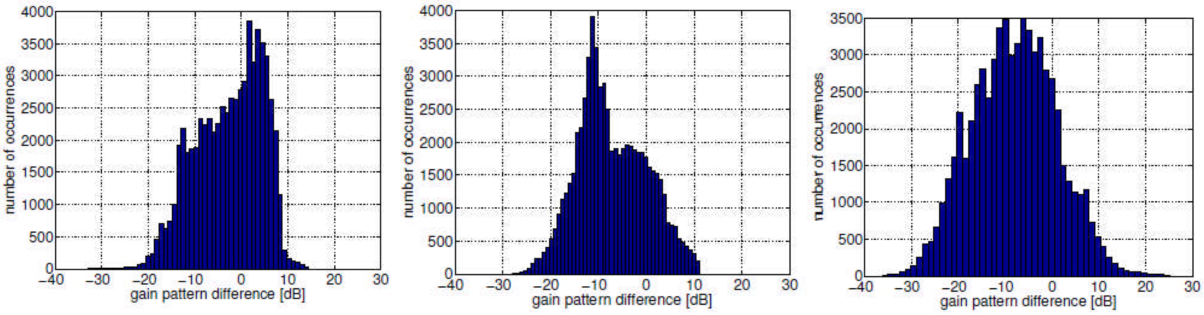

(a) probe 1 (b) probe 2 (c) probe 3

Figure 84: Realized Gain pattern difference distribution at 2.6 GHz (waist).

Table 33 Realized gain pattern difference statistics for 2.6 GHz (waist).

	$\overline{\Delta G_R}$ [dB]	$\sigma_{\Delta G_R}$ [dB]
Probe 1	-2.61	7.15
Probe 2	-7.14	7.21
Probe 3	-8.06	9.04

These results evidence the higher disturbance of the radiation patterns of probes 2 and 3, where $\overline{\Delta G_R}$ reaches -7 and -8 dB, respectively. All the patterns present large fluctuations from the average, especially probe 3, whose $\sigma_{\Delta G_R}$ reaches 9 dB. It is worthwhile to mention that, on average, $\overline{\Delta G_R}$ directly affects the EMF value obtained by the dosimeter.

The wideband study of the body influence on the dosimeter performance is presented in **Figure 85**, which displays ΔG_R over the analysed frequency band. Concerning the chest location, this study was done at different distances between body and dosimeter (from 0 cm (*i.e.*, dosimeter attached to the body) to 5 cm (*e.g.*, dosimeter attached to clothe). These scenarios were also analysed through the statistics gathered in **Table 34**.

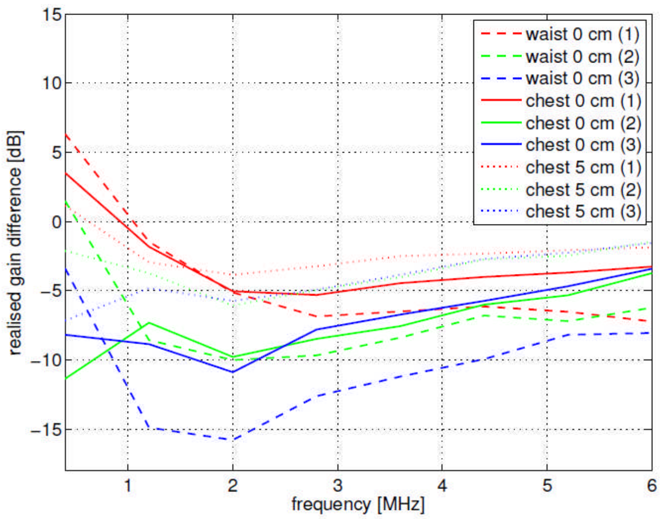

Figure 85: Realized Gain pattern difference vs. frequency (GHz).

Concerning probe 1, there are no large differences for the different locations of the dosimeter at lower frequencies, as expected, due to its perpendicular orientation to the user's body. Then, concerning probes 2 and 3, it is more evident that ΔG_R is lower when the dosimeter is further away from the body, as the body coupling effect decreases. For instance, concerning probe 3, $\overline{\Delta G_R}$, goes from -10 to -4 dB when the dosimeter is placed from 0 to 5 cm from the user.

Table 34 The average Realized Gain difference in [0.4, 6] GHz.

Dosimeter Placement	$\overline{\Delta G_R}$ [dB]		
	Probe 1	Probe 2	Probe 3
Waist 0 cm	-4.19	-6.92	-10.51
Chest 0 cm	-3.01	-7.45	-7.04
Chest 5 cm	-2.21	-3.44	-4.12

4.3.2.2 Simulated body impact (Duke): dynamic body

The statistical analysis of the body influence (*i.e.*, body shadowing) on the performance of the dosimeter is a critical parameter, in order to evaluate real exposure. Depending on the body posture (*e.g.*, standing or sitting) different directions of radiation are obstructed. Body movements and actions imply that the pattern of shadowing is going to change. Depending on the action (*e.g.*, walking or running) various directions change in a different way, which can be described statistically.

When modelling the radio link between the dosimeter located on the body and the base station, one considers the influence of the body (*i.e.*, body coupling, [19], and body movements, [20]), and accounts for the propagation environment (*i.e.*, multipath propagation). Therefore, the modelling of the radio channel has been separated into several steps, as described in [21].

The received signal level at the dosimeter depends on the distance, d, to the base station, being modelled by the mean path loss, $L_P(d)$. Moreover, it also depends on the body shadowing (*i.e.*, determined by the body posture and orientation), and it is modelled by a random variable ΔL_B. Finally, the influence of the propagation environment (*i.e.*, multipath propagation), which results in fast fading, is modelled by a random variable ΔL_F. The total path loss is given by:

$$L_{PT}(d)[\mathrm{dB}] = L_P(d)[\mathrm{dB}] + \Delta L_B[\mathrm{dB}] + \Delta L_F[\mathrm{dB}] \quad (3.11.14)$$

The path loss strongly depends on the propagation conditions, namely Line of Sight (LoS) or Non-LoS (NLoS). Therefore, when the 3 dB beam width of the dosimeter is directed towards the base station, LoS conditions are considered.

The mean path loss, $L_P(d)$, is characterised by a log-distance linear fit of the path loss obtained for different body positions, orientations and postures:

$$L_P(d)[\text{dB}] = L_P(d_0)[\text{dB}] + 10n\,log\,10(\frac{d}{d_0}) \quad (3.11.15)$$

where:

• n: path loss exponent,

• d_0: reference distance (*i.e.*, 1 m).

In order to have a statistical viewpoint on the propagation conditions in the particular type of environment, a number of simulations (*i.e.*, channel realisations), N_s, are performed (*i.e.*, each time for randomly generated scatterers in the environment).

For each randomised environment, the body is always repeating the same behaviour, namely: position in the cell, body orientation and body posture. Therefore, for a given time instant (which always occurs for the same body posture, orientation and position in the cell), the variations in output parameters come from the differences in the propagation environment. The average total path loss, $\overline{L_{PT}\ (d)_{[\text{dB}]}}$, is calculated by:

$$\overline{L_{PT}\ (d)_{[\text{dB}]}} = \frac{1}{N_s}\sum_{s=1}^{N_s} L_{PT}\ (d,s)[\text{dB}] \quad (3.11.16)$$

where $L_{PT}\ (d,s)$ is the path loss calculated for the sth simulation.

To model body shadowing (*i.e.*, to obtain the random variable ΔL_B), the mean path loss, $L_P(d)$, is subtracted from the average total path loss, $\overline{L_{PT}\ (d)_{[\text{dB}]}}$:

$$\Delta L_B(d)_{[\text{dB}]} = \overline{L_{PT}\ (d)_{[\text{dB}]}} - L_P(d)_{[\text{dB}]} \quad (3.11.17)$$

The body shadowing is equivalent to the concept of slow fading, however, it is directly related to the body movement.

An outdoor scenario (street) has been considered, Figure 86, including a set of 6 clusters, of 3 scatterers each, with a Uniform Distribution in the street. The user is performing a double loop (of circular shape with radius 9.5 m), at both sides of the base station. A base station antenna is located in the middle of the left wall, at 2.5 m height. Simulations were repeated 20 times for random distributions of scatterers.

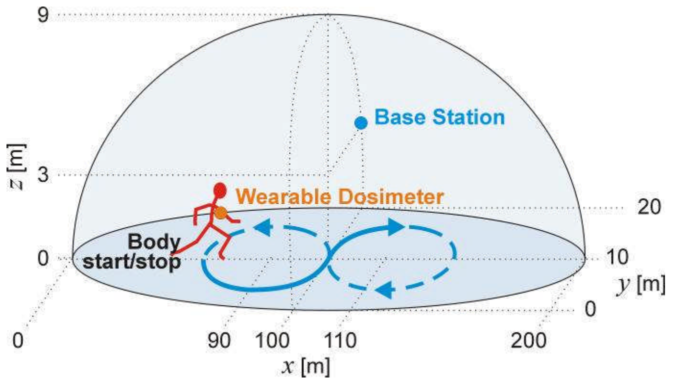

Figure 86: Street scenario (body is making a loop).

The linear fit of the mean path loss, $L_p(d)$, simulated for the dosimeter located on chest is presented in Figure 87for 2.6 GHz. It is worthwhile to draw the attention to the fact that mixed results (LoS and NLoS) represent the statistics of the radio channel, where body posture and orientation is random. However, the results for LoS and NLoS are presented, in order to allow for the comparison to the similar models drawn from the measurements, where propagation conditions can be controlled.

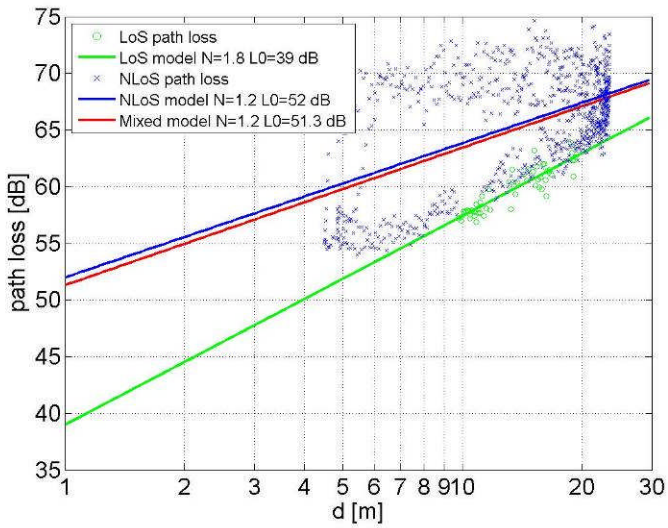

Figure 87: Linear fit of the mean path loss for dosimeter on chest (2.6 GHz).

The dispersion in the path loss is increasing when the body is standing farther away from the base station. The path loss is higher for NLoS compared to LoS, being determined by the orientation of the body. The mean path loss fit performed jointly for LoS and NLoS (mixed model) is very similar to the NLoS fit, with n=1.2 and L_0 ranging in [51, 52] dB. The LoS fit shows an exponent very similar to free space propagation (n=1.8), as expected.

The distribution of the body shadowing component, for 0.9 GHz and 2.6 GHz is presented in Figure 88 and Figure 89, respectively.

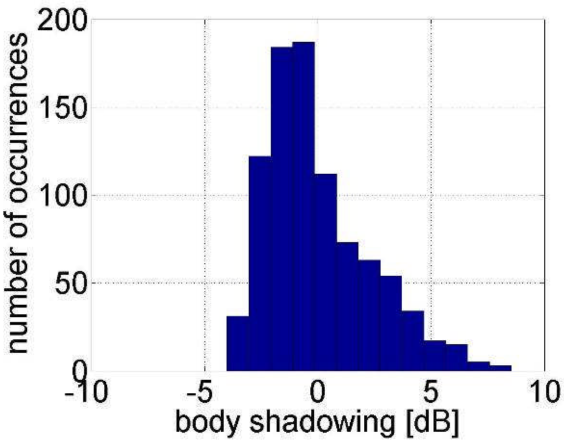

Figure 88: Distribution of the body shadowing component (0.9 GHz).

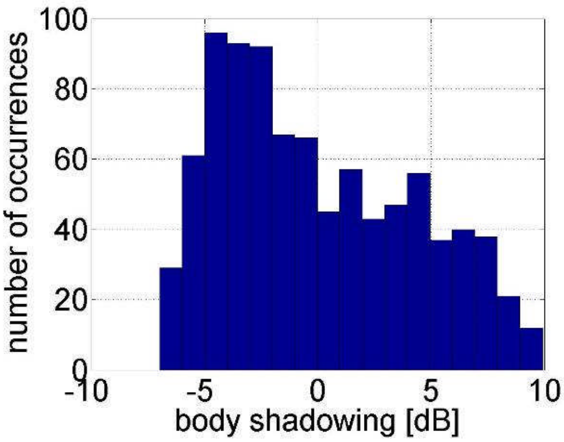

Figure 89: Distribution of the body shadowing component (2.6 GHz).

As expected, due to the changes of the body posture and orientation, the body shadowing varies significantly. The distribution of the body shadowing depends on the frequency, being larger for the higher one (2.6 GHz). It is worthwhile to notice that the specific distribution to fit the body shadowing has not been found yet.

4.3.2.3 Simulated body impact analysis : dosimeter worn on the chest

The purpose of this analysis is to identify trends through preliminary statistical assessments. A “small” phantom has been chosen to minimize the simulation time: “Eartha”, an 8-years old child girl (see Table 29). The sensor is placed at a few millimetres from her chest (Figure 90).

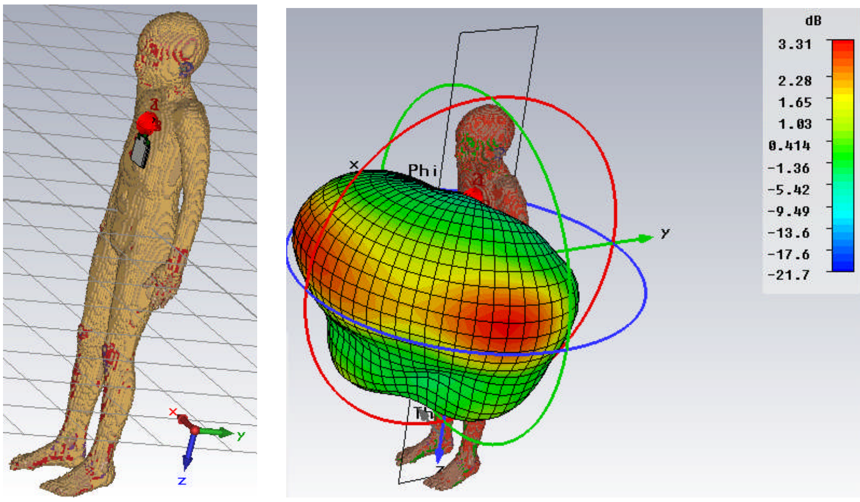

Figure 90 : (a) Sketch of the triaxial sensor placed on Eartha's phantom chest, (b) Example of realized gain pattern (2.5 GHz, □-polarization).

The Tx antenna transfer function (ATF) $\mathcal{H}(f,\theta,\varphi)$ [16] is computed from the Far Field calculated over 0.5 – 6 GHz by the time domain solver of CST Microwave Studio®, for each axial probe.

The main characteristics of the body-worn sensor are shown below as before (Figure 91).

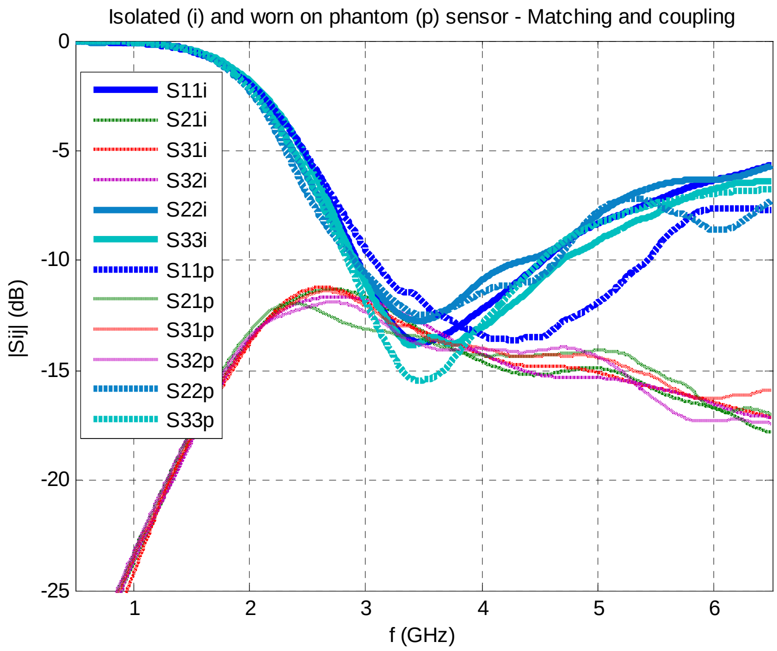

Figure 91 : Simulated reflection coefficient of each probe sensor – comparison between the worn and isolated cases.

As was observed in the measurement case, the body proximity has a moderate effect on the matching (it is even marginal here). The (co-polar) MRG (averaged over 0.7 – 6 GHz) for the "V" probe and combined "H" probes are shown in Figure 92. This gives an overview of the masking effect of the phantom.

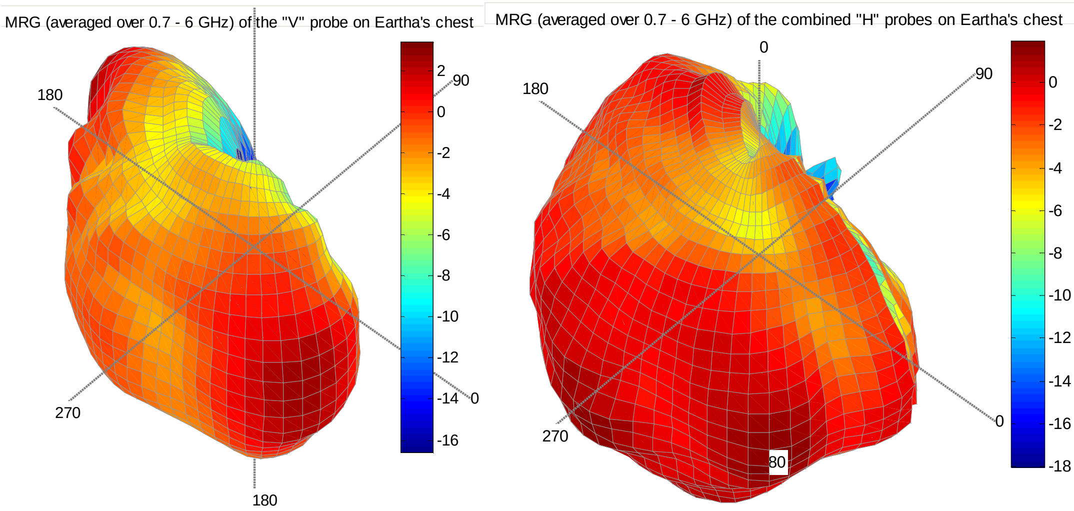

Figure 92 : MRG (co-polar components) of "V" and "H" probes on Eartha's chest averaged over 0.7 – 6 GHz (3D radiation patterns).

4.3.2.3.1 Polarimetric approach

The polarimetric gain "isotropy" is considered in Figure 93. First, a significant "bias" can be observed (Figure 94 and Table 35) in particular for the "V" probe. This is due to the energy absorbed by the body. However, this effect is less pronounced (by about 1 to 5 dB) than for the measurements (see Table 26). The deviation compared to measurements is lower for the "H" probes (within about 1 to 3 dB). Note that the phantoms sizes are significantly different, precluding any strict comparisons: only the trends should be considered here, and they are globally similar.

Apart for a few cases, the isotropy variances are in better agreement: the standard deviations remain high in particular for the "V" probe (~ 7 – 10 dB). This effect is significantly less pronounced for the "H" probes, in qualitative agreement with the measurements (see Figure 66 and Table 26).

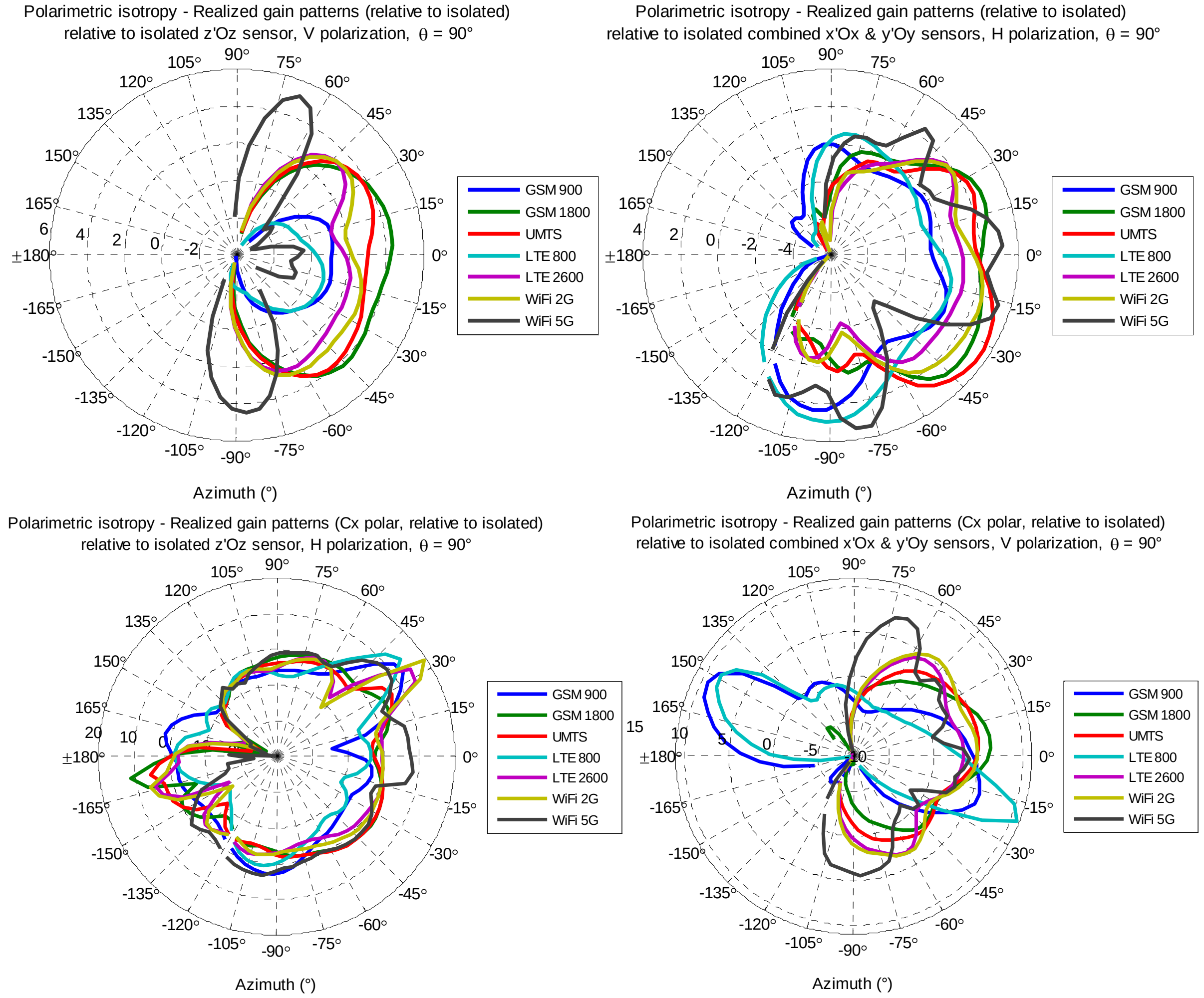

Figure 93 : Relative (to isolated) realized gain patterns (averaged over each RAT band) of the "V"(z'Oz) probe and combined "H" probes (xOy) in the azimuthal plane for the sensor worn on eartha's chest scenario, θ = 90°. Co-polar (top) and cross-polar (bottom).

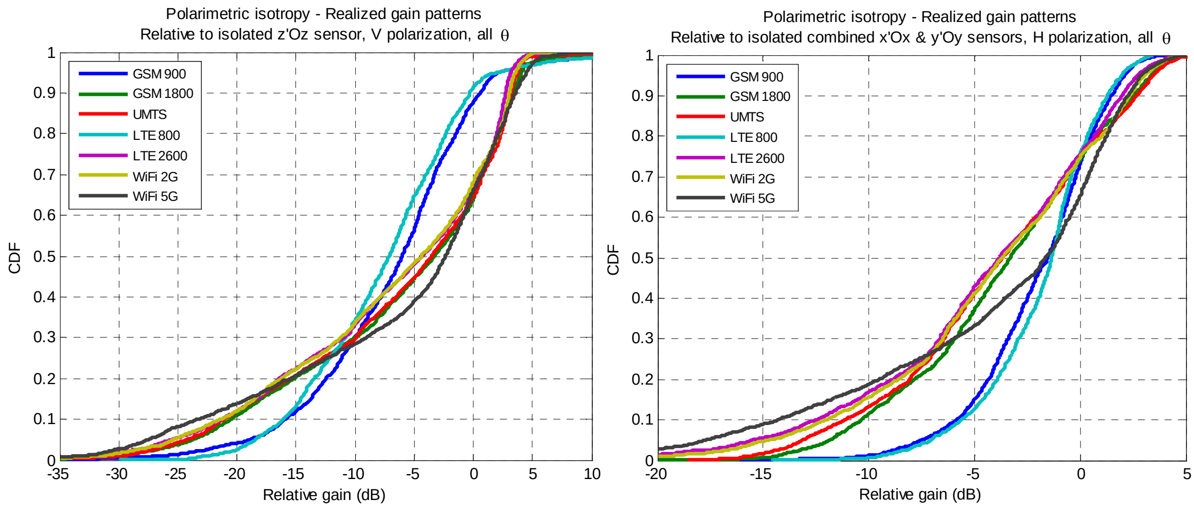

Figure 94 : Polarimetric "isotropy" (averaged over each RAT band) of the "V"(z'Oz) probe and combined "H" probes (xOy) for the sensor worn on Eartha's chest (relative to isolated), all φ.

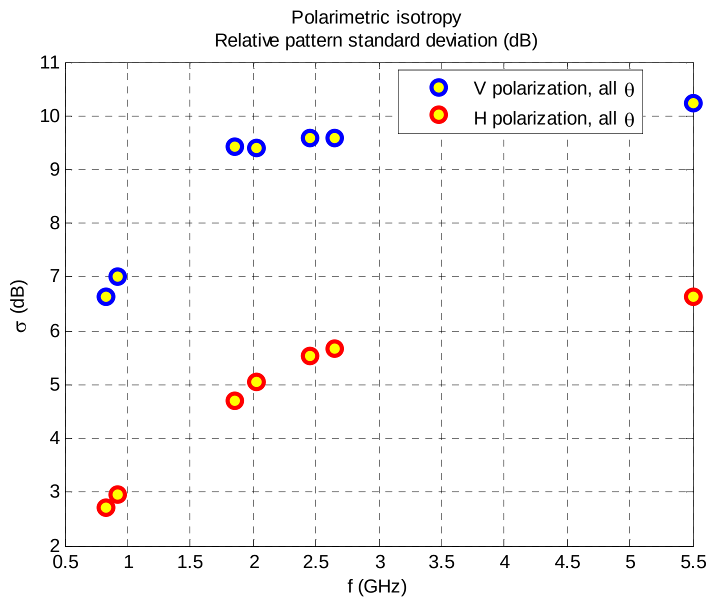

Figure 95 : Simulated realized gain pattern (relative to isolated) standard deviation over azimuth (averaged over frequency for each RAT – yellow circles) of the "V"(z'Oz) probe and combined "H" probes (xOy), all φ.

Table 35: Polarimetric isotropy statistics (over φ and θ), Eartha's chest (dB)

	GSM 900	GSM 1800	UMTS	LTE 800	LTE 2600	WiFi 2G	WiFi 5G
μ_{Gv}	–6.93	–6.03	–6.29	–7.52	–6.99	–6.97	–6.22
σ_{Gv}	**7.02**	**9.42**	**9.40**	**6.62**	**9.58**	**9.59**	**10.22**
μ_{Gh}	–2.02	–3.61	–3.90	–1.85	–4.51	–4.24	–4.07
σ_{Gh}	**2.95**	**4.70**	**5.04**	**2.71**	**5.66**	**5.53**	**6.64**

4.3.2.3.2 Non polarimetric approach

The influence of the incident field polarization is now considered. In the following figures (Figure 96 to Figure 99), the realized gains are *relative* to the isolated case (see section 4.2.2.3).

The influence of the incoming wave XPR can be clearly seen. It is particularly significant for elevations around the horizon, which concentrate most of the energy for most typical environments studied in practice. This result again prompts to take into account the characteristics of the propagation channel.

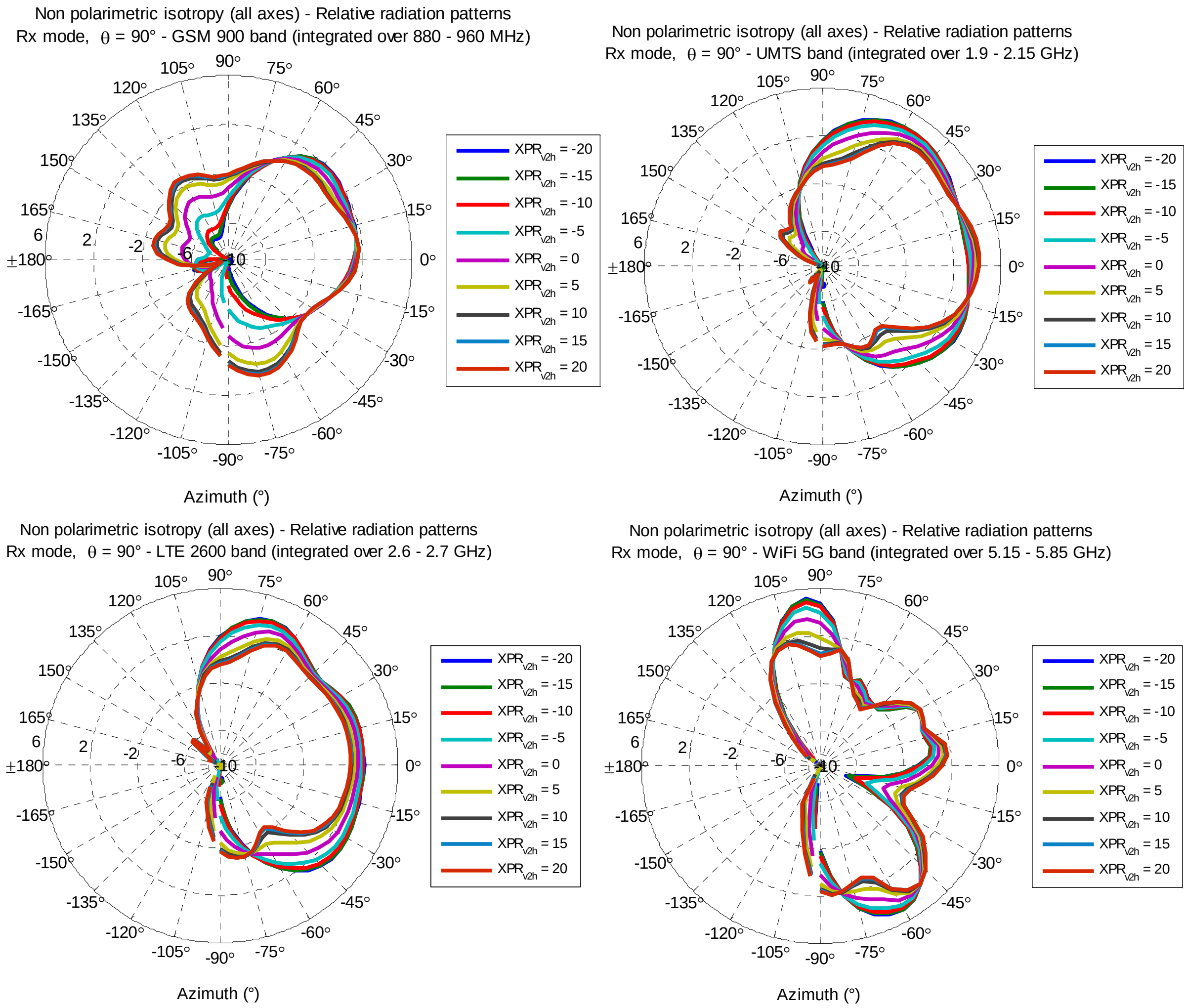

Figure 96 : Influence of the incoming wave XPR level on the isotropy (for various RATs), (a-e) received signal in azimuth (relative to isolated sensor), (f) variance of the isotropy (θ = 90°).

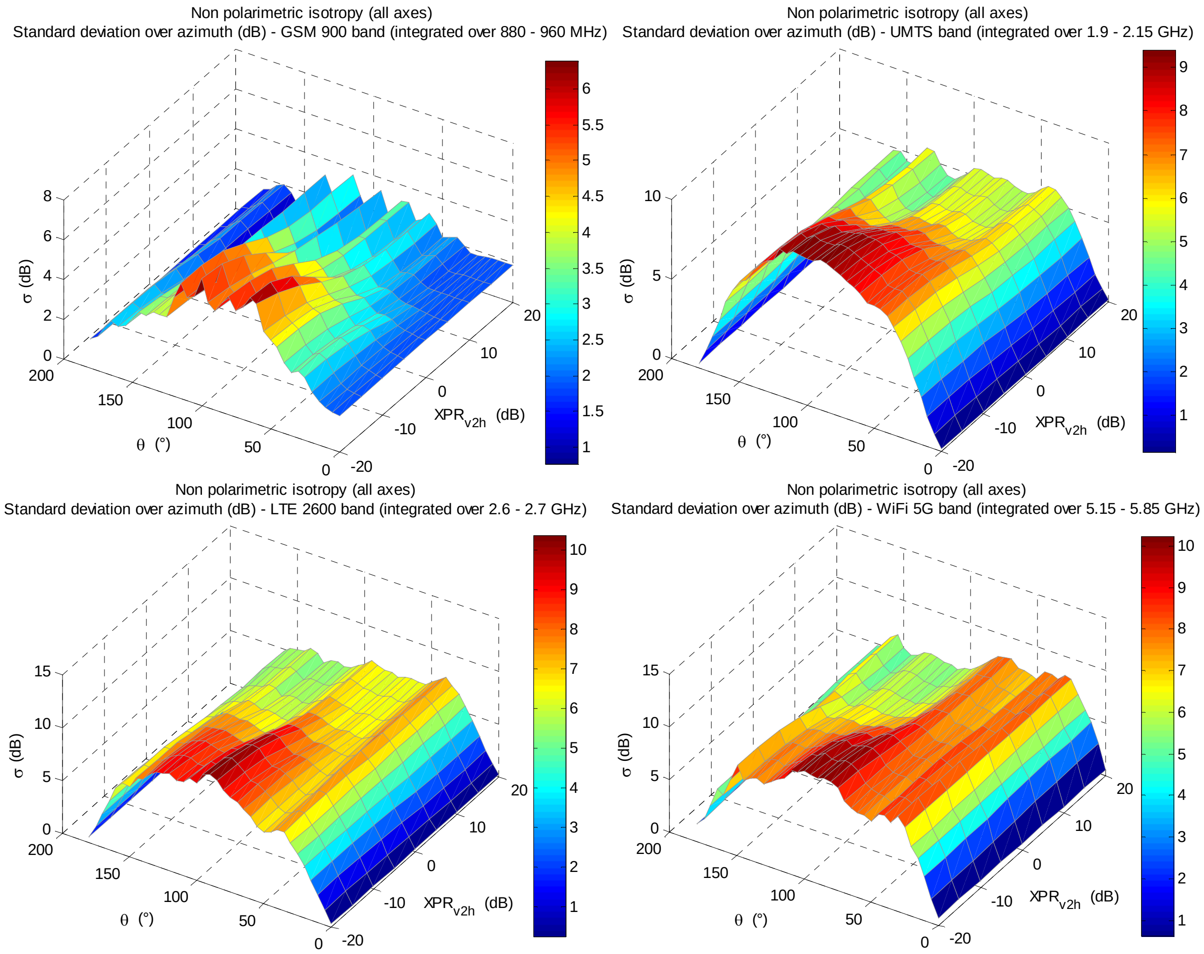

Figure 97 : Influence of the incoming wave XPR level on the isotropy (for various RATs): standard deviation of the received non polarimetric signal (relative to isolated sensor).

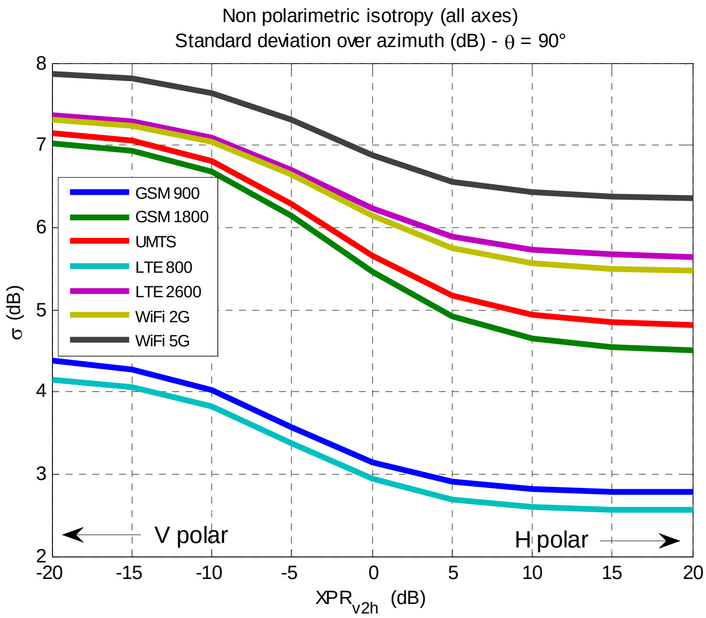

Figure 98 : Influence of the incoming wave XPR level on the isotropy (for all RATs): standard deviation of the received non polarimetric signal (relative to isolated sensor), θ =90°.

Influence of the channel characteristics

The analysis is restricted here to environments n° 1 (LOS) and 2 (NLOS) for brevity.

Both the “bias” (μ_{ei0}) and the isotropy deviation (σ_{Ei0}), results (Figure 99, Table 36, and Table 37) should be compared to those of the isolated case (Figure 48 and Table 20) on the one hand, and to the standard deviations obtained in the polarimetric analyses (Table 21).

The biases for both environments are non-negligible, the means (Tables 32 and 33) ranging typically between 0.6 and 0.85 V/m (instead of 1 V/m), but the main difficulty is of course the significant variances (up to almost 10 dB).

This should be of course corrected somehow.

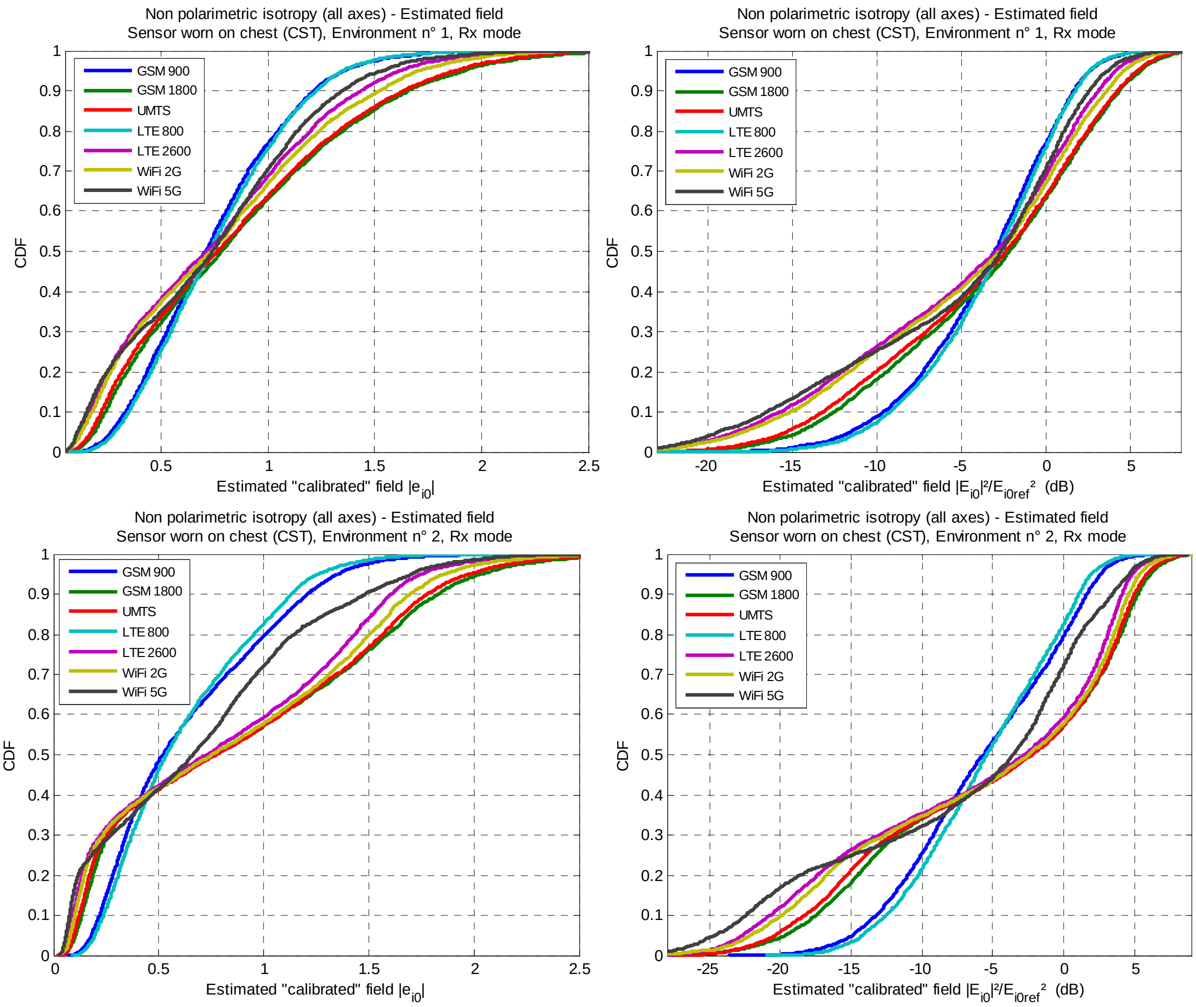

Figure 99 : Non polarimetric statistics (CDF) of isotropy deviation for an NLOS (left) and a LOS (right) environments. Sensor worn by Eartha (signal relative to isolated case).

Table 36 : Non polarimetric sensor isotropy deviation statistics (over θ and φ) for Env. n° 1.

e_{i0norm}	GSM 900	GSM 1800	UMTS	LTE 800	LTE 2600	WiFi 2G	WiFi 5G
μ_{ei0}	**0.75**	**0.87**	**0.85**	**0.76**	**0.75**	**0.79**	**0.74**
σ_{ei0}	0.44	0.57	0.57	0.41	0.56	0.57	0.53
m_{Ei0} (dB)	–3.00	–2.13	–2.33	–2.75	–2.90	–2.66	–2.62
σ_{Ei0} (dB)	**4.39**	**6.40**	**6.60**	**4.23**	**7.22**	**7.19**	**7.27**

Table 37 : Non polarimetric sensor isotropy deviation statistics (over θ and φ) for Env. n° 2.

e_{i0norm}	GSM 900	GSM 1800	UMTS	LTE 800	LTE 2600	WiFi 2G	WiFi 5G
μ_{ei0}	**0.64**	**0.89**	**0.87**	**0.62**	**0.80**	**0.84**	**0.70**
σ_{ei0}	0.39	0.69	0.67	0.35	0.61	0.65	0.54
m_{Ei0} (dB)	–5.62	–2.38	–2.19	–5.43	–2.70	–2.42	–3.54
σ_{Ei0} (dB)	**5.67**	**9.00**	**9.19**	**5.14**	**9.71**	**9.67**	**9.65**

4.3.3 Intermediate results summary tables

Table 38 : Measurement and simulation approaches summary: averages ("bias").

Detection bias	Isolated sensor												Body-worn sensor											
	Measurement						Simulation						Measurement (Chest/Hip)					(Chest)	Simulation					(Chest)
	μ_{Gv}	μ_{Gh}	$\mu_{\bar{b}}^{V}$	$\mu_{\bar{b}}^{H}$	$\bar{\mu}_{\bar{b}}$	m_{Ei0} Env. 1/2	μ_{Gv}	μ_{Gh}	$\mu_{\bar{b}}^{V}$	$\mu_{\bar{b}}^{H}$	$\bar{\mu}_{\bar{b}}$	m_{Ei0} Env. 1/2	μ_{Gv}	μ_{Gh}	$\mu_{\bar{b}}^{V}$	$\mu_{\bar{b}}^{H}$	$\bar{\mu}_{\bar{b}}$	m_{Ei0} Env. 1/2	μ_{Gv}	μ_{Gh}	$\mu_{\bar{b}}^{V}$	$\mu_{\bar{b}}^{H}$	$\bar{\mu}_{\bar{b}}$	m_{Ei0} Env. 1/2
GSM 900	–0.1	–0.5	2.5	–0.3	1.2	–0.2/**2.2**	–0.5	–0.1	–0.2	–1.2	–0.7	–0.9/0.1	–13.1/–17.2	1.4/–17.7	–5.8/–8.8	–2.6/–5.1	–3.7	**–5.3/–4.3**	–6.9	–2.2	–5.7	–3.2	–4.3	**–3.0/–5.6**
UMTS	–0.2	–0.4	0.9	0.7	0.8	–0.3/0.6	–0.6	–0.2	1.2	0.1	0.7	–0.7/–0.0	–8.8/–10.6	–3.3/–10.5	–6.3/–7.5	–5.8/–5.8	–5.5	**–7.2/–6.2**	–6.3	–3.9	–4.7	–3.7	–4.0	**–2.3/–2.2**
LTE 2600	–0.2	–0.2	0.5	–0.1	0.3	–0.6/0.1	–0.3	–0.1	–0.0	–0.5	–0.2	–0.9/–0.2	–10.6/–11.8	–3.6/–11.3	–7.2/–7.9	–6.0/–6.2	–6.0	**–7.6/–6.5**	–7.0	–4.5	–5.9	–4.9	–5.3	**–2.9/–2.7**
WiFi 5G	–0.2	–0.3	0.4	–0.0	0.2	–0.5/0.1	–0.3	–0.3	–0.7	–1.3	–1.0	–0.8/0.3	–10.2/–9.4	–4.6/–7.2	–7.2/–6.2	–7.0/–6.6	–6.5	**–5.5/–4.5**	–6.2	–4.1	–6.1	–5.3	–5.5	**–2.6/–3.5**

Table 39 : Measurement and simulation approaches summary: standard deviations.

Detection dispersion	Isolated sensor												Body-worn sensor											
	Measurement						Simulation						Measurement (Chest/Hip)					(Chest)	Simulation					(Chest)
	σ_{Gv}	σ_{Gh}	$\sigma_{\bar{b}}^{V}$	$\sigma_{\bar{b}}^{H}$	$\bar{\sigma}_{\bar{b}}$	σ_{Ei0} Env. 1/2	σ_{Gv}	σ_{Gh}	$\sigma_{\bar{b}}^{V}$	$\sigma_{\bar{b}}^{H}$	$\bar{\sigma}_{\bar{b}}$	σ_{Ei0} Env. 1/2	σ_{Gv}	σ_{Gh}	$\sigma_{\bar{b}}^{V}$	$\sigma_{\bar{b}}^{H}$	$\bar{\sigma}_{\bar{b}}$	σ_{Ei0} Env. 1/2	σ_{Gv}	σ_{Gh}	$\sigma_{\bar{b}}^{V}$	$\sigma_{\bar{b}}^{H}$	$\bar{\sigma}_{\bar{b}}$	σ_{Ei0} Env. 1/2
GSM 900	0.7	2.1	0.5	2.0	1.25	**4.7/4.4**	2.5	1.0	1.4	1.3	1.35	**4.3/4.0**	8.4/7.5	5.1/4.4	6.6/6.0	6.7/5.7	6.7/5.8	**6.3/5.3**	7.0	3.0	4.4	2.8	3.4	**4.4/5.7**
UMTS	1.2	1.8	1.0	1.6	1.7	**4.6/4.0**	2.6	1.2	1.3	1.5	1.4	**4.2/3.9**	10.6/9.5	4.7/4.2	9.6/8.9	5.9/5.8	7.6/7.2	**8.8/8.5**	9.4	5.0	7.1	4.8	5.9	**6.6/9.2**
LTE 2600	1.3	1.5	1.1	1.4	1.3	**4.3/4.0**	2.0	1.2	0.9	1.6	1.2	**4.2/3.9**	11.7/11.0	5.2/5.1	10.2/10.0	6.3/6.5	8.1/8.0	**9.8/9.8**	9.6	5.7	7.4	5.6	6.4	**7.2/9.7**
WiFi 5G	1.4	1.7	1.2	1.6	1.4	**4.2/3.8**	1.9	1.9	1.5	2.1	1.7	**4.0/3.9**	13.1/12.2	7.3/7.3	12.0/10.6	7.7/6.9	9.7/8.6	**10.5/10.5**	10.2	6.6	7.9	6.3	7.0	**7.3/9.7**

Note that the programme giving the statistical results according to the channel characteristics has been validated (among other test) with a fictive environment corresponding to the analysis of the influence of the incoming field XPR (i.e. quasi deterministic, with no cluster azimuth spread, only one path and the same spread of the XPR). The values of σ_{Ei0} obtained in this case are comparable to those of $\bar{\sigma}_{\bar{b}}$ for all cases, in particular for the isolated case.

4.3.4 Alternative approaches involving channel models

The received wave b_p at the p-th probe port is defined from the p-th ATF as in (4.2.1), As the quantities used in the following will be normalized in a way or another (but for each band separately), the coefficient $\kappa = -\frac{1}{2}j\sqrt{\frac{4\pi}{h_0}\frac{c}{\omega}}$ will now be omitted in the expression of the received signals b_p, so that $b_p(f,\hat{\mathbf{r}}) = \mathcal{H}_n^T(f,\hat{\mathbf{r}})\cdot\mathbf{E}_{i0}(\hat{\mathbf{r}})$. The incident field is a linear combination of plane waves $\mathbf{E}_{i0} = E_{i0}^V\hat{\boldsymbol{\theta}} + E_{i0}^H\hat{\boldsymbol{\varphi}}$ characterized by their amplitude E_{i0} and their cross-polarization ratio $xpr_E = \left|E_{i0}^V\right|^2/\left|E_{i0}^H\right|^2$. Whatever the considered approach in the sequel the *total* field strength will be set to 1 V/m, so that, for a single incoming plane wave:

$$E_{i0}^V = \pm\frac{xpr_E^{1/2}}{(1+xpr_E)^{1/2}} \quad \text{and} \quad E_{i0}^H = \pm\frac{1}{(1+xpr_E)^{1/2}}$$

If the incoming field is composed of Multi Path Components (MPCs), the signal received at each probe, averaged over each RAT band reads:

$$\begin{aligned} b_p(f) &= \sum_{n=1}^{N}\mathcal{H}_p^T(f,\hat{\mathbf{r}}_n)\cdot\mathbf{E}_{i0}(\hat{\mathbf{r}}_n) \\ &= \sum_{n=1}^{N}\left|E_{i0,n}^V\right|\frac{\varepsilon_\theta\mathcal{H}_p^\theta(f,\hat{\mathbf{r}}_n)xpr_{E,n}^{1/2} + \varepsilon_\varphi\mathcal{H}_p^\varphi(f,\hat{\mathbf{r}}_n)}{(1+xpr_{E,n})^{1/2}} \end{aligned}$$

under the constraint $\sum_{n=1}^{N}\left|E_{i0,n}^V\right|^2(1+xpr_n^{-1}) = 1$, where $\varepsilon_\theta = \pm 1$ and $\varepsilon_\varphi = \pm 1$, with $p\in\{x, y, z\}$ (or {1,2,3}), and where the superscript “T” has been omitted in the Tx transfer function for ease of reading.

In order to preserve the sensor isotropy as much as possible, or at least its omni-directionality for polarimetric measurements, the vertical probe on the one hand, and the horizontal probes on the other hand, are not used in a symmetrical way. For the polarimetric measurements, the considered signals, respectively mostly sensitive to the vertical or horizontal components are defined as:

$$\bar{b}_v(f_{RAT}) = \left(\frac{1}{\Delta f_{RAT}}\int_{\Delta f_{RAT}}\left|b_z(f)\right|^2 df\right)^{1/2}$$

$$\bar{b}_h(f_{RAT}) = \left(\frac{1}{\Delta f_{RAT}}\int_{\Delta f_{RAT}}\left|b_x(f)\right|^2 + \left|b_y(f)\right|^2 df\right)^{1/2}$$

whereas for the non polarimetric approach, these signals are combined as:

$$\bar{b}(f_{RAT}) = \left(\frac{1}{\Delta f_{RAT}} \int_{\Delta f_{RAT}} \sum_{p=1}^{3} \left| b_p(f) \right|^2 df \right)^{1/2}$$

ISOLATED SENSOR

Calibration – Normalization schemes

In the field assessment process, two aspects should be considered: first, the sensor deviation to isotropy (or omni-directionality), and second the measurement "bias", which is defined here as the deviation between the average value of the field measurement and the true value. The last is in particular affected by the way the calibration procedure is applied, i.e. the way the raw measurements are normalized. Various options are possible. The simplest is based on the intrinsic directional characteristics of the sensor (actually the partial realized gains), irrespective of the considered environment (i.e. on the channel characteristics):

$$\bar{b}_v^{ref}(f_{RAT}) = \frac{1}{2\pi} \int_0^{2\pi} \left(\frac{1}{\Delta f_{RAT}} \int_{\Delta f_{RAT}} \left| \mathcal{H}_z^{\theta}(f, \tfrac{\pi}{2}, \varphi) \right|^2 df \right)^{1/2} d\varphi$$

$$\bar{b}_h^{ref}(f_{RAT}) = \frac{1}{2\pi} \int_0^{2\pi} \left(\frac{1}{\Delta f_{RAT}} \int_{\Delta f_{RAT}} \sum_{p=x,y} \left| \mathcal{H}_p^{\varphi}(f, \tfrac{\pi}{2}, \varphi) \right|^2 df \right)^{1/2} d\varphi$$

$$\bar{b}^{ref}(f_{RAT}) = \frac{1}{2\pi} \int_0^{2\pi} \left(\frac{1}{\Delta f_{RAT}} \int_{\Delta f_{RAT}} \sum_{p=1}^{3} \left| \mathcal{H}_p^{\varphi}(f, \tfrac{\pi}{2}, \varphi) \right|^2 df \right)^{1/2} d\varphi$$

A close alternative is to take into account a solid angle around the azimuthal plane, averaging over a reasonable elevation range [$\pi/2 - \theta_{max}$, $\pi/2 + \theta_{max}$] which contains in practice most of the energy for most of the typical channels, i.e.:

$$\bar{b}_v^{ref}(f_{RAT}) = \frac{1}{4\pi \sin\theta_{max} \Delta f_{RAT}} \iint_{\Delta\Omega} \left(\int_{\Delta f_{RAT}} \left| \mathcal{H}_z^{\theta}(f, \theta, \varphi) \right|^2 df \right)^{1/2} d\theta d\varphi$$

These normalization quantities necessarily induce a bias in the statistical assessment of the field as none of them are the mean of the quantities defined in section II. However, this approach has the advantage of not requiring any knowledge or intervention from the user.

A way to get rid of the bias is to perform a statistical averaging (using a Monte Carlo sampling (MC)) for each typical type of environment. This can be done once, a priori, resorting to typical channel models, such as the WINNER2/WINNER+ models (see [21], Table 40) which are used here, i.e.:

$$\bar{b}_\alpha^{ref}(f_{RAT}, Env) = \langle \bar{b}_\alpha(f_{RAT}, Env) \rangle_{stat}$$

The drawback, which is undoubtedly unacceptable for non specialist users, is that the user should know the environment type he is sounding. Note however that some techniques able to assess propagation conditions (LOS or NLOS) exist. In any case, the estimated field is given by $\bar{e}_{\alpha}(f_{RAT}) = \frac{\bar{b}_{\alpha}(f_{RAT})}{\bar{b}_{\alpha}^{ref}(f_{RAT})}$, α representing any kind of measurement type (polarimetric or not).

These normalization quantities are presented in **Figure 100** for the ten environments considered here (see the WINNER2/WINNER+ channel models). It can be observed that the normalization with the realized gains underestimate the statistical averaging of the vertical sensor signal for all the environments, and hence for the combined non polarimetric signal $\bar{b}$. Note that the averaging over a moderate range in elevation induces only a marginal variation.

The observation of these figures show that a fourth possibility, offering an interesting compromise between accuracy and required a priori knowledge, is to consider the mean, over all the environments, of the statistical averages, i.e.:

$$\bar{b}_{\alpha,all}^{ref}(f_{RAT}) = < \bar{b}_{\alpha}^{ref}(f_{RAT}, Env) >_{Env}$$

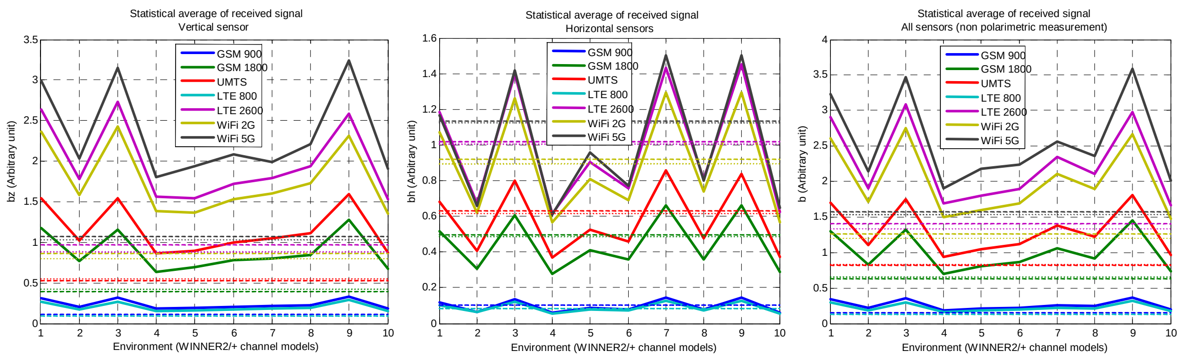

Figure 100 : Normalization quantities: (plain) statistical averaging (MC), (dashed) $<G_r>_{\varphi}$, and (dotted) $<G_r>_{\varphi,|\theta-\pi/2|<\theta max}$ ($\theta_{max} = \pi/9$ rad here (20°)).

Field assessment in various propagation environments

Results are presented as examples for two WINNER2/+ environments: indoor small office / residential, A1/NLOS (n° 1, **Figure 101**) and A2/LOS (n° 2, **Figure 102**).

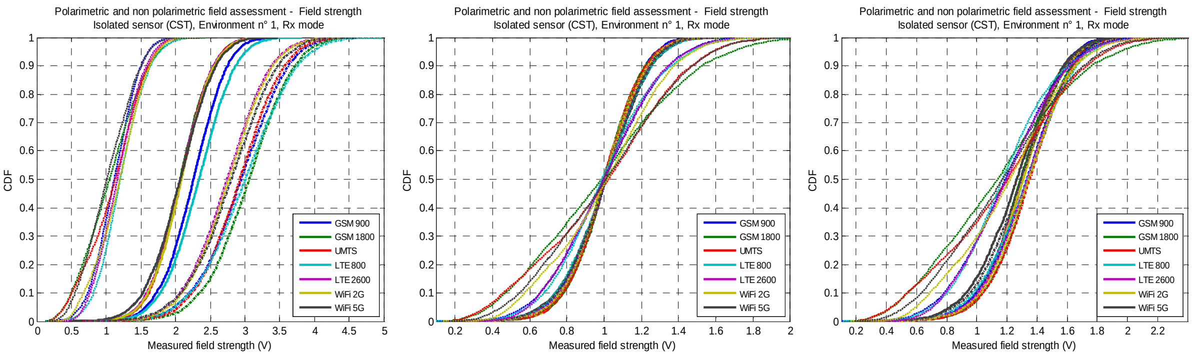

Figure 101 : Field strength assessment for the environment n° 1 (Indoor NLOS), based on: (a) $<G_r>_{\varphi}$ normalization, (b) statistical normalization per environment type, and (c) statistical normalization averaged over all environment types. Non polarimetric (plain), V sensor (dashed-dotted), and H sensors (dashed).

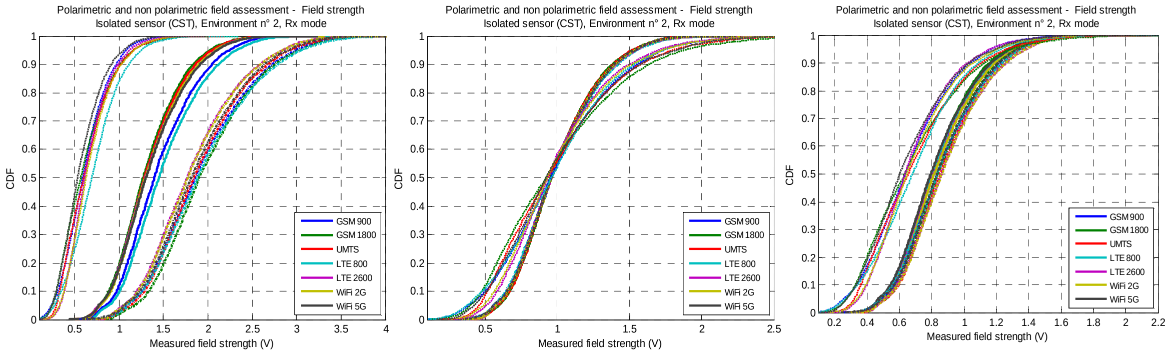

Figure 102 : Field strength assessment for the environment n° 2 (Indoor LOS), based on: (a) $<G_r>_\varphi$ normalization, (b) statistical normalization per environment type, and (c) statistical normalization averaged over all environment types. Non polarimetric (plain), V sensor (dashed-dotted), and H sensors (dashed).

As expected, for both environments, the bias is almost null for the "statistical normalization" (**Figure 101**b and **Figure 102**b). Note that for the LOS case, the distribution is clearly not normal so that the median and the mean are different. It is however unacceptable for the "$<G_r>_\varphi$ normalization", except for the H sensors for the NLOS scenario (as expected from **Figure 108**b). The bias range for the "averaged statistical normalization" is about +15 to +30 % for the 1st environment, and about –20 % for the second (in linear scale).

As can be observed in **Figure 101** and **Figure 102**, both the bias and the variance depend weakly on the frequency bands (RATs). The variance also increases when the normalization is not optimal. For the non polarimetric signal $\bar{e}$ (measuring the field amplitude), the standard deviation (RMSE) for the NLOS case is about 0.18 V/m (~1.7 dB) for the unbiased normalization, 0.24 V/m (~2.7 dB) for the "averaged statistical normalization" and 0.4 V/m for the "$<G_r>_\varphi$ normalization". For the LOS case, these quantities are respectively 0.29 V/m, 0.25 V/m, and 0.28 V/m. The "averaged statistical normalization" is consequently adopted as a good compromise between accuracy and practical usage.

It can be observed that the variance is lower for the non polarimetric and the vertical probe signals. This is mainly due to the fact that, although the channel induces depolarization effects, the main energetic contribution remains in the vertical component on the one hand, and the fact that the cross-polarization level of the horizontal probes is not negligible.

BODY-WORN SENSOR

The simulation results presented hereafter have been carried out with *Eartha*, a numerical phantom model of the Virtual Population suit (from ITI'S foundation), already presented in 4.3.1 ([18]).

The received signals are normalized as previously explained, but with the reference signals of the *isolated* sensor. In that sense, the measured normalized quantities allow to analyze the deviation to isotropy or omni-directionality due to the body proximity effects, *relative* to the isolated case.

The bias and the standard deviation of the non polarimetric signal (**Figure 103**) are respectively (depending on the RAT): 0.26 to 0.37 V/m and 0.14 to 0.26 V/m for the environment n° 1 (NLOS) and 0.25 to 0.36 V/m and 0.14 to 0.27 V/m for the environment n° 2 (LOS).

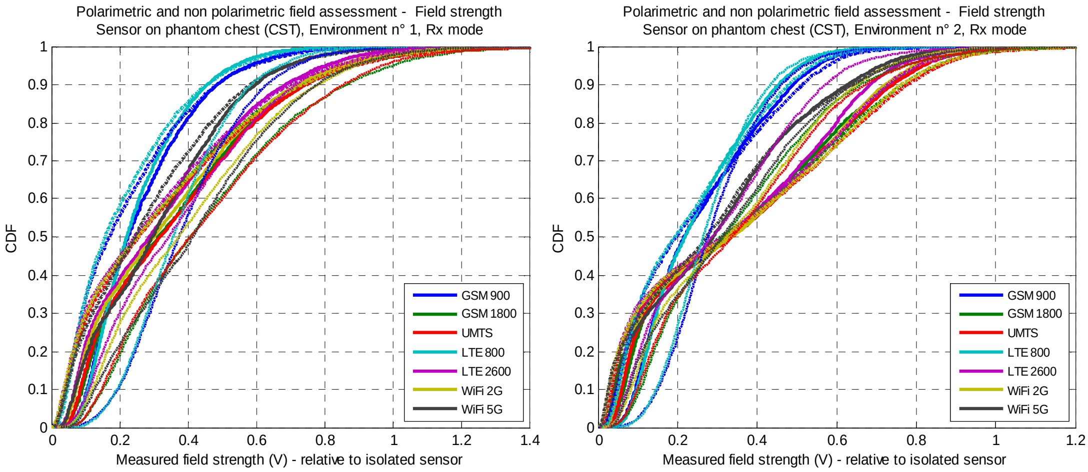

Figure 103 : Field strength assessment by the sensor worn on Eartha's chest for the environment n° 1, Indoor NLOS (top) and n° 2, Indoor LOS (bottom), relative to the *isolated* sensor statistical normalization averaged over all environment types. Non polarimetric (plain), V sensor (dashed-dotted), and H sensors (dashed).

Note however that a significant part of the values are very low, particularly for the LOS case, which correspond to the case where the direction of the BS (or the AP) is in the back of the user. This effect is even stronger when the sensor is worn by an adult male, who's wider morphology presents a larger masking area.

4.4 Studies with complete dosimeters

4.4.1 Dosimeter study in controlled environment

To compare the results of the above study carried out using the three axial probe with connecting cables and a whole body phantom, a similar study was carried out using the EMESPY 140 dosimeter in an anechoic chamber. The objective was to evaluate the variation in the dosimeter measurements over 360° when it is illuminated with a vertical / horizontal polarization over an incidence angle between -16° and +20° (which is the same as used in the previous study, characterizing the direction of arrival of most of the EMF exposure). The reason for doing this study is that there would be no effect of the connecting wires in this case, and in addition, the dosimeter measurements are post-processed in order to produce reliable measurement results, while in the previous study, raw E-field measurements were considered.

Two measurement configurations were considered in this study:

- First the dosimeter was placed alone inside an anechoic chamber and it was illuminated with a horn antenna at three vertical incidence angles (0°, +20°, and -16°). The vertical and horizontal polarization incidence was considered in each case. The dosimeter was rotated covering the 360° with a step of 10°.
- Secondly, a body liquid in a bottle was placed behind the dosimeter simulating the effect of a human torso and the above mentioned process was repeated to evaluate the effect on the isotropy of the measured E-field.

The measurement setup is presented in the Figure 104 below.

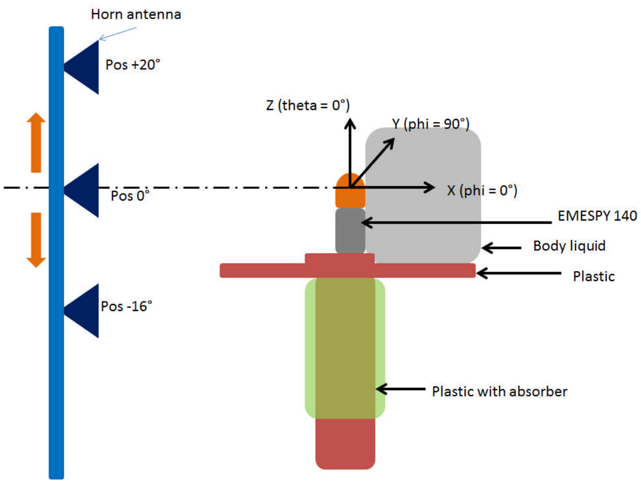

(a) Measurement steup

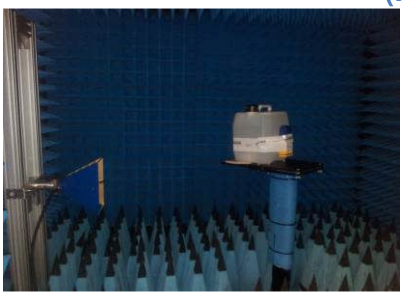

(b) EME-SPY 140 with body liquid at -16° incidence (horizontal polarization)

(c) EME-SPY 140 with body liquid at +20° incidence (vertical polarization)

Figure 104: Measurement setup for the dosimeter study in a controlled environment.

The study was carried out for incidence at a single CW frequency in the three frequency bands (GSM, DCS, and UMTS). The results are compared in Table 40.

Table 40: Results comparing the dosimeter measurements with and without a body liquid in a controlled environment.

		Mean values (V/m)		Difference in mean values	
		Alone	On body	V/m	dB
GSM-DL (900 MHz)	PV	2,0	1,1	0,9	5,1
	PH	2,5	2,2	0,3	1,0
DCS-DL (1800 MHz)	PV	2,2	1,5	0,7	3,4
	PH	2,3	2,0	0,3	1,2
UMTS-DL (2100 MHz)	PV	1,9	1,2	0,7	3,8
	PH	1,6	1,4	0,2	1,1

(a) Results for +20° incidence

		Mean values (V/m)		Difference in mean values	
		Alone	On body	V/m	dB
GSM-DL (900 MHz)	PV	3,2	1,5	1,7	6,5
	PH	2,3	2,2	0,1	0,3
DCS-DL (1800 MHz)	PV	3,0	2,0	1,0	3,5
	PH	2,7	2,3	0,4	1,5
UMTS-DL (2100 MHz)	PV	2,6	1,7	0,9	3,7
	PH	2,1	1,6	0,4	2,1

(b) Results for 0° incidence

		Mean values (V/m)		Difference in mean values	
		Alone	On body	V/m	dB
GSM-DL (900 MHz)	PV	3,6	1,4	2,3	8,5
	PH	2,0	1,9	0,1	0,2
DCS-DL (1800 MHz)	PV	1,8	1,3	0,4	2,4
	PH	2,1	1,7	0,4	1,9
UMTS-DL (2100 MHz)	PV	2,1	1,3	0,8	4,2
	PH	1,7	1,3	0,4	2,1

(c) Results for -16° incidence

The mean value is calculated for each case (dosimeter alone and with body liquid), each polarization (PH = horizontal and PV = vertical), and for each of the three frequency standards over the 360°. The results for the GSM 900 frequency for +20° (PV) and -16° (PH) incidence show a poor isotropy (even for the dosimeter alone) due to the reflections in the anechoic chamber at this frequency. The difference between the mean values for the two cases is given in V/m and in dB to have an idea about the impact of the human body (simulated by the liquid bottle).

To have an idea of the variation of the E-field over 360°, few interesting results are presented in Figure 105 for the DCS signal.

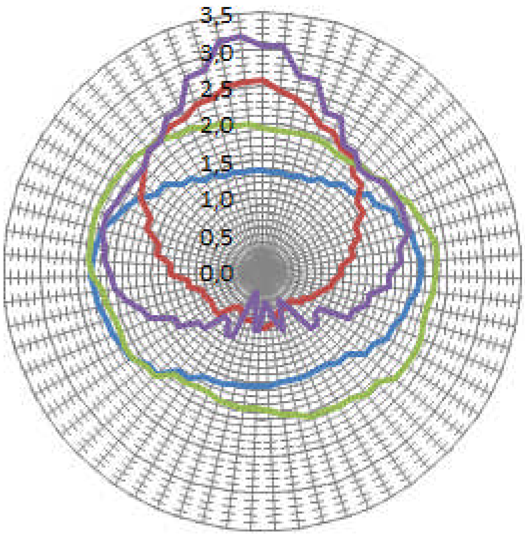

(a) DCS results with -16° incidence

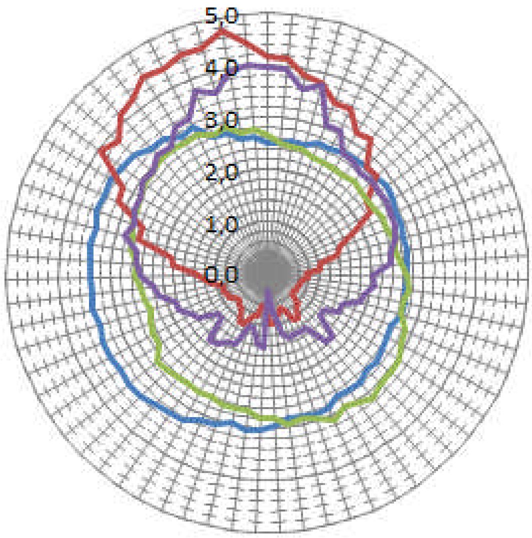

(b) DCS results with 0° incidence

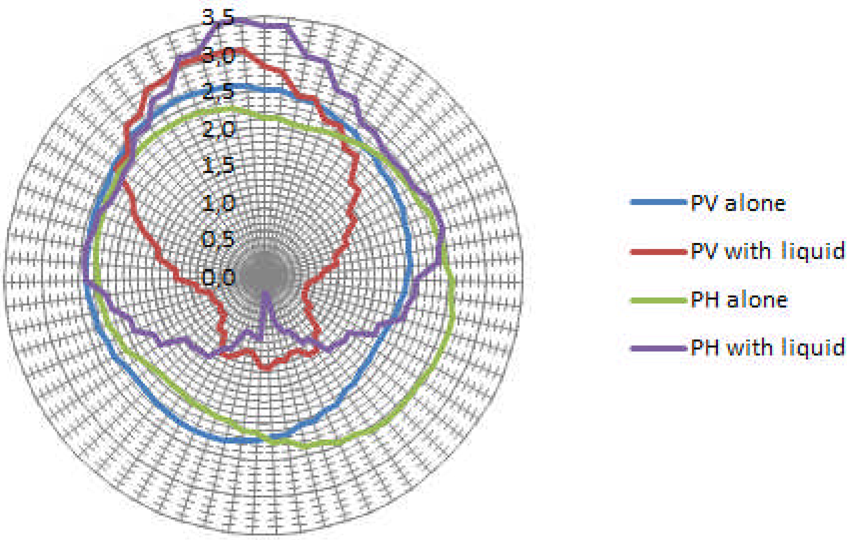

b) DCS results with 20° incidence

Figure 105: Isotropic measurements with and without body liquid for DCS frequency with 0°, +20°, and -16° incidence angles. The legend is the same for all cases.

Comparing the above results, we can see that although with the addition of the body liquid, a strong variation between maximum and minimum value over 360° is observed (due to the shadowing effect of the body), the mean value does not show a similar tendency. For example, the worst case variation between the mean values is seen for the -16° incidence in vertical polarization at GSM frequency of about 8.5 dB between the two cases. For DCS and UMTS this variation is between 0.2 dB and 4.2 dB (for UMTS with PV at -16° incidence). It should also be stated here that these measurements present the worst case scenario, i.e. with a single direction of arrival of the incident E-field. In a real world scenario, the E-field arrives from all angles due to multiple reflections. Hence, the mean masking effect would be different.

Accordingly, the next step is to carry out measurements in the real environment in order to evaluate the impact of the human body.

4.4.2 Dosimeter study in real environment

To evaluate the impact of human body on the dosimeter measurements, the EMESPY140 dosimeter was used to carry out an outdoor study. The objective was to compare four scenarios at three different locations, Table 41.

Table 41: Scenarios for the dosimeter study in real environment.

	Scenarios	Explanation
1	Dosimeter alone fix	Measurement of a dosimeter alone on a tri-pod in static condition during 1 minute.
2	Dosimeter worn fix	Measurement of a dosimeter worn around the waist-line in static condition during 1 minute.
3	Dosimeter alone rotating	Measurement of a dosimeter alone on a tri-pod rotating over 360° with a step of 30°.
4	Dosimeter worn rotating	Measurement of a dosimeter alone worn around the waist-line rotating around 360° with a step of 30°.

Table 42: Locations for the dosimeter study in real environment.

Location	Explanation
Site 1	In a university campus parking alongside a road with buildings in between two BTS stations.
Site 2	In a football field with two BTS stations, on the same side one closer than the other. No environment changes. No buildings in close proximity.
Site 3	Direct Line of Sight (LoS) conditions with the Base Station (BS) on a football field with very little variation of the environment (no passage and few buildings around).

The measurements were carried out for the three DL standards, GSM-DL, DCS-DL and UMTS-DL. The three locations in the city of Brest, France are summarized in Table 41. A detailed analysis of real signals and optimum measurement techniques is given in appendix-7.

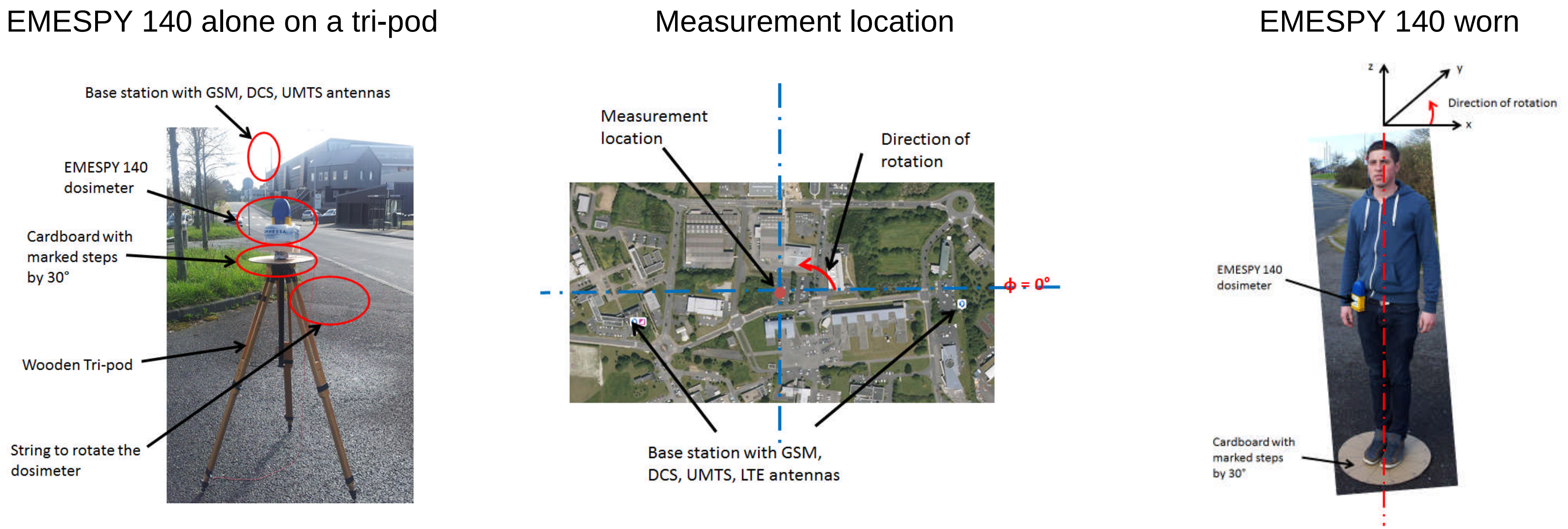
EMESPY 140 alone on a tri-pod
Base station with GSM, DCS, UMTS antennas
EMESPY 140 dosimeter
Cardboard with marked steps by 30°
Wooden Tri-pod
String to rotate the dosimeter
Measurement location
Measurement location
Direction of rotation
ϕ = 0°
Base station with GSM, DCS, UMTS, LTE antennas
EMESPY 140 worn
z
y
x
Direction of rotation
EMESPY 140 dosimeter
Cardboard with marked steps by 30°

(a) Site 1

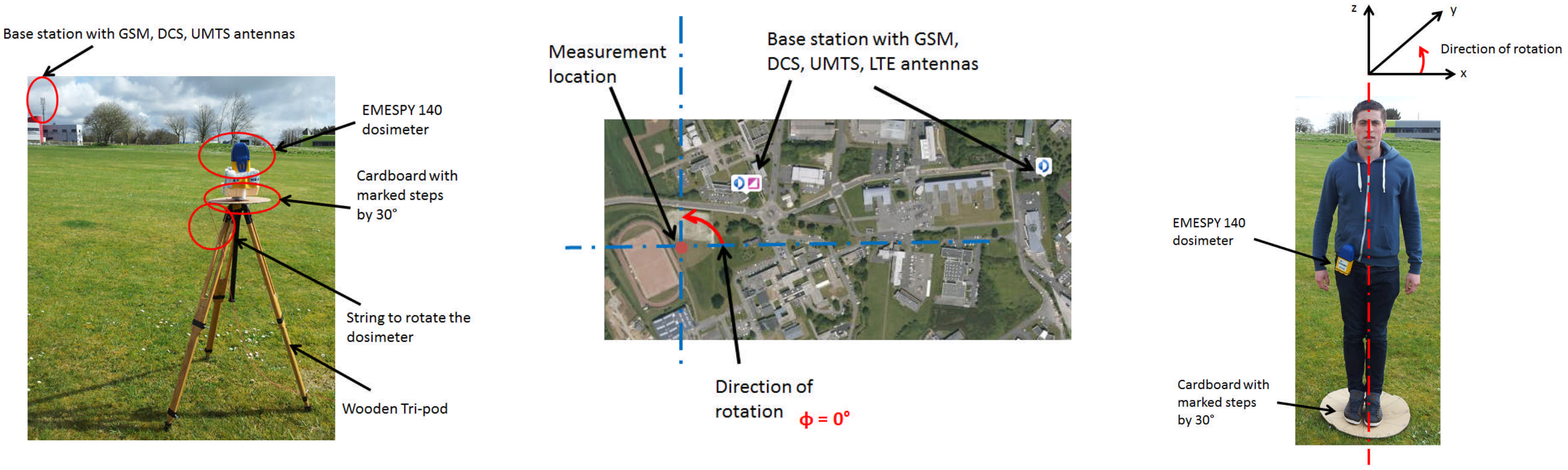
Base station with GSM, DCS, UMTS antennas
EMESPY 140 dosimeter
Cardboard with marked steps by 30°
String to rotate the dosimeter
Wooden Tri-pod
Measurement location
Base station with GSM, DCS, UMTS, LTE antennas
Direction of rotation
ϕ = 0°
z
y
x
Direction of rotation
EMESPY 140 dosimeter
Cardboard with marked steps by 30°

(b) Site 2

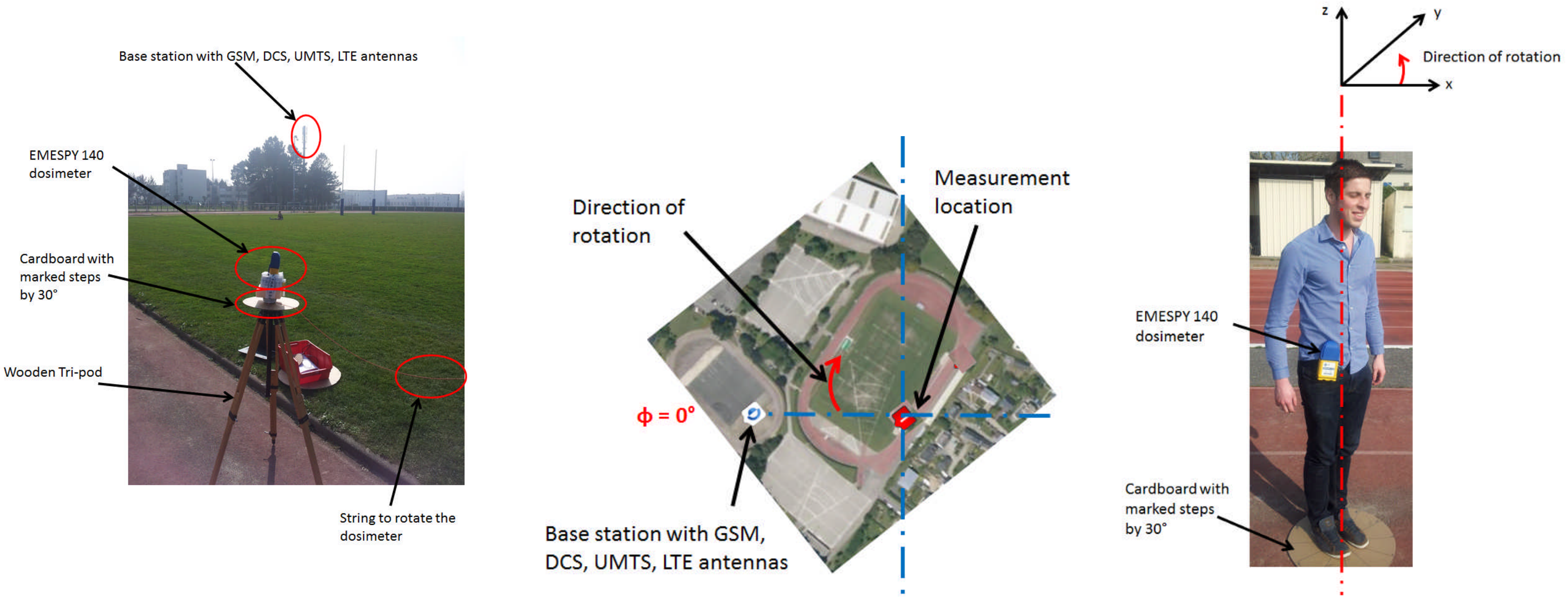

(c) Site 3

Figure 106: Locations for the measurements with EMESPY140 dosimeter.

The results for the three standards are presented in Figure 107 below.

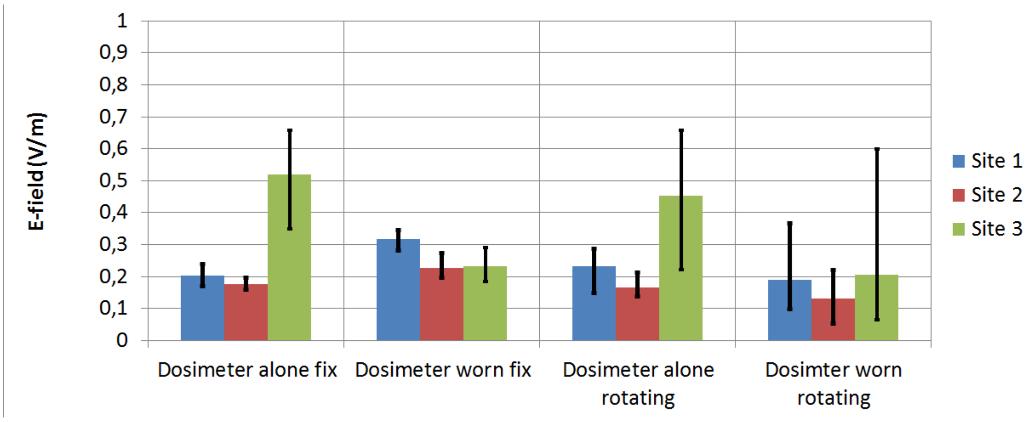

(a) GSM-DL

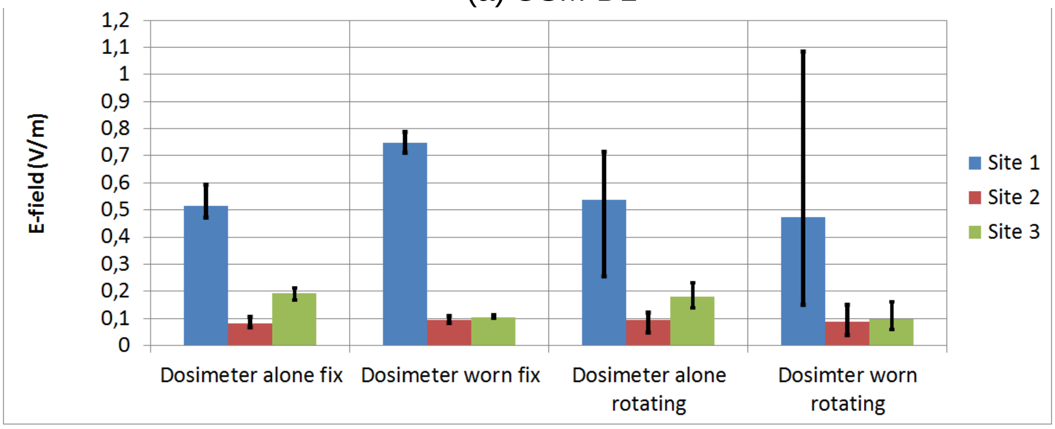

(b) DCS-DL

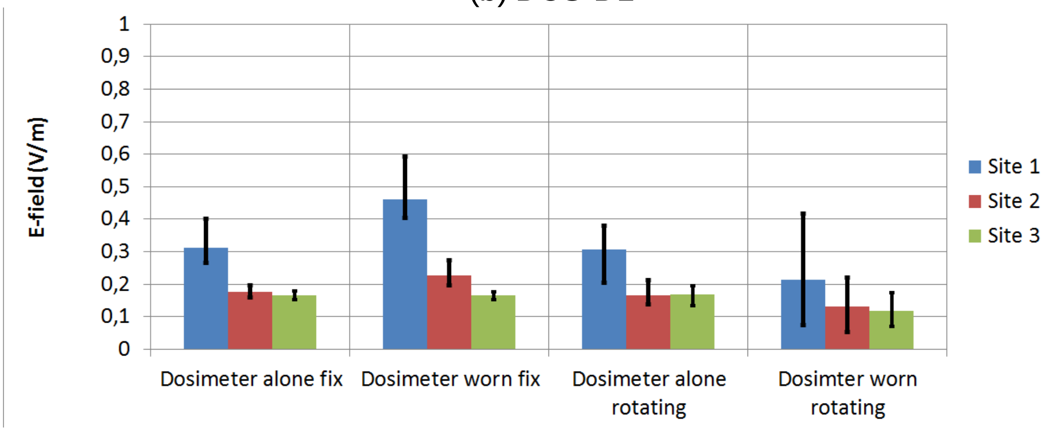

(c) UMTS-DL

Figure 107: Measurement results for the different frequency standards at the three locations (sites) comparing the four scenarios with mean values and variation levels between the maximum and minimum values.

The above results represent a mean value calculated over 12 values (each 30° from 0° to 330°) with the maximum and minimum values for the scenarios with the rotating dosimeter (secnarios#3 and #4 in Table 42). Each of the 12 values is calculated over a single frame of the respective signal (e.g median value over 4.616 ms for the GSM, DCS, and UMTS DL signals). A measurement is carried out each 4 seconds over a 1 minute period. The dosimeter or the person changes their position by 30° each 4 seconds with the help of a cardboard marking the angles as shown in Figure 106.

For the scenarios where the dosimeter is fixed (not rotating), the average value in Figure 107 represents the mean over the 1 minute measurement period with 12 values.

Reference measurements using a three axis probe and a spectrum analyser for each band were also carried out at the three locations and the results are presented in the appendix-6. These measurements show the presence of different operators at the measurement locations and their respective power levels. It can be seen that we are always in the presence of multiple operators with power levels not so far apart from one another. The frequency distribution of different operators in France is also given in the appendix-6.

Considering the above results, it can be observed that in general, when the dosimeter is rotating (alone or in worn conditions), a higher variation is observed as compared to the static measurements. The variations however, are a result of the combination of signal variations over the period of 1 minute, the changing environment, spatial fading changes, and impact of shadowing of the human body, etc. Hence, to extract only the effect of the human body is quite challenging from this data in a real environment as a lot of parameters are varying at the same time. This study however gives us an idea of the error we can have in body-worn conditions in real environment when recording real-time EMF exposure over a given period of time.

A quantitative comparison for the three standards for the three locations is shown in Table 43. The first column is the reference measurement (mean value in V/m) from the one minute static dosimeter scenario. The variation (in dB) is calculated for the other three scenarios by using the previously mentioned reference value.

A maximum variation level of about 8 dB is observed for the GSM-DL case when the dosimeter is the vicinity of a human body as compared to bieng alone on a tri-pod. For DCS and UMTS, the difference is between 0.7 and 6 dB.

Table 43: Mean value variation for the dosimeter measurements at the three locations.

		Dosimeter alone fix (Reference average value) V/m	On body fix / Reference (dB)	Dosimeter alone rotating / reference (dB)	On body rotating / reference (dB)
GSM-DL	Site 1	0,20	3,95	1,19	-0,53
	Site2	0,18	2,18	-0,57	-2,67
	Site 3	0,52	-6,97	-1,17	**-7,98**
DCS-DL	Site 1	0,51	3,25	0,39	-0,69
	Site2	0,08	1,39	1,54	0,80
	Site 3	0,19	-5,41	-0,65	-6,11
UMTS-DL	Site 1	0,31	3,43	-0,15	-3,25
	Site2	0,18	2,18	-0,57	-2,67
	Site 3	0,16	-0,01	0,21	-2,85

4.4.3 Studies with two dosimeters in real environment

To mitigate the body shadowing when the dosimeter is worn, the following section quantifies the advantages to use a second worn dosimeter. A measurement campaign with a human subject and two EME SPY140 dosimeters has been carried out in real indoor and outdoor environments. The version of the used dosimeters provide non polarimetric data, i.e; the E-field magnitude. Indoor measurements were performed at Télécom ParisTech premises in an amphitheatre, a classroom and a corridor. Outdoor ones were driven in Paris around Télécom ParisTech, in streets along three different “routes”. For both, LOS and NLOS conditions were considered. For the first measurements subset, one dosimeter was worn on the subject’s chest and the other above his head such that it could be approximately considered as isolated and used as reference. For the second subset, both dosimeters were worn by the subject, one on the chest and the other on his back (at the trousers right rare pocket level). Measurements were carried out sampling the routes typically every 1.5 m, recording several samples at each position, standing still during about 25 s, which corresponds to about 6 samples per static position, for the measurement minimal repetition period of the dosimeter which is of 4 s. In addition, for each “scenario”, measurements were regularly recorded while the subject was rotating on the spot every 45°, standing still during 40, 50 or 60 s (depending on the cases) for each orientation (corresponding to about 10, 12 or 15 samples per orientation). Each route has been sampled in both directions (“forward” and “backward”) in order to underscore the body masking effect, in particular in LOS conditions.

The first measurements subset is intended to bring out the body masking effect, the “isolated sensor” serving as a reference. A part of the processing of these measurement data will be consequently performed after normalization of the “on-body” measurements by the isolated ones. Besides, the performance of possible correction schemes of the measurement errors due to the “body effects” are tested *relative* to the isolated measurements.

The second measurement subset is notably intended for testing the performance of the error correction strategy based on the usage of two dosimeters (placed at two opposite sides of the body).

Figure 108 : Outdoor measurements forward and backward routes. Involved base stations are identified. The rotation phases are roughly indicated by the red cross symbols.

Figure 109 : Measurement configurations with two dosimeters (used in both outdoor and indoor environments). Left: on the chest and "isolated", right: on the chest and on the back.

Measurements are first pre-processed: first the samples ($|E_{sk}^{(c)}|$) in the configuration (c) are averaged for each static position s (giving $|\bar{E}_s^{(c)}| = \frac{1}{K_s}\sum_{k=1}^{K_s}|E_{sk}^{(c)}|$), then, the spatial sampling along each route (*forward* and *backward, c = "f" or "b"*) and the "rotations phases" (c = "r") are separately extracted. An example of raw and pre-processed outdoor measurements (*rue de la colonie*, Figure 108b) with the dosimeter on the chest is given in Figure 110. The body masking effect can be clearly observed for the GSM 900 and UMTS RATs comparing the field amplitude, respectively, along the forward and backward routes, the LOS BS (Figure 108 left) being in the back of the subject for the first and in front of him for the last. Note that the backward sequence has been reversed in Figure 110 right plot so as to be able to compare both routes at roughly the same static positions. Conversely, for the RATs either in NLOS conditions (GSM 1800) or composed of numerous disseminated sources (WiFi), resulting in an aggregated signal characterized by a wide angular spread, both routes give similar results.

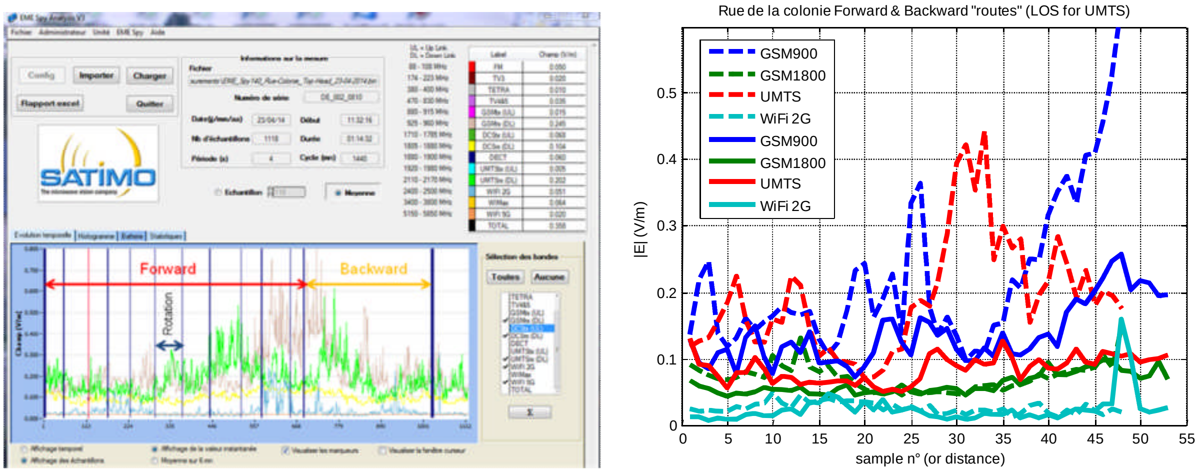

Figure 110 : Example of outdoor measurement (*rue de la colonie*, dosimeter on the chest): raw measurement (left); after pre-processing (right), forward (plain) and backward (dashed) routes.

An example of the statistics of the averaged measured data along the same route (*rue de la colonie*), showing empirical CDFs (and lognormal fits) for both directions (forward and backward) is given in Figure 111. As in Figure 110, it can be observed that in NLOS conditions, both directions give similar statistics, whereas in LOS conditions, the body masking effect is underscored by the CDF shifts.

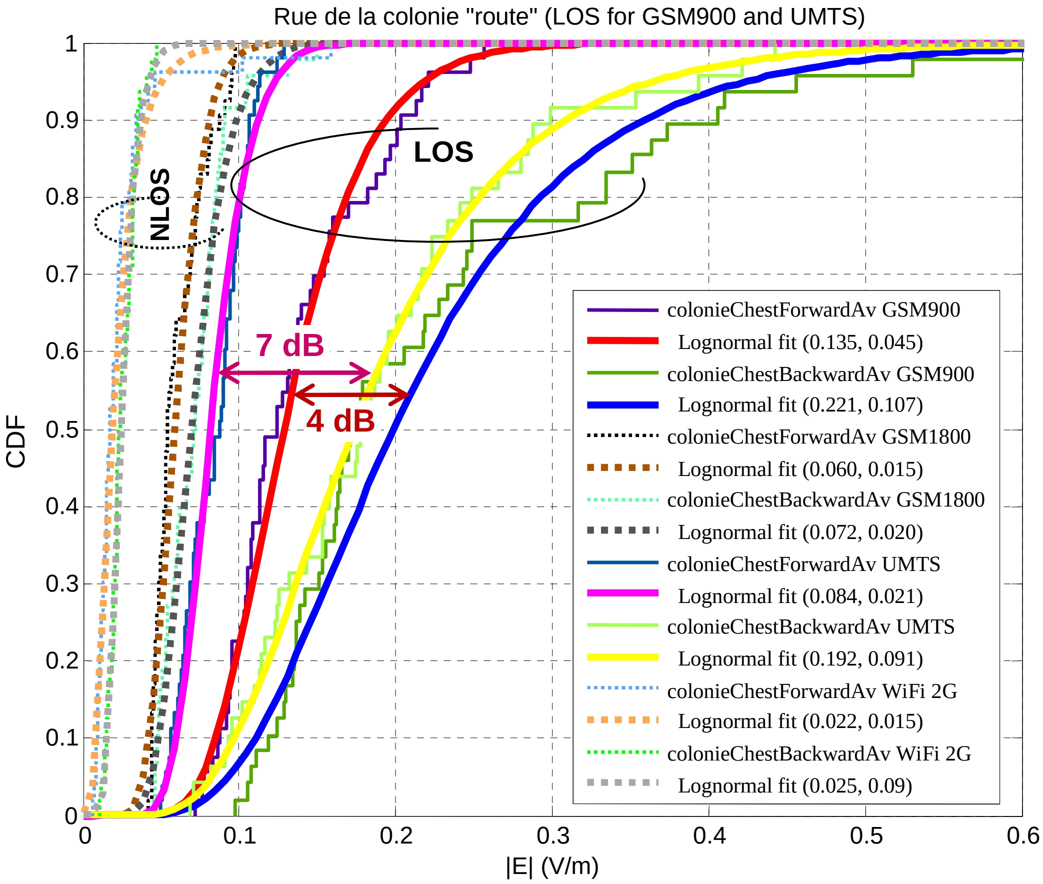

Figure 111 : Example of outdoor measurement (*rue de la colonie*, dosimeter on the chest): empirical CDFs and lognormal fits (with the 1st two moments μ and σ), in LOS (plain) or NLOS (dotted) conditions.

Average trends are summarized in Table 44 for various outdoor and indoor scenarios. The mean values of the field strength are given for each route, respectively for the directions back (*backward*) and forth (*forward*), and for the entire round trip (in the “All” column). In the third column of the “Chest data”, the mean variation is defined in linear scale as the difference between the means in the backward and the forward directions, i.e.:

$$\Delta\mu = \mu_b - \mu_f \quad (3.11.18)$$

and in dB as:

$$\Delta\mu_{dB} = 20\log(\mu_b/\mu_f) \quad (3.11.19)$$

where $\mu_{b,f} = \mathrm{E}[|\bar{E}_s^{(b,f)}|]$

The last column represents the difference between the means of the data measured with the isolated dosimeter and the dosimeter worn on the chest, over the entire round trip. It can be interpreted as a signature of the losses induced by the body proximity.

Table 44 : Average trends of non polarimetric measurements with complete dosimeters.

$\lvert E \rvert$ (V/m)		Chest				Isolated (« Top Head »)			Δμ/μ All
		Forward	Backward	Δμ V/m (dB)	All	Forward	Backward	All	% (dB)
Colonie LOS	GSM900	0.135	0.22	0.087 (**4.3**)	0.18	0.195	0.255	0.22	21 (2.0)
	UMTS	0.08	0.19	0.107 (**7.2**)	0.13	0.175	0.19	0.18	26 (2.6)
Colonie NLOS	GSM1800	0.06	0.07	0.011 (1.5)	0.065	0.105	0.10	0.10	37 (**4.0**)
	WiFi	0.02	0.025	0.002 (0.7)	0.02	0.03	0.03	0.03	24 (2.4)
Vergniaud-Daviel LOS	GSM1800	0.14	0.22	0.08 (**3.9**)	0.175	0.255	0.26	0.26	32 (**3.3**)
	UMTS	0.14	0.22	0.08 (**3.8**)	0.18	0.265	0.27	0.27	33 (**3.5**)
Vergniaud-Daviel Multi BS	GSM900	0.23	0.27	0.045 (1.5)	0.25	0.34	0.335	0.34	25 (2.5)
	WiFi	0.025	0.03	0.002 (0.5)	0.028	0.037	0.028	0.033	15 (1.5)
Amphi LOS	WiFi†	0.12	0.34	0.22 (**8.9**)	0.23	0.25	0.29	0.25	10 (0.9)
Amphi NLOS	GSM900	0.07	0.11	0.04 (3.7)	0.09	0.10	0.10	0.10	8 (0.7)
	GSM1800	0.075	0.09	0.015 (1.5)	0.08	0.08	0.08	0.08	–6 (–0.5)
	UMTS	0.05	0.07	0.02 (2.5)	0.06	0.07	0.07	0.07	10 (1)

†For this case, “forward” (rep; “backward”) corresponds to routes directions along with the direct LOS path from the AP is masked (resp. not masked) by the body. These routes are the same for the other RATs, although it is not really meaningful in NLOS conditions.

The above table shows clearly that the body masking effect is particularly significant in clear LOS conditions. Conversely, in clear NLOS conditions, for which the angular spread is large, the propagation channel reintroduces some “omni-directionality”, so that the loss effect is increased relative to the masking effect. This “loss effect” seems less pronounced in the presented indoor environment, which will need further investigations.

4.5 Strategies for body-worn field sensor correction

CORRECTION SCHEMES FOR MEASUREMENT WITH SEVERAL DOSIMETERS

Recently, it has been proposed in [24] to resort to several dosimeters (in this case at 950 MHz) to compensate for the shadowing and reflection effects, and somehow "regain" omnidirectionality. The results improvement of this interesting approach is really significant. However, although the system uses textile antennas and wearable electronics, one wonder if it can be easily used on a large scale, in particular with regard to its user acceptability, or if it will be restricted to professionals.

CDF of the MRG (averaged over each RAT band) for the considered scenarios are presented in Figure 112 As expected, the high variance observed when using only one sensor (notably in V polarization) can be drastically reduced when using two sensors (in particular on opposite sides of the body). Using all three does not bring any significant improvement (note however that, contrary to the strategy adopted in [24], no attempt was made here to optimize the sensors positioning). Note also that, as it was shown previously, the variance would be further reduced, first using all sensors (non polarimetric measurements), and second considering received signals in real propagation conditions (resorting to analyses involving realistic channel models or "in situ" measurements, as was previously demonstrated). Note eventually that the most stringent aspect is the variance reduction, whereas the observed "biases" can be compensated with an appropriate calibration procedure.

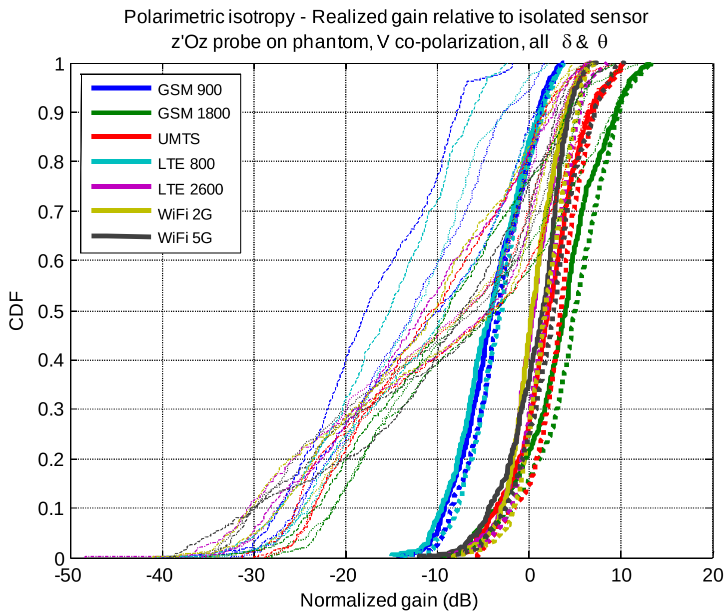

Figure 112 : CDF of the realized gain of the "V" probe of the sensor worn on the chest, hip or back of a whole body phantom (relative to the isolated one), compared to the "combined gain" of 2 sensors, chest/back (plain bold) or hip/back (dot bold).

CORRECTION SCHEMES FOR MEASUREMENT WITH A SINGLE DOSIMETER

Measurements performed with dosimeters (worn-dosimeters) are prone to three possible sources of error:

- Losses induced by the body proximity (in both LOS or NLOS conditions)
- Masking effect of the body in LOS conditions, when the BS (or AP) is opposite to the body side on which the dosimeter is worn
- Reflection effect (from the body) in the reverse situation (dosimeter in direct visibility from the BS or AP.

The following proposed correction scheme is based on “rotation measurements” regularly performed along the measurement route. In LOS conditions, the “masked” measurements along the route are corrected with a coefficient computed as the ratio of measurements registered during rotations in two convenient opposite directions. For NLOS conditions, measurements are simply corrected with a global “loss coefficient”, which can be, a priori, obtained statistically. An example of such scheme is given in **Figure 113** for the “rue de la colonie” route. The RMSE before and after correction is given in Table 44.

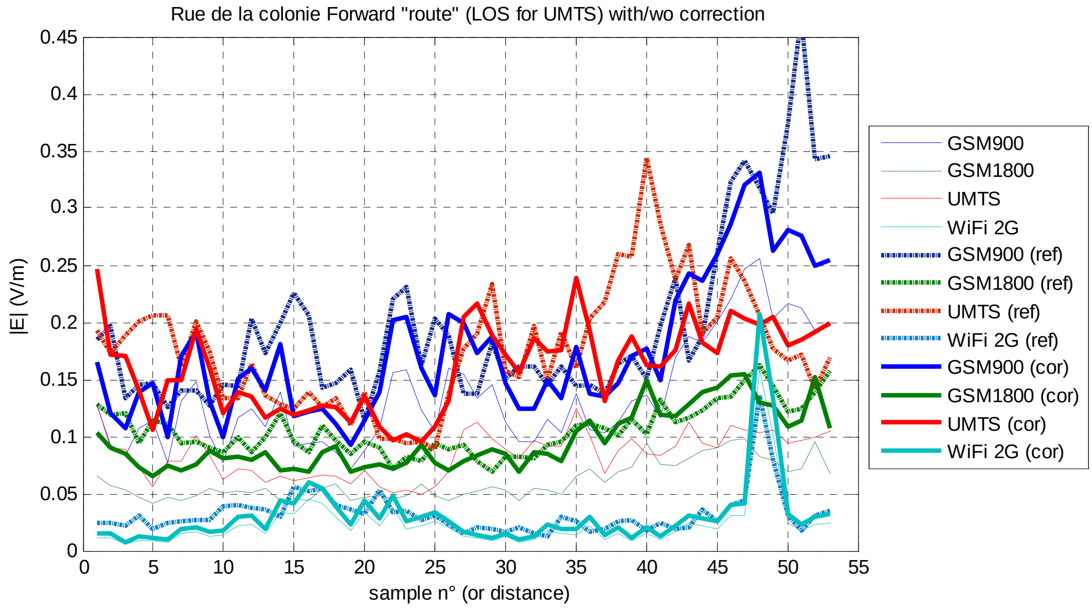

Figure 113 : Field measurements on a human chest, without correction (plain), with correction (plain bold), compared to the reference (dashed dotted). LOS conditions for GSM and UMTS, but the BS is on subject’s back.

Table 45 : Measurement RMSE without and with correction (Rue de la colonie, "forward path").

RMSE		GSM 900	GSM 1800	UMTS	WiFi 2G
Uncorrected	V/m	0.077	0.048	0.103	0.013
	%	39	45	58	45
	dB	**3.2**	**4.9**	**6.5**	**2.8**
Corrected	V/m	0.050	0.021	0.047	0.010
	%	26	20	27	35
	dB	**1.0**	**0.8**	**0.8**	**1.5**

The proposed correction scheme requires the knowledge of the propagation conditions, LOS or NLOS. Techniques based on higher order statistics (notably the Kurtosis) of either the channel impulse response or its delay spread have been proposed in the literature [22] [23]. The implementation of such techniques would be of course at the price of an increased complexity of the receiver, which would require a channel response estimator. Alternative approaches based on the analysis of the statistics of the data measured during the "rotation phases" compared to those measured "along the route" ("linear phases"), avoiding any modification of the receiver architecture, are still under investigation.

Various approaches [25] and [26] have been proposed in the literature, in particular based on daily activity recording. Data fusion, resorting notably to GPS, accelerometers, gyrometers and magnetometers, are more complex alternatives which could be promising.

4.6 Conclusions on wearable dosimeter characterizations

Simulations and measurements with one or several triaxial sensors and anthropomorphic phantoms have been performed in a controlled environment (real or "numerical" anechoic chamber). The influence of the deviation to isotropy and increased cross-polarization level induced by the body proximity, on the field measurement accuracy has been notably analysed. As expected, it appears inter alia from these analyses that the presence of the body induces three effects:

- A global energy loss effect, which can be quantified by the *global efficiency* of the probes (i.e. the total efficiency $\eta_T = (1 - |S_{11}|^2)\eta_e$ in presence of the body), mainly depending on the characteristics of the sensor probes and on the sensor distance to the body. This effect consequently appears as random and should be considered statistically.
- A masking effect of the body in the "shadow region". This effect is generally dominant compared to the first.
- A possible "reflection effect" in the visible region, which can be balanced by the loss effect.

These simulations and measurements have been used jointly with realistic channel models (WINNER2/+) in order to analyse the impact of the propagation conditions, and more generally the channel characteristics – notably its angular spectrum and cross-polarization ratio – on the field assessment and its accuracy, in particular when the sensor is worn by a user. The main conclusions which can be drawn from this study, focussing on the worn sensor, are:

- The interaction between the cross-polarization level of the probes degraded because of the body proximity and the cross-polarization ratio of the incoming waves (due to the depolarization effect of the channel) reduces the reliability of the polarimetric measurements. Measurement errors due to the body presence appear less important when using all probes. In this context, non polarimetric measurements, seem more reliable, and should be consequently preferred.
- The field assessment, and the estimation of measurement errors must take into account the propagation conditions, i.e. realistic characteristics of the channel, because the last re-introduce more or less some “omni-directionality” (depending on the propagation conditions) owing to its angular spread, and because the polarization of the incoming waves are partly random, so that it is difficult to define rigorously intrinsic performance indicators of the worn sensor(s).

“In situ” measurements (in both outdoor and indoor environments) have been performed with complete worn dosimeters. The preliminary results of this campaign confirm the previous analyses, in particular regarding the strong influence of the propagation conditions (LOS or NLOS) on the field assessment and measurement errors. Simple measurement correction schemes, based either on the usage of two dosimeters (combining their measurements) or resorting to only one dosimeter and some specific actions of the user have been proposed.

5 Network environment impact studies

The dosimeter is developed for band-selective measurement of electric field strength in frequency range of LEXNET project. Measurement results from dosimeter are intended to be used for EI calculation. In order to use these results in a proper way, variability of electric field strength should be analyzed. Guidelines which provide general rules for evaluating and expressing overall uncertainty in measurements carried out by LEXNET dosimeter are provided in appendix 3.

Besides the well-known short-term fading, which generally characterizes propagation of radio waves, several additional effects have also significant influence on the EMF strength in the mobile networks environment. The most important effects are [26]: traffic load, automatic transmitter power control and discontinuous transmission.

5.1 Traffic Load impact

The total BS Tx power directly depends on the number and throughputs of the active connections, i.e. its traffic load. In the case of GSM/DCS systems, depending on the traffic load, transmitters are turned on or off. On the other side, in the UMTS and LTE system, the increase in the traffic load forces transmitters to operate at higher power and vice-versa.

5.1.1 Description of the topic

BS traffic load varies during the day and depends on: the applied tariff profiles, the time of the day, the day of the week, the location of BS... As a rule, mobile operator configures the BS in such a way that under certain conditions it satisfies the traffic demands in the so-called busy hour (the sliding 60-minutes period during which the maximum total traffic load occurs in a given 24-hours period). It should be noted that even if the BS is operating with maximum traffic load, the number of active traffic channels is not constant because of the stochastic nature of call arrivals and call durations.

For each individual connection, the BS Tx power is automatically adjusted depending on the propagation conditions in which the mobile terminal resides. Automatic power control is implemented with a frequency of about 2 Hz in GSM/DCS system, with 1500 Hz in UMTS and with 1000 Hz in LTE system.

During an established call, when the user makes a normal pause in speech, the base station temporarily stops transmission (in GSM/DCS system transmitters are turned off, while the traffic channel is not transmitted in the UMTS and LTE systems) [28]. Typically, due to this functionality, for each voice connection, the BS transmitters are inactive approximately 40-50% of time.

All the previously mentioned effects lead to greater instability of the DL EMF strength at the measurement position. For this reason, an additional uncertainty stemming from telecommunications traffic must be taken into account. The value of the uncertainty of this type is determined on the basis of daily traffic profiles obtained by measurements.

The dosimeter is intended to be used for band-selective measurements and it essentially measures a number of electric field components originating from distinct BS simultaneously. Variability of EMF strength originating from different BSs is different from each other, because the BSs are placed at different geographical locations, and carried different traffic loads. This leads to the necessity of analysis of band selective measurements variability with regards to network environment.

For this reason intensive measurements of electromagnetic field strength were carried out in Paris (France) and Belgrade (Serbia).

For sake of brevity, the set-up and detailed results of the two measurement campaigns in Paris and Belgrade are proposed in Appendix 2.

5.1.2 Discussions and conclusions

In this study, the variability of band selective measurements with regards to network environment is considered. Measurement results of the EMF strength for GSM, DCS and UMTS DL bands show that, with regards to field strength variations, day can be separated into two distinctive periods: “active hours” (9h-23h) with higher values and “night hours” (23h-9h) with lower ones. On the other side, as expected, seven day measurements show that two specific categories for 7-day week can be distinguished: working days (Monday to Friday) and weekends (Saturday to Sunday).

In order to use the results obtained with dosimeter band selective measurements for EI assessment, the variability of electric field strength is analysed. For this reason, an additional traffic uncertainty is calculated for 6 different categories regarding the days of the week and specific day periods. Having in mind that for the EI determination, the values of electric field strength (i.e. surface power density) averaged over the defined time periods are needed, the uncertainty caused by telecommunication traffic and transmitter functionalities is calculated for different time intervals of averaging: 10s, 30s, 1min, 6min, 15min, 30min, 1h, 3h, 6h and 10h. In this way, it can be determined how this type of variability of electric field strength affects the uncertainty of EI.

Comparing the uncertainty ranges corresponding to different systems it can be concluded that the highest values are for the UMTS, with range of uncertainties of 4,69 – 14.69 %. Range of uncertainties for the GSM is 4.04 – 12.11 %. The lowest values of uncertainties has DCS, the range is 2.71 – 7.92 %.

Besides the voice communications, UMTS system is often used for data communications, which causes higher variability of electric field strength and consequently higher uncertainty. On the other hand, GSM system provides service to broader user population, mostly for voice communications and lower for data communications. Finally, DCS part of the system has the lowest traffic share and mostly provides voice services for users. On the other hand, data communications are small portion of traffic in DCS.

The results show that uncertainty decreases with increasing of averaging interval. For example, in category “all days – all hours” for UMTS, the uncertainty is decreasing from 14.58% calculated for 10s interval to 7.7% for 10h interval. In category "all days – all hours" for GSM, the uncertainty is decreasing from 11.74% for 10s interval to 6% calculated for 10h interval. For DCS, in category "all days – all hours", the uncertainty is decreasing from 7.73% for 10s interval to 4.8% calculated for 10h interval. For all other categories the similar behavior can be observed.

In addition the uncertainty caused by telecommunications traffic and transmitter functionalities is analyzed for averaging intervals of all hours (24 hours), active hours (14hours) and night hours (10 hours). These results show that measurement uncertainty for values averaged over all hours (all day), active hours and night hours are below 5%.

5.2 Extrapolation from mono-axial to isotropic EMF measurements

The main objective of this study is to find a way to extrapolate Mono-Axial Antenna (MAA) measurement results to isotropic (three-axial) electric field strength. Standards regulating the field of human exposure to EMF require isotropic measurements of EMF strength [30], [31], [32]. Similarly, for assessment of EI defined in LEXNET project isotropic measurements of DL power density are also required. This is very important issue since the simplified version of dosimeter is using MAA. Additionally, there are plans to employ user equipment (i.e. mobile phones) for measuring DL received power for the purpose of calculation of DL power density. It should be noted that most of user devices have a built-in MAA.

When MAA is used, additional extrapolation factor should be applied. Precisely, measurement readings should be multiplied by a scalar extrapolation factor. Consequently, the usage of MAA causes additional uncertainty in measurement readings and should be taken into account also.

The basic idea for determining additional extrapolation factor was to conduct simultaneous measurements of all three spatial components of electric field and try to develop empirically the model for the extrapolation of measurement results obtained with MAA to the isotropic case.

Due to the complex mechanisms of radio wave propagation, the uncertainty arising from the extrapolation from mono-axial to isotropic case is hard to analyze theoretically (or by simulations) and can be more easily determined by measurements in the field.

5.2.1 Measurement system and methodology

For the analysis, the calibrated measurement system composed of broadband field meter NARDA EMR300 and isotropic E-field measuring probe TYPE 18c (100 kHz to 3 GHz) is used. This equipment allows the measurements of overall electric field strength in the specified frequency range. Nominal sensitivity of the measuring system is 0.2V/m, and because of that measurements were carried out in areas where the electric field strength was well above this value.

In order to collect a large number of measurement results, the measurement system was connected to a remote PC by using optical cable. For each sample, measurement system provides values for all three spatial components of electric field strength E_X, E_Y and E_Z. Total electric field strength E_{tot} is calculated using formula:

$$E_{tot} = \sqrt{{E_X}^2 + {E_Y}^2 + {E_Z}^2}$$

Measurements were performed in seven different scenarios. Scenario 1 is representing indoor propagation environment with both LOS and NLOS conditions. Propagation environment with indoor receiving area and outdoor transmitting antennas is represented in scenario 2. Scenario 3 is representing outdoor environment with outdoor receiving area and outdoor transmitting antennas. Most of the measurement points had LOS conditions with at least one of base station antennas. Scenario 4 is the underground railway station with base stations installed indoor in station. In scenario 5, measurements were performed in dense urban area, in pedestrian area outdoor environment. Scenario 6 is representing suburban outdoor propagation environment, while scenario 7 representing rural outdoor area.

These seven scenarios are representing environments where most of population is exposed. On the other hand, these environments are representing seven different environments with regards to propagation and depolarization of radio-frequency electromagnetic waves.

Measurement system was mounted on a tripod, and it was placed on an industrial cart. E-field probe was placed at the angle of 45° with respect to a vertical axis. Industrial cart with measurement system were slowly moving in the chosen area and slowly rotating with respect to a vertical axis. In such a way equality among the axes was ensured. Measurements were done in 2 hours campaigns and 3600 samples were collected for each scenario. Sampling time was 2 sec.

5.2.2 Determination of extrapolation factor

For each sample value, estimates of extrapolation factors n_X, n_Y and n_Z were obtained using the following formulas:

$$n_X = \frac{E_{tot}}{E_X}$$

$$n_Y = \frac{E_{tot}}{E_Y}$$

$$n_Z = \frac{E_{tot}}{E_Z}$$

Based on the estimates n_X, n_Y and n_Z obtained for each scenario mean value, median value, standard deviation and uncertainty were determined. After that, all estimates of extrapolation factors n_X, n_Y and n_Z were grouped in one set n and for n mean value, median value, standard deviation and uncertainty were determined, also.

5.2.3 Uncertainty caused by the usage of mono-axial probe - u(MA)

The uncertainty caused by the usage of MAA was determined by statistical analysis of a series of measuring results [28][29]. In the first step, the mean value n_{meas} and the standard deviation $\sigma(n_{meas})$ were determined using:

$$n_{meas} = \frac{1}{N}\sum_{i=1}^{N} n_{meas\ i}$$

$$\sigma(n_{meas}) = \sqrt{\frac{1}{N-1}\sum_{i=1}^{N}(n_{meas\ i} - n_{meas})^2}$$

where $n_{meas\ i}$ denotes outcome of the *i*-th measurement and *N* is the total number of measurements.

The relative ratio of the standard deviation and the mean value defines the uncertainty caused by the usage of mono-axial probe ***u(MA)***:

$$u(MA) = \frac{\sigma(n_{meas})}{n_{meas}}$$

In the interests of brevity, the details of this extrapolation study measurements results) have been put in the Appendix 5

5.2.4 Discussions and conclusions

Results of this study show that it is possible to extrapolate mono-axial antenna measurement results to isotropic (three-axial) electric field strength. When mono-axial probe is used, additional extrapolation factor should be applied. Consequently, the usage of mono-axial probe causes additional uncertainty in measurement results and should be taken into account. Measurement results show that the extrapolation factors are very similar for all seven scenarios (Appendix 5 Table 7, . Namely, the mean value for overall extrapolation factor n is in range from 1.84 for scenario 6 to 2.10 for scenario 4. In addition, the median has range from value 1.76 for scenario 2 to 1.83 for scenario 4. On the other hand, the uncertainty caused by the usage of mono-axial probe depends on the environment. The highest value of uncertainty is for scenario 4, and it is 44.77%. The lowest value, which is 21.83%, has the scenario 6.

Regarding the mean values obtained for n_Overall (Appendix 5 Table 8), when mono-axial probe is used, additional multiplicative extrapolation factor value of 1.95 should be applied, and consequently additional uncertainty in measurement results of 33.07% should be taken into account.

6 CONCLUSIONS

This deliverable presents the detailed development of the wearable LEXNET dosimeter. First of all in chapter 2, an analysis explains the usages and the objectives of this E field measurement device which will assess the human exposure and particularly the LEXNET exposure global metric. The non-collaborative approach is selected. It means that the dosimeter, as a measurement tool stays independent from any data sharing with the transmitting sources. The innovative features of the LEXNET dosimeter are also given and compared with regard to the existing products.

Based on the LEXNET project specifications, the RF front-end architecture has been studied in chapter 3, by considering the trade-off between sensitivity, frequency selectivity, frequency range, and energy consumption. Two different configurations have been evaluated and the one with tunable pre-filter, variable gain LNA, and DCR receiver has been selected and developed. The two key advantages of the LEXNET wearable dosimeter are the unique frequency selectivity (able to isolate a 3 MHz service provider band from another) and the extreme hardware flexibility as regards current and future standards in the 0.7-6 GHz LEXNET frequency band. Experimental characterization of each of the sub-components has been individually detailed, with their own performance indicators (frequency selectivity, loss, linearity, consumption, and occupied surface). Then each component from the antennas up to the microcontroller will be integrated as a whole device inD6.2; nevertheless dimensions and total current consumption have been estimated from the previous analyses in order to fix the mechanical design and the battery capacity.

Moreover an innovative study aims to analyze the impact of the body proximity on the E field measured level. Both amplitude and polarization impacts are quantified through measurement and simulation campaigns of an isolated and a body-worn dosimeter. The body proximity generates a deviation to isotropy and increased cross-polarization level induced by the body proximity; the influence on the field measurement accuracy has been notably analyzed. As expected, it appears inter alia from these analyses that the presence of the body induces three frequency-dependent effects:

- A global energy loss effect, mainly depending on the sensor probes and on the sensor distance to the body. This effect consequently appears as random and should be considered statistically.
- A masking effect of the body in the “shadow region”. This effect is generally dominant compared to the first.
- A possible “reflection effect” in the visible region, which can be balanced by the loss effect.

Simulations and measurements have been used jointly with realistic channel models (WINNER2/+) in order to analyze the impact of the propagation conditions, and more generally the channel characteristics – notably its angular spectrum and cross-polarization ratio – on the field assessment and its accuracy, in particular when the sensor is worn by a user. The depolarization effect of the channel reduces the reliability of the polarimetric measurements. Measurement errors due to the body presence appear less important when using all axial probes. In this context, non polarimetric measurements, seem more reliable, and should be consequently preferred. The field assessment, and the estimation of measurement errors must take into account the propagation conditions, because the channel re-introduces more or less some “omni-directionality” owing to its angular spread, and because the polarization of the incoming waves are partly random, so that it is difficult to define rigorously intrinsic performance indicators of the worn sensor(s).

“In situ” measurements (in both outdoor and indoor environments) have been performed with worn dosimeters. The results of these campaigns confirm the previous analyses, in particular regarding the strong influence of the propagation conditions (LOS or NLOS) on the field assessment and measurement errors.

These results drive the bias compensation strategies which shall be based on a statistical approach to take into account the wide variability of the configurations. Simple measurement correction schemes based either on the usage of two dosimeters (combining their measurements) or resorting to only one dosimeter and some specific actions of the user have been proposed.

By measuring the E field strength, when mono-axial probe is used instead of the three probes, additional extrapolation factor of 1.95 should be applied. It causes up to 33% additional uncertainty in measurement results and should be taken into account. Moreover it has been determined how the variability of electric field strength due to the Network environment (throughput daily variation) affects the uncertainty of EI. It is shown that the uncertainty is decreasing from 15% when calculated for 10s interval to 8% for 10h interval.

The LEXNET wearable dosimeter is designed to fulfill the requirements of general public EM exposure on a large deployment base. Thus the perspective at a longer term is to re-use the selected RF architecture study to transpose it on an integrated circuit in order to reach better performances and lower cost.

7 REFERENCES

[1]. EME-Guard broadband dosimeter developed by Satimo industries, [online] http://www.satimo.com/content/products/eme-guard

[2]. Narda personal monitor, developed by Narda, [online] http://www.narda-sts.us/products_personal_nardalertxt.php

[3]. EMEPY 140 dosimeter developed by satimo industries, [online] http://www.satimo.com/sites/www.satimo.com/files/EMESPY140_EN.pdf

[4]. ESM-140 mobile phone dosimeter, [online] http://www.maschek.de/pdf/ESM-140-uk.pdf

[5]. SEAWIND FP7 Project – Deliverable D1.1: "Litterature review of exposure assessment and dosimetry of wireless networks", http://seawind-fp7.eu/uploads/Deliverable%20D1.1.pdf

[6]. D. Picard, S. Chauvin, L. Fouquet, "Characterization of four different radio frequency dosimeters", *6th international workshop on biological effects of electromagnetic fields*, Bodrum, Turkey, 2010.

[7]. G. Neubauer, S. Cecil, W. Giczi, B. Petric, P. Preiner, J. Fröhlich, and M. Röösli, "Evaluation of the correlation between RF dosimeter reading and real human exposure", final report on the project C2006-07, 2008 [online] http://www.emf.ethz.ch/archive/var/SB_Neubaue_pre25f.pdf.

[8]. J FB. Bolte, M. Pruppers, J. Kamer, G. Van der Zande, C. Schipper, S. Fleurke, T. Kluwer, H. Kromhout, and I van Kamp, "The Dutch exposimeter study: developing an activity exposure matrix", *ISEE 20th annual conference*, Passadena, California, 12-16 October, 2008.

[9]. P. Juhasz, "Uncertainties in EMF antenna measurements", COST STSM scientific report, 2010, [online] http://www.cost-action-bm0704.org/doc/STSM_Report_Juhaszp.pdf

[10]. http://www.avagotech.com/pages/home

[11]. http://www.hittite.com/

[12]. http://217.34.103.131/homepage/homepage.html

[13]. http://www.rfmd.com/

[14]. Wide band PLL- VCO from Hittite microwave corporation, [online] http://www.hittite.com/content/documents/data_sheet/hmc833lp6g.pdf

[15]. http://www.ciblenergie.fr/fr/index.php

[16]. C. Roblin, S. Bories, and A. Sibille, "Characterization tools of antennas in the Time Domain," IWUWBS, Oulu, June 2003.

[17]. T. Alves, "UWB characterization of the dielectric properties of a phantom", Private communication, Feb. 2013.

[18]. http://www.itis.ethz.ch/itis-for-health/virtual-population/human-models/

[19]. J. Meinilä, T. Jämsä, P. Kyösti, D. Laselva, H. El-Sallabi, J. Salo, C. Schneider, D. Baum, "D5.2, Determination of Propagation Scenarios," IST-2003-507581 WINNER, 16/07/2004.

[20]. Pekka Kyösti, Juha Meinilä, Lassi Hentilä, Xiongwen Zhao, Tommi, Jämsä, Christian Schneider, Milan Narandzić, Marko Milojević, Aihua Hong, Juha Ylitalo, Veli-Matti Holappa, Mikko Alatossava, Robert Bultitude, Yvo deJong, Terhi Rautiainen, "D1.1.1 V1.1, WINNER II interim channel models," IST-4-027756 WINNER II, 30/11/2006.

[21]. Juha Meinilä, Pekka Kyösti, Lassi Hentilä, Tommi Jämsä, Essi Suikkanen, Esa Kunnari, Milan Narandžić, "D5.3: WINNER+ Final Channel Models," WINNER+, CELTIC / CP5-026, 30.6.2010.

[22]. S. Venkatesh and R. Buehrer, "Non-line-of-sight identification in ultrawideband systems based on received signal statistics," IET Microwaves, Antennas & Propagation, vol. 1, no. 6, pp. 1120-1130, December 2007.

[23]. J. Zhang ,J. Salmi, and E.-S. Lohan "Analysis of Kurtosis-based LOS/NLOS Identification using Indoor MIMO Channel Measurements." Vehicular Technology, IEEE Transactions., vol. 62,no. 6, pp. 2871 – 2874, July 2013.

[24]. A. Thielens *et al*, "Design and Calibration of a Personal, Distributed Exposimeter for Radio Frequency Electromagnetic Field Assessment," COST IC1004, TD(13)08033, Ghent, Belgium, 25-27 Sept. 2013.

[25]. J. Blas *et al*, "Potential exposure assessment errors associated with body-worn RF dosimeters," Bio Electro Magnetics, 28(7), 2007.

[26]. S. Iskra *et al*, "Factors influencing uncertainty in measurement of electric fields close to the body in personal RF dosimetry," Radiation Protection Dosimetry, 140(1), 2010.

[27]. Mishra A. R. (Editor). "Advanced cellular network planning and optimization: 2G/2.5G/3G...evolution to 4G", John Wiley & Sons, West Sussex, England, (2007).

[28]. Joint Committee for Guides in Metrology (BIPM, IEC, IFCC, ILAC, ISO, IUPAC, IUPAP and OIML), JCGM 100:2008, "Evaluation of measurement data – Guide to the Expression of Uncertainty in Measurement".

[29]. G.Basso, "Uncertainty in the measurement of electromagnetic field with isotropic broadband sensor and selective E&H field analyzer", NARDA Safety Solutions, 2009.
[30]. European standard EN 50400:2006, "Basic standard to demonstrate the compliance of fixed equipment for radio transmission (110 MHz — 40 GHz) intended for use in wireless telecommunication networks with the basic restrictions or the reference levels related to general public exposure to radio frequency electromagnetic fields, when put into service".
[31]. European standard EN 50383:2010, "Basic standard for the calculation and measurement of electromagnetic field strength and SAR related to human exposure from radio base stations and fixed terminal stations for wireless telecommunication systems (110 MHz — 40 GHz)".
[32]. European standard EN 50492:2008, "Basic standard for the in-situ measurement of electromagnetic field strength related to human exposure in the vicinity of base stations".
[33]. Antenna Standards Committee of the IEEE Antennas and Propagation Society, IEEE Standard Definitions of Terms for Antennas, IEEE Std 145-1993, IEEE Standards Board, New York, NY, USA, Mar. 1993.
[34]. ANFR report on E-field measurement in the city of Brest, online refrence: http://www.cartoradio.fr/cartoradio/web/rapports/Rapport%20public%20OO111305-R.pdf
[35]. ANFR report on E-field measurement in the city of Brest http://www.cartoradio.fr/cartoradio/web/rapports/R_SO034_1_1PUB.pdf

APPENDIX 1: INTERNAL REVIEW

	Reviewer 1: Yoann Corre			Reviewer 2: Xavier Begaud		
	Answer	**Comments**	**Type***	**Answer**	**Comments**	**Type***

1. Is the deliverable in accordance with

(i) the Description of Work?	☒ Yes ☐ No		☐ M ☐ m ☐ a	☒ Yes ☐ No		☐ M ☐ m ☐ a
(ii) the international State of the Art?	☒ Yes ☐ No		☐ M ☒ m ☐ a	☒Yes ☐ No		☐ M ☐ m ☐ a

2. Is the quality of the deliverable in a status

(i) that allows to send it to EC?	☒ Yes ☐ No		☐ M ☐ m ☐ a	☐ Yes ☐ No		☐ M ☐ m ☐ a
(ii) that needs improvement of the writing by the editor of the deliverable?	☒ Yes ☐ No	Only the small proposed correction. However, my own feeling is that the deliverable is too long; too many technical details are reported.	☒ M ☐ m ☐ a	☒ Yes ☐ No	Report is well written and rich. As introduction, it will be interesting to remind the Lexnet index and after (for each part) explaining which term(s) of the index is(are) considered in the chapter. The content is maybe unbalanced. Part 2 is quick because it's seems that there is too few wearable dosimeters. Is-it the reality ? The Sota only deals with only industrial products. No academic team is working on such a device? Part 3 is clearly presented but the justification of some choices are not realy explained.	☐ M ☒ m ☐ a

					Part 4 is difficult to assess because many results are presented. It's probably necessary to change the table of content or the organisation of this part to clearly see the contribution. Summary tables may help to synthetise with also tranfert of some results in the annexes.	
(iii) that needs further work by the partners responsible for the deliverable?	☐ Yes ☒ No		☐ M ☐ m ☐ a	☐ Yes ☐ No		☐ M ☐ m ☐ a

* Type of comments: M = Major comment; m = minor comment; a = advice

APPENDICES FROM 2 TO 7

To keep a decent size to the D3.2 release 2, the other appendices are in a separated file (LEXNET_WP3_D3.2_release2_Appendices.doc)